MACRO-SCALE LEAD HALIDE PEROVSKITE CRYSTALS IN STABLE HIGH-EFFICIENCY PHOTODETECTOR APPLICATIONS

by

Md Mehedi Hasan

A thesis submitted in partial fulfillment of requirements
for the degree of Master of Applied Science

at

Dalhousie University

Halifax, Nova Scotia

December 2018

© Copyright by Md Mehedi Hasan, 2018

To my mother Jamila Khatun and late father Rezaul Haque

Table of Contents

List of Tables

List of Figures

Abstract

Scalable solution-processed methylammonium lead iodide-based perovskite materials are exhibiting high performance by controlling over the morphology, crystallinity, and crystal orientation in perovskite film. High-quality crystallized perovskite films and millimeter size single crystal grains were demonstrated using a meniscus-assisted blade coating technique. The blade-coated perovskite grain is also compared with conventional spin-coated perovskite film both in morphology and for application in optoelectronic devices. The dissertation is concluded by presenting the comparison of blade-coated perovskite photodetectors with the conventional spin-coated perovskite photodetector. The blade-coated perovskite photodetector obtains a responsivity (R) of 148.7 A/W using a 522nm wavelength of light with a calculated external quantum efficiency 3.52×10^4 % under at 4V bias, which is higher than the reference of conventional spin-coated devices. In addition, the larger crystal grain in blade-coated perovskite film enhanced the stability of the photodetector devices, to a value above 80% higher than a reference spin-coated device.

List of Abbreviations Used

OM	Optical Microscopy
XRD	X-Ray Diffraction
UV-Vis	Ultraviolet Visible
PL	Photoluminescence
TRPL	Time-Resolved Photoluminescence
Au	Gold
NIR	Near Infrared
Pb	Lead
Sn	Tin
DMSO	Dimethyl Sulfoxide
GBL	Gamma Butyrolactone
EQE	External Quantum Efficiency
ITO	Indium Tin Oxide
UVO	Ultra-Violate Ozone
TCSPC	Time-Correlated Single Photon Counting
SPAD	Single Photon Avalanche Photodiode
FTO	Fluorine Doped Tin Oxide
IPA	Isopropanol
R	Responsivity
mm	Millimeter
um	Micrometer
nm	Nanometer

Acknowledgments

I would like to thank my supervisor Professor Ghada Koleilat for giving me this wonderful opportunity to conduct my graduate studies with her research team. I'm also grateful for her thorough guidance and feedback, inspiration and patience, and financial support all through the dissertation work. I would also like to acknowledge the financial support from Dalhousie's Faculty of Graduate Studies during my graduate studies.

I would like to thank Professor Ian Hill and Professor Kimberley Hall in the Physics department for their strong support in my project work. I am deeply grateful to Charlotte Clegg for her constant help with research work and her patience dealing with my requests for materials. She has been a great friend throughout the project works. Similarly, thanks to Dean Grijm for his great instrumental support in our lab and grateful to Max Manning and Daphne Palaco for their instrumental setup and characterization during my project work in Koleilat Group.

I am grateful to all of the previous and present lab members of Koleilat Group, and have collaborated with in discussions with Shayan Angizi, Ahmed El Ghanam, Chen Su, and Tarmy Abbot.

Lastly, I dedicate my dissertation to my mother and late father Rezaul Haque. I'm in debt to my father who has been a source of encouragement and motivation. He would have been extremely excited that I finally completed my degree.

Chapter 1 Introduction

Applications of silicon-based photon-sensitive semiconductor devices are severely limited by the high radiation of traditional silicon, which exceeds 40%. In addition, the large bandgap, especially for wavelengths greater than 1.1 μm, delimits the useful wavelength spectrum of bulk silicon. Moreover, the high reflectance of silicon-based devices across the electromagnetic spectrum severely influence their efficiency and sensitivity [1]. Thin film photodetectors have important applications in areas such as environmental monitoring, large-area displays, and optical communications, and they are of great importance in both civil and military fields [2] .

1.1 Background and Motivation

In the commercial market, indium gallium arsenide (InGaAs) and germanium-based semiconductors are used for near-infrared detection in parallel with silicon materials. However, these photodetectors exhibit some disadvantages for commercial use. The inorganic materials are expensive, with high noise characteristics as well and poor integration with the present silicon-based electronic processes. In the past few decades, scientists have focused on finding effective methods to upgrade the responsivity of conventional silicon materials [3]–[6]. Recently, In_2Te_3, ZnO, GaN, and flexible nanostructures of nanowires and nanoparticles have been used in photodetectors for the ultraviolet-visible (UV-Vis), and near-infrared (NIR) spectrum [3]–[6].

Currently, many researchers are working on solution-based perovskite films. Methods of using the perovskite film as a photodetector have exhibited excellent performance. Recent studies have concentrated primarily on various methods of enhancing the stability of the perovskite active layer, and on replacing the lead (Pb) with tin (Sn), resulting in improved performance [7]. Over the past few years, organic-inorganic hybrid perovskites have attracted considerable attention due to ground-breaking success in the field of photovoltaics. A deeper understanding of the optoelectronic and structural properties of perovskite materials has facilitated their use in light emitting diodes, lasers, photodetectors, photodetectors, memory devices, *etc.* Due to the structural simplicity of perovskite materials, low-cost fabrication, and operation at room temperature, the solution process is suitable for real applications.

In comparison with other non-organic photodetectors, solution-processable lateral structure organic-inorganic hybrid photodetectors display attractive characteristics, including light weight, transparency, flexibility and ease of fabrication [8]–[10]. At the same time, photodetection performance can be improved with other device configurations, such as photodiodes, photodetectors, and phototransistors. Generally, a perfectly placed semiconductor lattice structure plays a role in forming the optoelectronic system. A precisely oriented crystal structure is an essential element in high-quality photodetectors, allowing the photoactive materials to be placed between the electrodes in photodetectors, and enabling them to serve as the channel material in photodetectors, photodiodes, and phototransistors [11].

The main applications of metal halide perovskites are concerned with optoelectronic devices, where obtaining a high-quality thin film morphology is crucial. Thus, the engineering of perovskite thin films is a key consideration and the production of crystallized perovskite thin films has been extensively studied. For perovskite nanostructures can be prepared in thin films via solution processes including centrifugal casting, drop casting, spin coating, spray coating, and blade coating as illustrated in Figure 1-1 [12]–[14]. These methods are not difficult to execute and are compatible with a wide range of perovskite solutions. According to the number of fabrication steps, solution processing can be divided into two steps: single-step and sequential deposition by two steps. Both processes can deposit films with various stoichiometric ratios. In a single-step

process, a precursor solution of perovskite with certain components is dissolved in a selected solvent, and the thin film is prepared via solution processing.

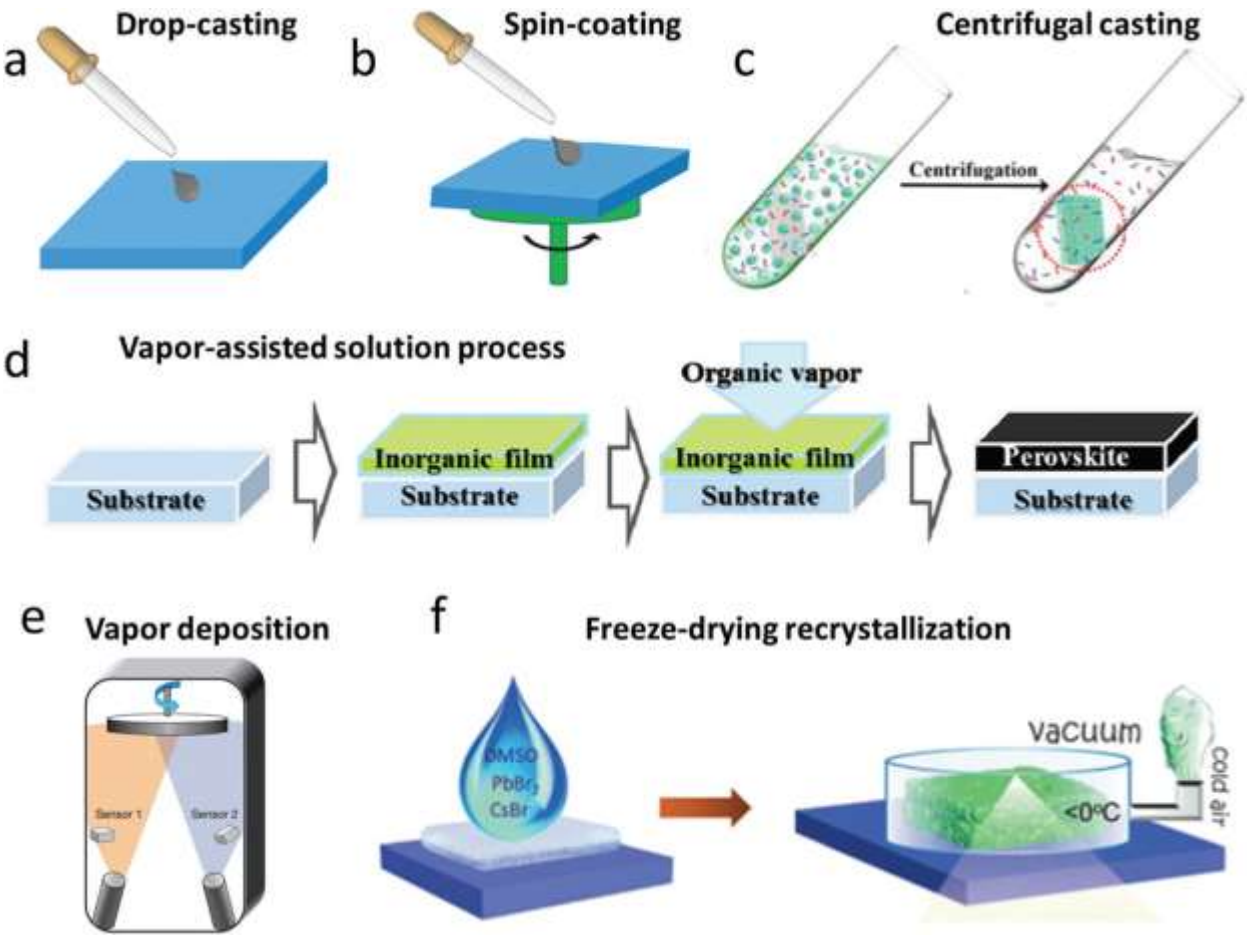

Figure 1-1 Perovskite thin film fabrication method by (a) Drop-casting, (b) Spin-coating, (c) Centrifugal casting from ref. [15], (d) Vapor-assisted solution process from ref.[16], (e) Vapor deposition from ref. [17] and (f) Freeze-drying recrystallization from ref. [18].

Due to recent scientific advances, $CH_3NH_3PbI_3$ perovskite semiconductor materials are a focus of attention for optoelectronic devices and are showing great prospective in the field of optoelectronic devices. This is due to their outstanding optoelectronic properties, such as nearly 100% photoluminescence quantum yields, carrier diffusion lengths more than 175 mm, and tunable light absorption wavelengths.

The present work explores and optimizes the perovskite solution fabrication technique referred to as blade coating of perovskite materials. The optimized perovskite film is then applied to a photodetector application.

1.2 Current Challenges

The development of perovskite-based optoelectronic devices faces two major challenges. One is the intrinsic instability of perovskites and the other is the toxicity of lead-based perovskite materials. The instability originates from the organic cations of perovskites. This limitation hinders their practical application in photovoltaics and in optoelectronic devices such as photoconductors, photodetectors, light emitting diode, and lasers.

This instability can be addressed partially by encapsulation techniques which commonly employed in the electronics industry and by coupling with other materials. Another method replaces the organic cations with inorganic cations such as cesium [13]. In dealing with this issue, strategies involving replacement with inorganic ions seem to be more prominent. According to reports in the literature, the performance of inorganic perovskite-based

optoelectronics is nearly comparable to that of optoelectronics with hybrid perovskites materials [13].

Another issue is the recombination losses in perovskite-based optoelectronic devices. Different fabrication techniques and interfacial engineering can play an essential role in reducing recombination in perovskite thin films [19]. One of the unsolved problems is film thickness. This is being investigated by many researchers in order to achieve an optimal thickness of perovskite materials in a device. Moreover, there is a solution to reduce recombination in a device, to make a correct choice of electrode for efficient electron and hole transfer. Due to these issues, the performance of the resulting devices and their photophysical mechanisms are far from satisfactory.

1.3 Research Questions and Contributions

A solution-based perovskite film was generated by using a different concept to fabricate the crystallized film and work is still being done to achieve better performance from the applications [17-20]. The performance of the device output and stability is based on the thin film morphology and crystallized structure [29]. This thesis explores and optimizes the perovskite thin film fabrication technique and studies the influence of different precursor solvents evaporation rate on the micro-structures of $CH_3NH_3PbI_3$-based perovskite film, which have not previously been examined.

The first challenge was the optimization of the blade coating technique to obtain the crystallized perovskite thin film. Another challenge was to control the perovskite crystal

grain size and to improve the crystallized thin film stability. The blade coating technique was optimized by changing the shearing blade angle and the direction of motion of the metal plate. After the technique was optimized, the meniscus-related blade coating method required making a larger size of crystal grain. An optimal crystal grain size was achieved by using a suitable solvent evaporation rate (with a fixed metal plate temperature), blade coating speed, and gap between the substrate and blade. The next question was how to obtain a stable perovskite thin film. This was achieved by using an optimal concentration of $CH_3NH_3PbI_3$ perovskite solution and an appropriate thermal annealing method on the fabricated perovskite layer.

Furthermore, this work addressed the question concerning the effect of mixing the precursor solvent on the precursor perovskite solution and the crystal structure, with the use of the blade coating technique. This issue is connected with the mixing ratio of the solvents and precursor perovskite solutions concentration. The focus of this thesis was to observe the influence of dimethyl sulfoxide (DMSO) solvents on $CH_3NH_3PbI_3$ based crystallized thin film morphology.

Finally, the electrical performance of a lateral structure perovskite photodetectors was investigated with the use of the blade coating technique. A maximum performance in terms of photo response (I-V), responsivity speeds (R) and external quantum efficiency (EQE) was achieved by applying optimal solutions for blade coating conditions on the pre-patterned interdigitate ITO substrate.

In summary, this work centers around understanding the blade coating of $CH_3NH_3PbI_3$ perovskite precursor solutions, how they work, and the influence of solutions shearing conditions on the film morphology and photodetector performance.

1.4 Thesis Outline

The thesis chapters are organized as follows.

Chapter 2 presents a general overview of different forms of perovskite crystal, such as $CH_3NH_3PbI_3$, $CH_3NH_3PbBr_3$, and $CH_3NH_3PbCl_3$. The chapter begins by comparing the crystal structure of lead-halide based perovskite materials. It also describes the advantages and disadvantages of lead-halide based crystallized perovskite thin films in devices. The chapter concludes by explaining the working principle of lateral structure for perovskite films.

Chapter 3 describes a characterization technique for $CH_3NH_3PbI_3$ based perovskite thin film morphology such as optical microscopy, X-ray diffraction and profilometry for film thickness measurement. The blade coating method is discussed, and crystallized perovskite thin film is compared to spin-coated film. Finally, the chapter discusses in detail the morphology controlling technique and a relationship in between substrate temperature and blade coating speeds.

Chapter 4 discusses first, the photon absorption, photoluminescence and time resolved photoluminescence decay (TRPL) techniques for perovskite film is discussed here. Secondly, the photodetector device layout, how to fabricate the photodetector device, and

the photodetector device architecture is discussed. After that, the performance metrics of the photodetector are introduced in details. The chapter then describes the electrical setup and measurement process for photodetector devices. Finally, the method of measuring photo resistance is described.

Chapter 5 discusses the photodetector results achieved by using the blade coating method. Also discussed a comparison of photon absorption, photoluminescence and time-resolved photoluminescence decay in between spin coated and blade coated perovskite film. A comparative analysis of the photodetector performance is provided for the blade coating and spin coating techniques. The chapter also describes the photo response and stability of the device responsivity (R). Finally, the photo resistance of blade coating and the spin-coated lateral structure photodetector are discussed and compared.

Chapter 6 concludes the thesis with a description of the research contributions and a short discussion of future aspects of work on the perovskite-based optoelectronic devices.

Chapter 2 Theoretical Background

A star semiconducting material $MAPbX_3$ (MA = CH_3NH_3I and X = I, Cl, Br) is called organic-inorganic halide perovskite. This chemical has different forms, such as $MAPbI_3$, $MAPbBr_3$, and $MAPbCl_3$. The perovskite materials have applications in optoelectronics such as organic light emitting diodes (OLED), photodetectors, lasers, thin film transistors, perovskite solar cells, and perovskite photodetectors. Until today, the best perovskite solar cells can already transform over 22% of the energy of sunlight into electricity by using polycrystalline halide perovskite [20]. The recent improvements in performance of perovskite-based solar cells is leading to the development of high performance light detecting optoelectronic devices. Active research is still in progress specifically in the area of halide base perovskite optoelectronic devices. Due to easy fabrication and a lower cost of materials, applying this material can be effiiciently done to devices such as the photodetector, photodetector, and OLED [21]–[23].

Recent reports show that the high responsivity (R) in halide base lateral-structured photodetector devices is achieved from a $MAPbI_3$ based lateral-structured perovskite photodetector [24]. This $MAPbI_3$ perovskite material is used as an active layer in device for photon detecting and providing an electrical signal to the output. The material can transform the energy of sunlight very efficiently because they can strongly absorb both visible and near-infrared light, unlike silicon solar cells (which are produced in high temperature conditions). Low-cost and solution-processable materials of $CH_3NH_3PbI_3$ perovskite have shown promise as active layers in large-area photodetector applications

[3], [25], [26][27]. The need for low-cost photodetectors with broadband of light detection range, high responsivity, high speed of time response, high quantum efficiency, and high gain is apparent; the low-temperature operation of hybrid $MAPbI_3$ perovskite nanomaterials satisfy these criteria.

2.1 Lead Halide Perovskite Structures

Typical three-dimensional (3D) perovskite make up a large family of compounds. The chemical formula is ABX_3, where A (CH_3NH_3) and B (Pb, Sn) are cations of dissimilar sizes and X (Br, Cl, I) is an anion. The inorganic halides (I, Br, Cl) are employed as anions (X), and the different spectral photo-response can be achieved through varying halide components.

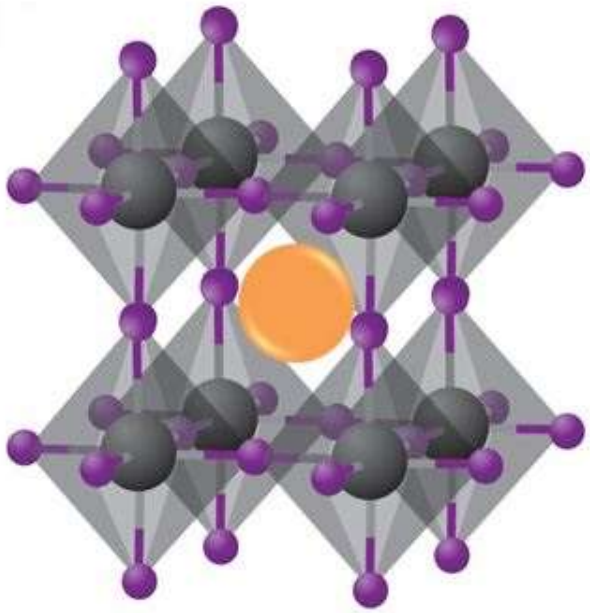

Figure 2-1 Crystal structure of $CH_3NH_3PbI_3$. The metal cation (Pb, grey sphere) is located at the body center of the cubic composed of six halide I-anions (purple). The orange sphere represents the $CH_3NH_3^+$ organic ion [29].

The cation $CH_3NH_3^+$ size is the key component for the formation of a close-packed $CH_3NH_3PbI_3$ perovskite structure. It is required to fit $CH_3NH_3^+$ ion into the space between the four adjacent octahedra and this are connected through corner-sharing as seen in Figure 2-1 [29]. $CH_3NH_3PbI_3$ perovskite materials have different phases depending on the molecule's temperature. With changing the temperature, the crystal structure of $CH_3NH_3PbI_3$ could change from a high-symmetry cubic phase to a tetragonal phase or to a low-symmetry orthorhombic phase [30], [31].

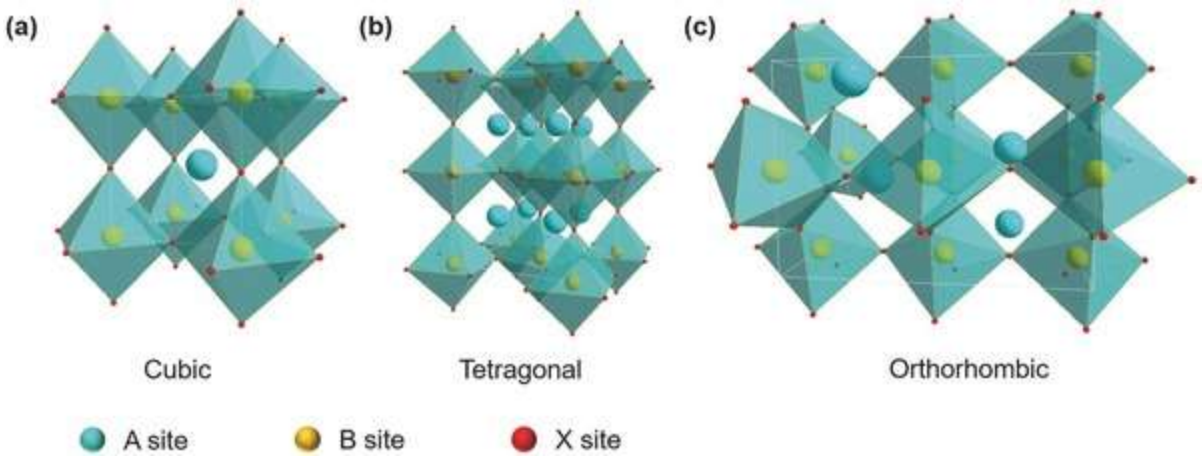

Figure 2-2 The crystal structures of perovskite materials with different symmetries: a) cubic phase, b) tetragonal phase, and c) orthorhombic phase. [31]

As seen in Figure 2-2 (c), the material is shown as a stable orthorhombic (γ) phase when the temperature is lower than 100 K. The tetragonal (β) phase in Figure 2-(b), started to appear replacing the orthorhombic (γ) phase with the increase of temperature to 160 K [31]. After that, the tetragonal (β) phase started to change to a stable cubic (α) phase Figure 2-2 (a), as the temperature further increases to about 330 K [33]. The phase transition of tetragonal-cubic shape at higher temperature partially influences the thermal stability of perovskite materials. There are several intrinsic optoelectronic properties of the $CH_3NH_3PbI_3$ perovskite thin film including ambipolar charge transport characteristics [34], high mobility [35], high dielectric constant [36], low binding energy [37], and ferroelectric polarization [38]. For these reasons, the semiconducting perovskite materials is an excellent candidate for the development of future optoelectronic devices. Thus, the typical $CH_3NH_3PbI_3$ [39]–[45], $CH_3NH_3PbBr_3$ [37], and $CH_3NH_3PbCl_3$ molecules have been extensively studied in the field of photodetectors [46], [47].

2.2 Lead Halide Crystallized Perovskite Thin Film and Single Crystals

To compare with other organic materials, the organolead halide perovskites have a high photon absorption. As a light absorbing molecule, it has stronger absorbance over the spectrum of light from UV-Vis to near infrared. The ambipolar transport propeties of perovskite enables complete light absorption in films as thin as the range of 500–600 nm to overcome the thickness limitations (of ~2 μm) of the classic solid-state dye sensitized solar cells (DSSCs). Another unique behavior of halide-based perovskite is that they exhibit p-type behavior beside the n-type active layer of optoelectronic devices. The reported demonstration of a simple nanoporous $TiO_2/CH_3NH_3PbI_3$ solar cell presents better efficiency without a p-type selective layer [48]. However, the solar cells configuration of mesoporous $ZrO_2/CH_3NH_3PbI_3$/spiro-MeOTAD, shows n-type behavior which achieves 10.8% power conversion efficiency [49]. As observed so far, the organolead halide perovskites $CH_3NH_3PbI_3$, $CH_3NH_3PbBr_3$, and $CH_3NH_3PbCl_3$ are able to exhibit ambipolar charge transport, that means they have potential to be excellent materials for use in optoelectronic devices to achieve high performance.

The study of transport properties of $CH_3NH_3PbI_3$ by performing time-resolved photoluminescence (TRPL) and transient absorption spectroscopy, which reported the diffusion lengths of the electrons and holes to be ~130 nm and ~100 nm [33]. This long charge diffusion length is facilitated by good charge transport in perovskites. The $CH_3NH_3PbI_3$ perovskite-based optoelectronic devices have ultrafast charge generation, high charge carrier mobilities, and low recombination rates. It is therefore relatively easy to achieve excellent device performance from $CH_3NH_3PbI_3$ crystallized perovskite films

[21]–[24]. It is worth mentioning that the perovskite materials have a high crystallinity and are defect tolerant. These characteristics make the study of perovskite photodetectors, photoconductors, or solar cells simpler than other form of perovskite materials.

There are two primary forms of hybrid halide-based perovskites film: polycrystalline films and single crystals. Perovskite thin films have been under intensive investigation and until now most reported applications have focused on polycrystalline thin films. Thus far, the fabrication methods for the perovskite films included one [50] or two-step methods [51], vacuum deposition [52], and vapor-assisted processes [53]. During the crystallization process, the formation of the intermediate phases has shown to be a critical step towards morphological engineering [50]. During the transition from the precursors perovskite solutions to the crystalline perovskite film the intermediate phases form and can facilitate the film reconstruction which that significantly influence the crystallization kinetics [50].

The study of $MAPbI_3$ based perovskite optoelectronic devices reveal excellent optoelectrical properties for applications. A polycrystalline perovskite film and perovskite nanowires have shown comparable performance based on photoresponse. The compact perovskite crystal structure and well oriented crystallized morphology, as presented in Figure 2-3, is the key to demonstrate a better optoelectronic device. The structure and morphology have a significant effect on device performance. Figure shows that a single step and two-step solution process were employed to yield polycrystalline perovskite film [54][55]. As seen in Figure (a),(b), and (c), the polycrystalline $MAPbI_3$ perovskite morphology has shown excellent performance in perovskite photodetector over nanowire perovskite photodetector [10], [54], [55]. The responsivity of the polycrystalline

perovskite-base photodetector was 3.49 AW^{-1} [55] where a nanowires perovskite based photodetector resulted in a 1.3 AW^{-1} responsivity [56]. Comparatively, the prepared nanowires crystal based perovskite photodetector had a value of 13.6 AW^{-1} photoresponsivity, which is comparable to polycrystalline perovskite photodetector [57]. From the comparison of the polycrystalline and the nanowires perovskite film of the vertical photodetector devices, the effect of increasing responsivity was observed only based on perovskite crystal structure.

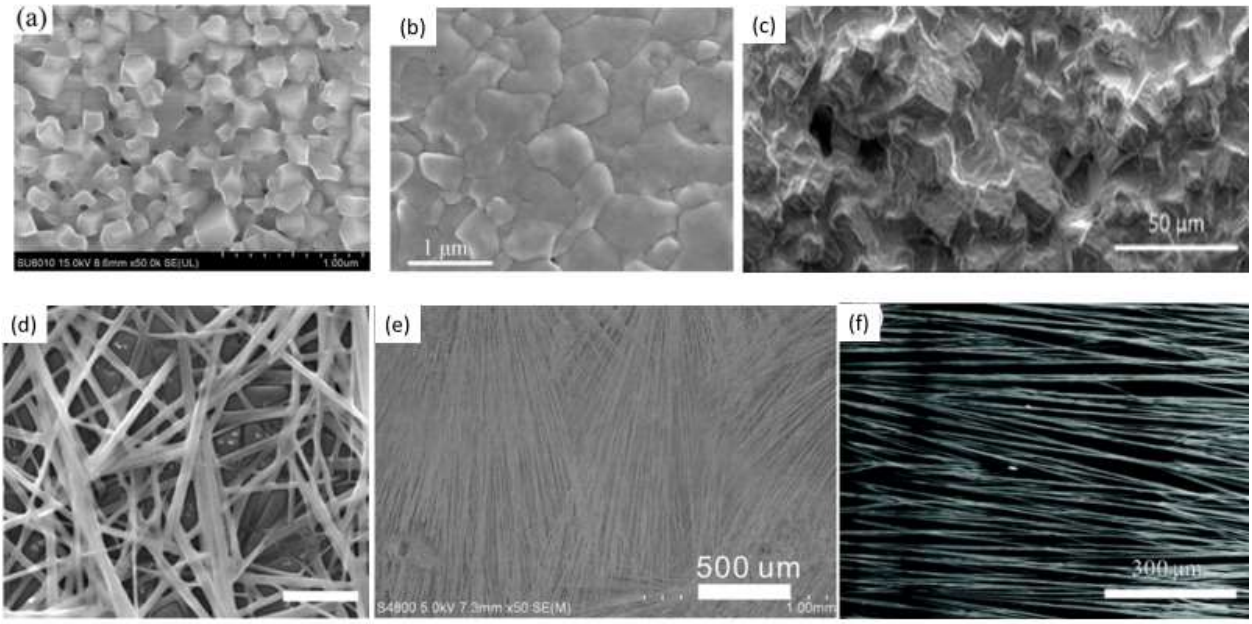

Figure 2-3 Optical and SEM images of $MAPbI_3$ perovskite crystal structure (a) polycrystalline film [54] (b) polycrystalline film [55] (c) microcrystalline film [10] (d) crystallized perovskite nanowires [58] (e) nanowires film [56] (f) perovskite nanowires film via doctor blading [57]

The study of $MAPbI_3$ based single crystals is still in an early stage of research. These crystals are being investigated fundamentally due to their low trap density and absence of crystal grain boundaries. These intrinsic properties of single crystalline $MAPbI_3$ perovskite possess much better optoelectrical properties than polycrystalline perovskite as reported in published journal [8]. In the other published research reports, it has been found that the low trap-state density is on the order of 10^9 to 10^{10} cm^{-3} and long charge carrier diffusion lengths exceed 10 μm in $MAPbI_3$ perovskite single crystals [59]. The $CH_3NH_3PbI_3$ single crystal-based perovskite photodetector devices showed excellent performance with excellent stability in air and a broader response to the electromagnetic spectrum as presented in Figure 2-4 and Figure 2-5. The performance of $MAPbI_3$ single crystalline nanowire-based devices have been found to be more stable than polycrystallinebased perovskite devices due to the photocurrent response as depicted in Figure 2-4. Moreover, as reported, the single crystalline $CH_3NH_3PbI_3$ perovskite photodetector showed roughly 1000 times faster of a photo-current response speed compared to the polycrystalline counterparts as seen in Figure 2-5 [9].

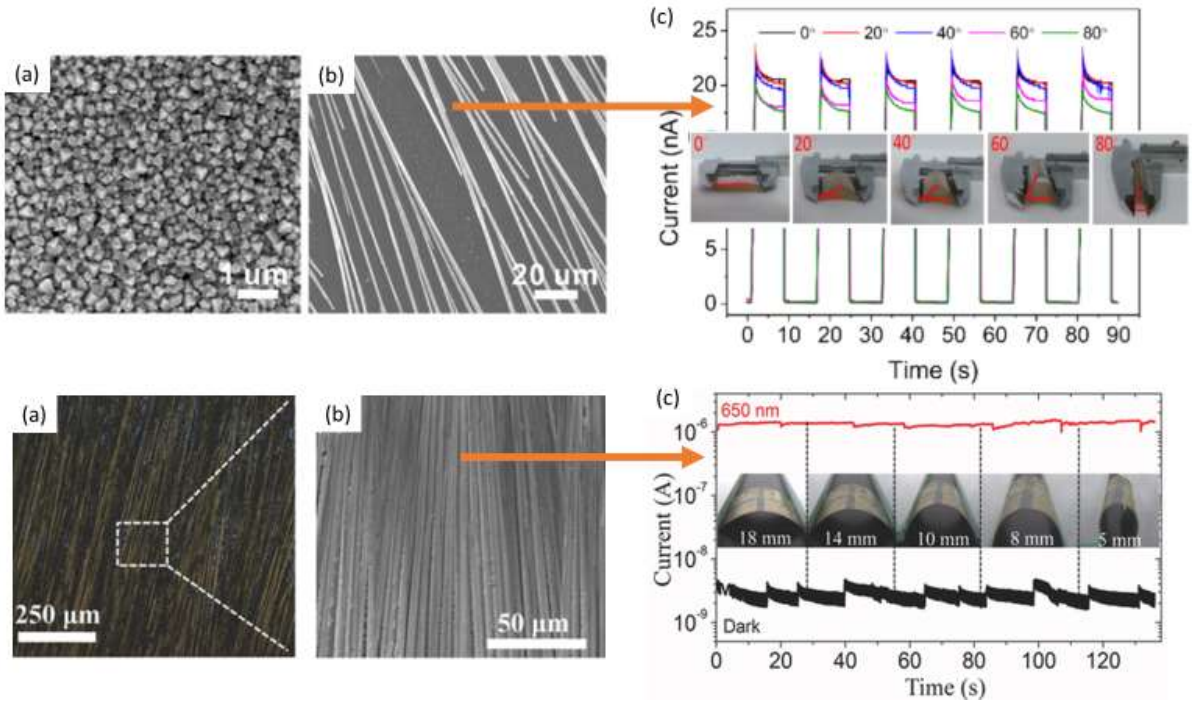

Figure 2-4 Stability performance of polycrystalline and single crystalline perovskite film, top row (a) nanocrystalline film (polycrystalline film) (b) nanowires perovskite film, (c) photo-current stability of polycrystalline film, and the images in below row (a) single crystalline nanowires (b) squire area of (a) at high resolution (c) photo-current stability of polycrystalline single-crystalline perovskite film [8], [60]

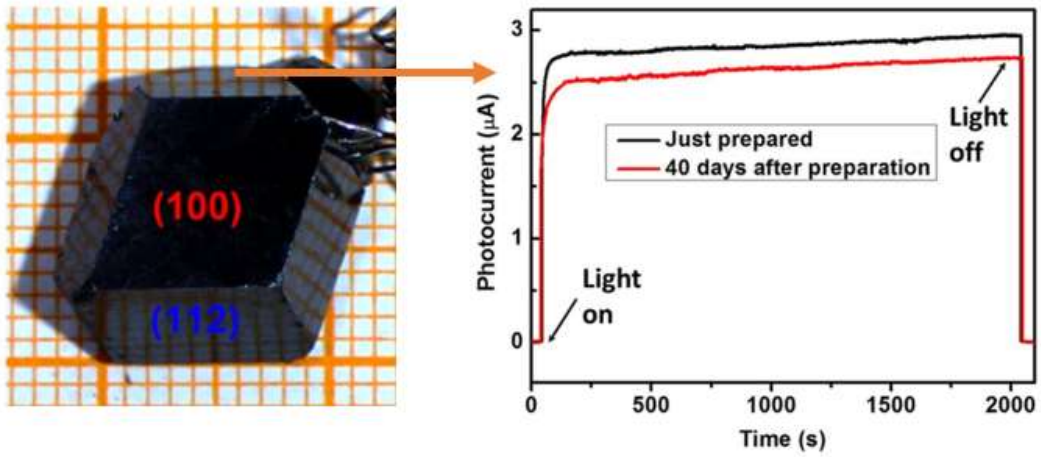

Figure 2-5 Photograph of a $MAPbI_3$ Perovskite bulk single crystal and stability performance [9]

It is worth mentioning that the solution-processed $CH_3NH_3PbI_3$ perovskites provide bright routes for fabricating photodetector devices with low cost and high performance [8], [9], [60]. Also, among the other forms of lead halide base perovskite, the methylammonium lead triiodide is being researched as a potential viable option because of its appropriate direct band gap [61], large absorption coefficient [62], long-range balanced electron- and hole-transport lengths [33], [63], high charge carrier mobilities [63], [64], and its stability as previously discussed. In a stability comparison of single crystal and polycrystal perovskite devices, high stability was observed based on perovskite crystal structure.

The long-term stability of perovskite optoelectronic devices is an important issue for their commercialization and technological development for applications where $MAPbI_3$ would be an appropriate material. It is also important to study the stability of the perovskite in response to changes in the environment including electric fields, humidity, temperature and photo-stability. Despite further study being required, the device architecture and interfaces in $MAPbI_3$ perovskite optoelectronic devices have been shown to improve and control the device stability in the conditions the tests were completed in.

2.3 Working Principle of Lateral Structured Photodetector

The lateral-structured photodetector can work as a photodetector and photodiode as well. As seen in Figure 2-6, the working principle of the perovskite-based photodetector is that the electron-hole pairs are generated upon illumination with photon energy and the photogenerated carriers accumulate at the transport-layer/electrode interfaces. However, with no light, the energy level of the respective materials in the device can be seen in Figure 2-6(b) where the Schottky barrier is very high and the charge cannot cross the barrier. After the illumination and after applying external voltage bias to the device, the Schottky barrier decreases. The photogenerated hole tends to migrate to the perovskite surface and become trapped, leaving unpaired electrons in the perovskite layer. The unpaired electrons then cross the barrier and contribute to the photocurrent.

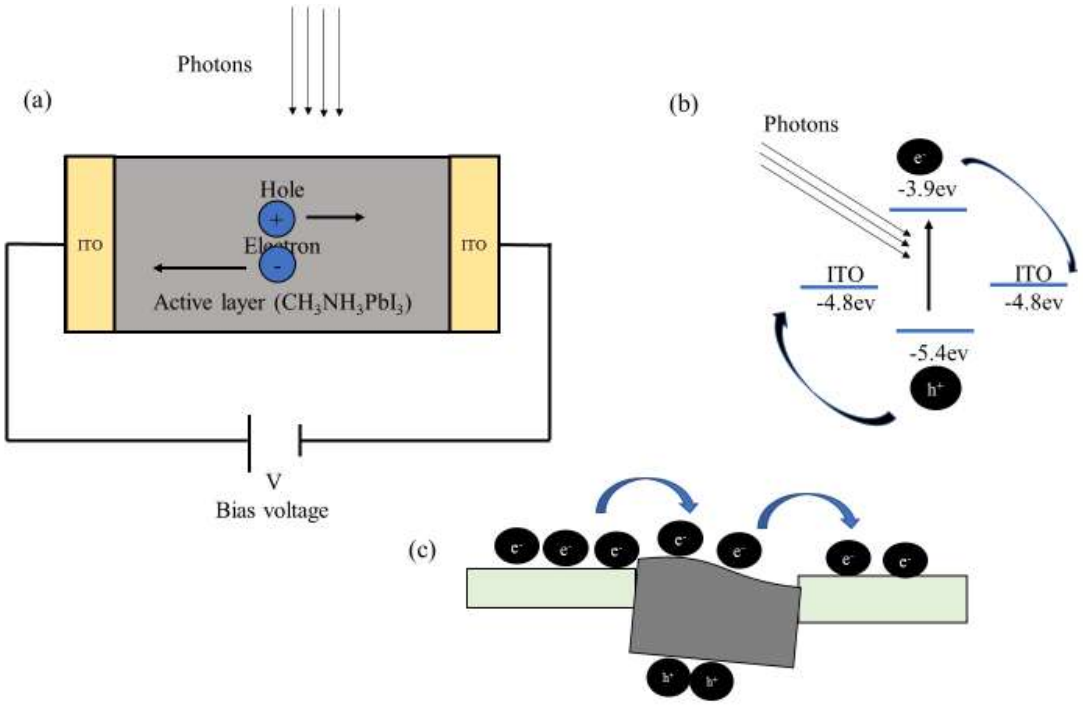

Figure 2-6 (a) Schematic of the Perovskite photodetector and electron-hole pairs generated upon illumination, (b) Energy level diagram of ITO and $CH_3NH_3PbI_3$ materials with no illumination, and (c) Under illumination and voltage bias, photogenerated holes migrating to the surface and being trapped, and unpaired electrons contributing to the photocurrent [41].

In photodetectors, the photocurrent increases significantly in reverse bias. The incident power to current efficiency (IPCE) can be higher than 100% in a photodetector. The photogenerated charge by illumination is added with the injected charge by electrodes under an applied bias.

2.4 Summary

This chapter has provided the basic information of $CH_3NH_3PbI_3$ based perovskite materials and its crystal structure in thin film. A crystallized thin film is created by one of several different processes and used in optoelectronic devices. The applications of single crystal structure of perovskite material in photodetectors and a stability comparison with microcrystalline perovskite thin film have also been discussed. Finally, the chapter provided its working principle in lateral-structured photodetector devices.

Chapter 3 Morphology Engineering of Methyl Ammonium Lead Iodide Thin Films

In this chapter, we present the properties of perovskite thin films fabricated with the blade casting technique, termed solution shearing method, using dimethyl sulfoxide (DMSO) as our solvent of choice.

3.1 Film Morphology Characterization Techniques

In order to determine the effects on film morphology, uniformity and crystal structure, we characterized the perovskite thin films by Optical Microscopy (OM), X-Ray Diffraction (XRD), and Profilometry. Morphology engineering directly influences the quality of electronic devices. With larger crystal grains, we can achieve efficient photodetectors with superior photo response and long-term stability.

3.1.1 Optical Microscopy (OM)

With OM, we were able to visually assess the quality of the films and their micrometer grain and crystal features. We were also able to identify the millimeter size crystal domains in the film and the films roughness using this technique. The grain boundaries in the film were mainly identified through the lower magnification (4X) in OM. The software OMAX Topview was used to record the images of our perovskite films.

3.1.2 X-Ray Diffraction (XRD)

X-ray diffraction (XRD) measurement, depicted in Figure 3-1, was used to identify the crystallinity properties of our thin films. XRD enabled us to identify the type of materials present in the solid films including unwanted impurities and the orientation of the crystals present in the films. Theoretically, the crystals orientation can be determined using Bragg's law as depicted in the Figure below.

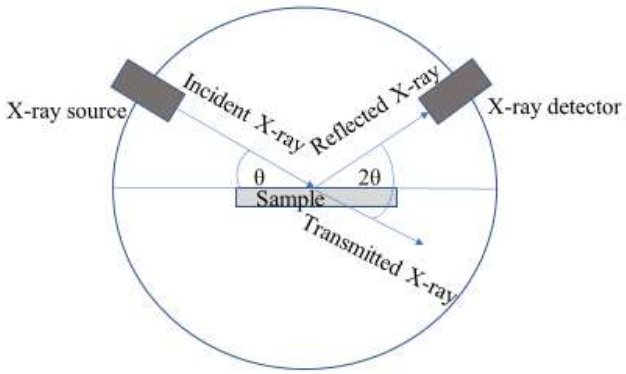

Figure 3-1 Schematic diagram of X-ray diffraction measurement

Bragg's law is determined using the following equation:

$$n\lambda = 2d\sin\theta$$

where;

n is an integer,

λ is the wavelength of incident radiation from the instrument,

θ is the angle of incidence of X-rays relative to the planes of the sample and

d is the separation distance between atomic planes.

The Bruker X-ray D8 ADVANCE Eco diffractometer, situated in the C building, is equipped with a CuKα radiation source and high-speed energy-dispersive LYNXEYE XE-T detector used to identify the crystal orientation. The perovskite thin film substrates were fitted into the individual sample holders, and the film holders were mounted into the instrument. In the XRD measurement, the receiving slit width was 0.6 mm. Finally, the data was collected through the DIFFRAC software package. The step size was set at 0.05 and the time per step was set at 0.1 s during sample scanning.

3.1.3 Profilometry

The Dektak-150 is a standard equipment used for surface topography, roughness, and step size measurements. We used the profilometer to measure the thickness of our perovskite thin films. We prepared the thin films by clearing the perovskite layer and making a straight line in the center of the film. We ran the tip (stylus) of the profilometer over the line at 90 degree horizontally and scanned the surface over that clean line. The schematic diagram in Figure 3-2 explains how it works; the tip diameter is 12.5 micrometer.

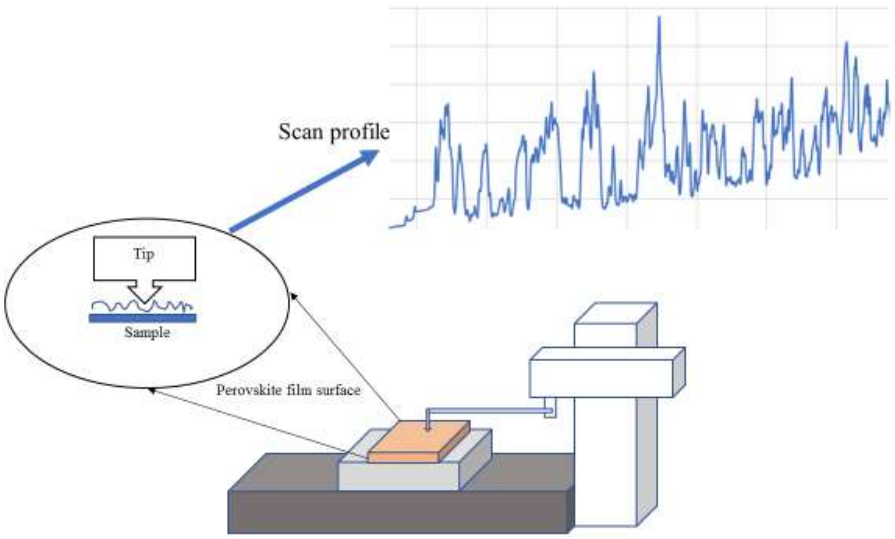

Figure 3-2 Schematic diagram of perovskite film thickness measurement system with a profilometer

The scanned distance was more than 1100 micrometers. In Figure 3-2 and Appendix 1 Figure A 3-1 explains how the scanned data allows us to evaluate the thickness of our film. We took the average of multiple point data to get the approximate thickness of our blade-coated sheared film.

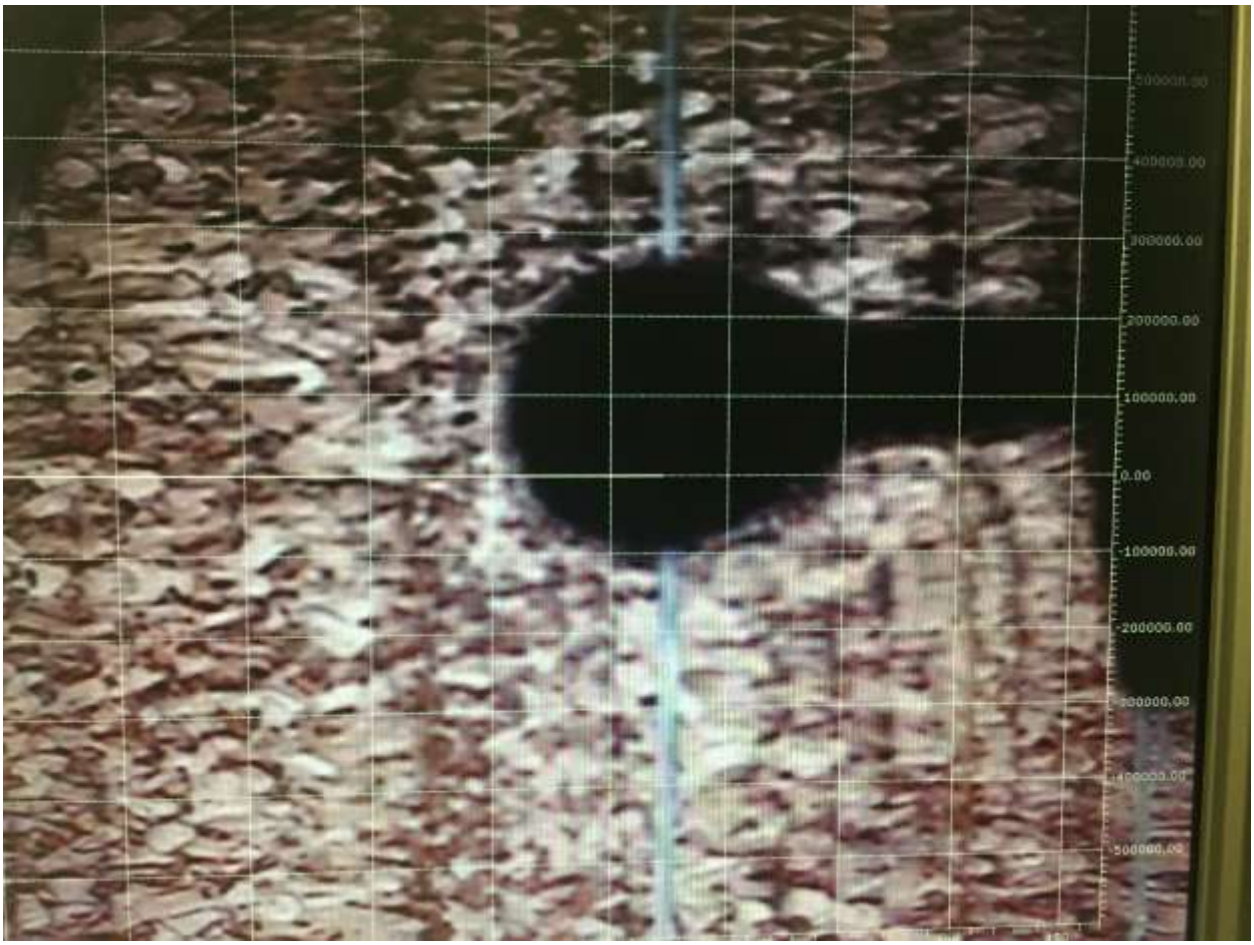

Figure 3-3 Photograph of perovskite film thickness measurement using profilometry

3.2 Thin Film Deposition Techniques

In Figure 3-4, we illustrate the deposition of the precursor perovskite solutions via both the blade coated shearing and the spin coating techniques.

The spin coating technique is one of the most common techniques for depositing solutions onto substrates and creating thin films. For perovskite solutions, the spin coating technique is widely employed in industry and technology sectors. By controlling the spinning speed, time and acceleration, the thickness and morphology of the films can be varied. More

specifically, for our perovskite solutions, we placed the solution on top of the substrate and we ran the spinning at a speed of 1000 rpm and 2000rpm for 10 second and 20 second, respectively. Once we got a uniform coating, we placed the substrate on a hot plate to facilitate solvent evaporation and further crystallization. After the samples have dried, we obtained our final perovskite thin films. As depicted in

Figure 3-4 (left), when using the spin coating technique, the crystal grains in the films were less than twenty micrometers in size.

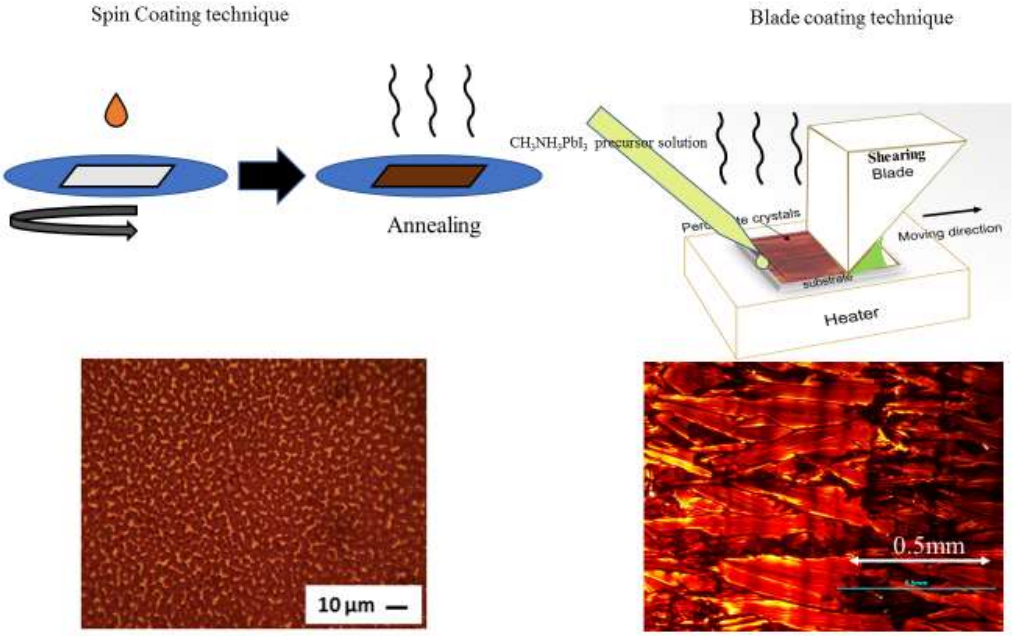

Figure 3-4 Illustration of solution spinning (spin coat) (left), and blade coating technique (right)

In Figure 3-4 (right), the blade coating technique is depicted with the resulting film morphology. During the process, we spread the perovskite solution in between the angled silicon blade and the substrate. There is a stationary translational stage that controls the blade ‘s movement forward over the substrate enabling the uniform deposition of the solution onto the substrate. We can control the blade speed using a computer program. We can also control the gap between the blade and the substrate. During blade coating, the substrate was heated at a specific controlled temperature. Perovskite solution of 60 microliter volume is placed in between the blade and substrate. We typically used speeds of 0.125 mm/sec and 0.15 mm/sec. By controlling the speed of the blade and temperature of the substrate, we can control the crystal size and thickness of the films.

Once the films were formed, we transferred the samples into the glovebox under nitrogen environment. We then placed the substrate on a hot plate at 100C for 20 min to facilitate solvent evaporation and further crystallization. After complete solvent evaporation, the films werecomposed of large crystal grains which are parallel to the shearing direction. This technique can produce mm size grains with preferred crystal orientation within the entire film.

In contrast, deposited spin-coated perovskite films have more grain boundaries and much smaller polycrystalline structures. It has been widely reported that recombination centers are more significant when there is increased disorder in the films. Those carrier trap centers that are present at the grain boundaries not only increase recombination losses but they have also been reported to be the centers that facilitate rapid degradation due to moisture

and oxygen [65]. In Appendix 1 Figure A 3-3 and Figure A 3-4, we include SEM images of spin-coated films and structure analysis.

Using the blade coating technique instead of spin coating, we can grow large crystal grains oriented in a specific direction of the blade movement. The shearing technique directly increases the crystal size and decrease the areas of grain boundary thereby reducing carrier traps and degradation sites in the entire film. In chapter 5, we will describe how these features directly affected the performance of our photodetectors by significantly minimizing recombination losses and increasing the stability of the devices.

3.3 Methylammonium Lead Iodide Perovskite Material Processing

In this section, we describe the preparation and chemical processing of the perovskite precursor solutions for the fabrication of methylammonium lead iodide perovskite ($CH_3NH_3PbI_3$) photodetectors.

Three-dimensional organic-inorganic hybrid perovskites materials have significant capability to make higher efficiency optoelectronic devices such as perovskite solar cells, light emitting diodes, photodetectors and photodetectors using low-temperature solution-processing methods. Innovative materials processing and engineering is the key to achieve this goal. Device configuration along with the electronic properties of the film determines the physics and operating mechanismof of an organic-inorganic perovskite photodetector. The three-dimensional hybrid perovskite material we selected for our study consists of methylammonium iodide and lead iodide (CH_3NH_3I and PbI_2) precursors.

3.3.1 Reagents

Two separate precursors, methylammonium iodide (CH_3NH_3I) and lead Iodide (PbI_2), were used to make homogeneous solutions for the perovskite thin-films, presented in Figure . We used commercially available high purity reagents (lead iodide, Alfa Aesar, ultra-dry, 99.99% and Methylammonium iodide 98% grain, CAS: 14965-49-2). The perovskite precursor materials were dissolved into dimethyl sulfoxide (DMSO) solvent to make $CH_3NH_3PbI_3$ perovskite solutions.

3.3.2 Solutions Preparation

Methylammonium lead iodide perovskite solution (0.3M) was made for blade-coating technique using dimethyl sulfoxide (DMSO) solvent. On the other hand, perovskite solution concentration was set at 1M for spin coated perovskite films as it is common in published literature. As presented in Figure 3-5, a 0.3M of perovskite solution was prepared with, 47.4g of CH_3NH_3I (MAI) and 138g of lead iodide (PbI_2) dissolved into 1mL of solvent. The mixture of perovskite materials and solvent was kept on the hot plate with a stir bar for a minimum of 12 hours at 70 ^oC. A perovskite film with mm size crystals were achieved using the blade-coated shearing technique as presented in Figure 3-6.

Figure 3-5 $CH_3NH_3PbI_3$ Perovskite solution

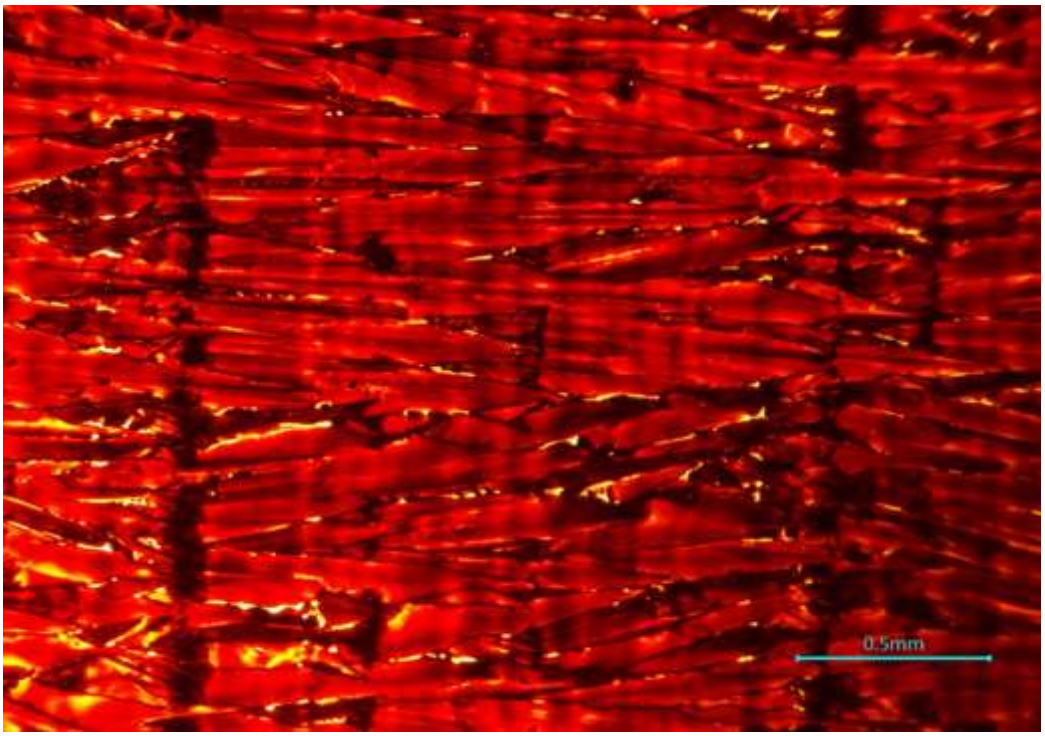

Figure 3-6 Perovskite single crystallized thin film viewed in transmission mode under an optical microscope (4X Magnification)

3.3.3 Perovskite Film Fabrication

The glass substrates were sonicated by deionized water (DI-H_2O) mixed with triton soap, followed by deionized water DI-H_2O, acetone, 2-propanol (IPA) and finally again by DI-H_2O. Each sonication round was set to twenty minutes. The substates were dried using nitrogen gun.

Once dry, the substrates were placed in an Ultra-Violet Ozone (UVO) treatment chamber for twenty minutes as the last step of the cleaning procedure. In the blade coating technique, the 0.3M perovskite solution was carefully deposited between the substrate (kept at 150 ^oC), and the blade typically moving at a speed of 0.125 mm/sec. The substrate holder plate can be heated to a maximum of 300 ^oC during the solution casting. The blade gap (typically between 20 to 500um) and blade coating speed were varied to achieve the optimal thickness of perovskite thin film. The shearing process was done in ambient conditions in a fumehood with the humidity maintained under 20%.

The reference perovskite films were spin-coated inside the glovebox under nitrogen condition as widely reported in literature to prevent instant degradation. The 1M of DMSO-based perovskite solution was prepared in a glovebox and stirred overnight at 70^oC. We spin-coated 250 µl of hot perovskite solution at 2000 rpm for 10 s and at 4000 rpm for 40 s. During the spin, 200 µl of chlorobenzene was deposited with 5s remaining and spun for 5 s. The finished samples were annealed under nitrogen condition at 100^oC for 30 min.

3.4 Morphology Control and Characterization

The morphology of $MAPbI_3$(MA= CH_3NH_3) perovskite thin films was modified by using different deposition techniques. The spin-coated perovskite film demonstrates less than 20 micrometer crystalline structures as presented in Appendix 1 Figure A 3-2, which are far smaller in size than the ones fabricated with shearing film as presented in Figure 3-4.

In the blade coating technique, the perovskite morphology was controlled by varying parameters like metal plate temperature, blade gap and shearing speed. We first demonstrate the effect of varying the plate temperature on the film morphology: the metal plate temperature was varied from 140 °C to 170 °C with speed held constant at 0.15 mm per second as shown in Figure 3-7. The effect of temperature on the directional crystal growth technique was observed using OM and SEM. As presented in Figure 3-7, the crystal grain size increased with the temperature. We were careful not to apply a temperature higher than the boiling point of the solvent employed (~170 °C for DMSO) and thus we avoided burning of the film. The temperature dependent solvent evaporation rate clearly controlled the growth process of crystallized perovskite grains [11]. As depicted in Figure 3-8, the morphology of the film is also dramatically affected by the coating speed.

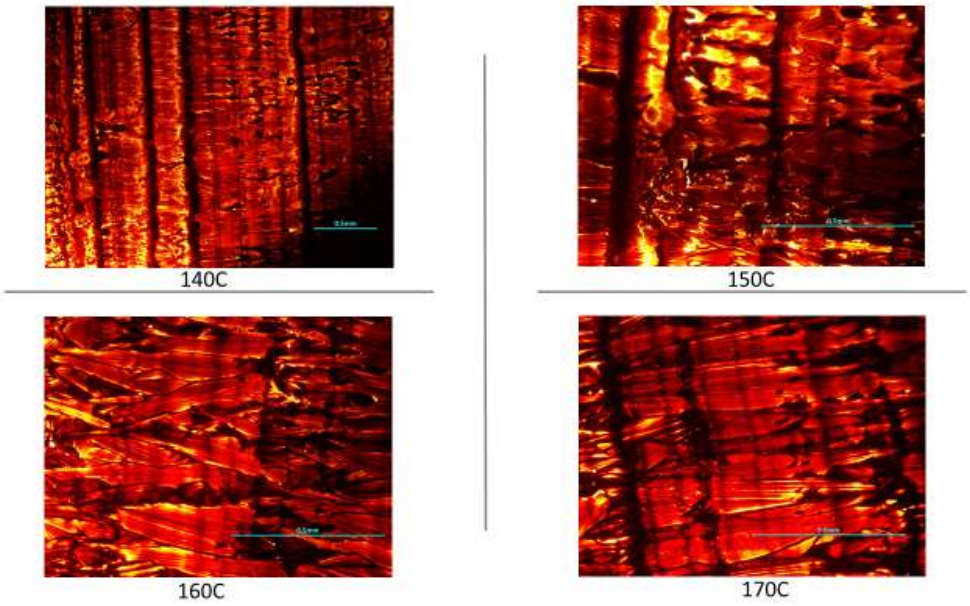

Figure 3-7 DMSO based sheared perovskite thin film surface morphology at a different temperature with a speed of 0.15mm/sec

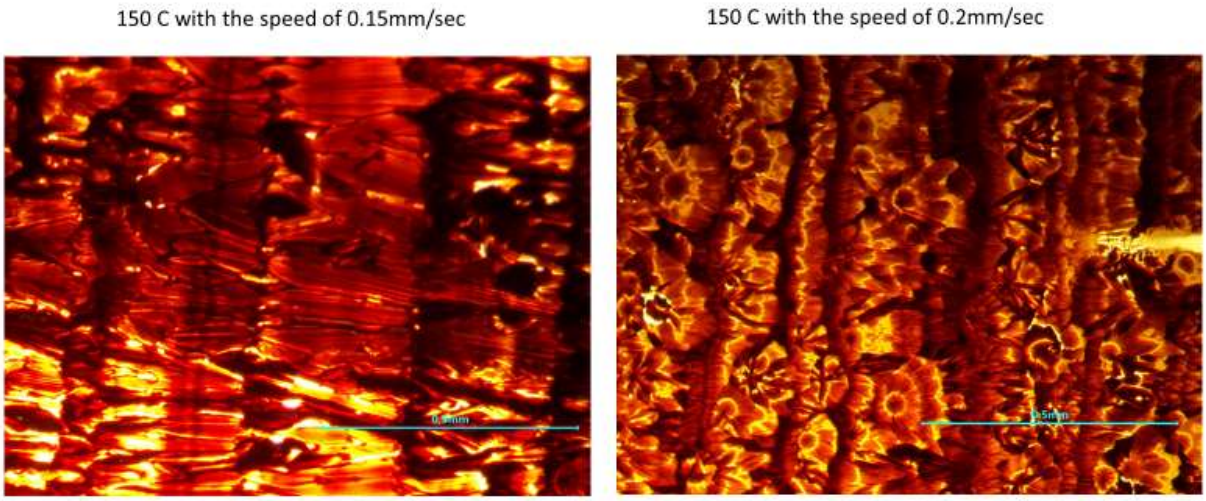

Figure 3-8 Crystal size and morphology is changing with varying the blade coating speed

The blade coating speeds affects the layer thickness and the crystallized structure in the perovskite film. A constant metal plate temperature of 150 °C was applied for different speeds such as 0.15mm/sec and 0.2mm/sec. The crystal size decreases with increased blade coating speed as presented in Figure 3-8. A speed of 0.15 mm/sec produced larger crystal grains than 0.2mm/sec shearing speed as we see in the OM images. Smaller crystal domains were achieved at 140 °C and 150 °C than at 160 °C and 170 °C as we see in Figure 3-7 with a higher speed [11].

There exists a relationship between the temperature of the metal plate and blade coating speed. A slow blade coating speed and high temperature burned the crystal grain boundary

in the perovskite film as depicted in Figure 3-9. We used a high temperature of 180 °C and the burned morphology and grain boundary in the film are visible in the OM image as presented in Figure 3-9.

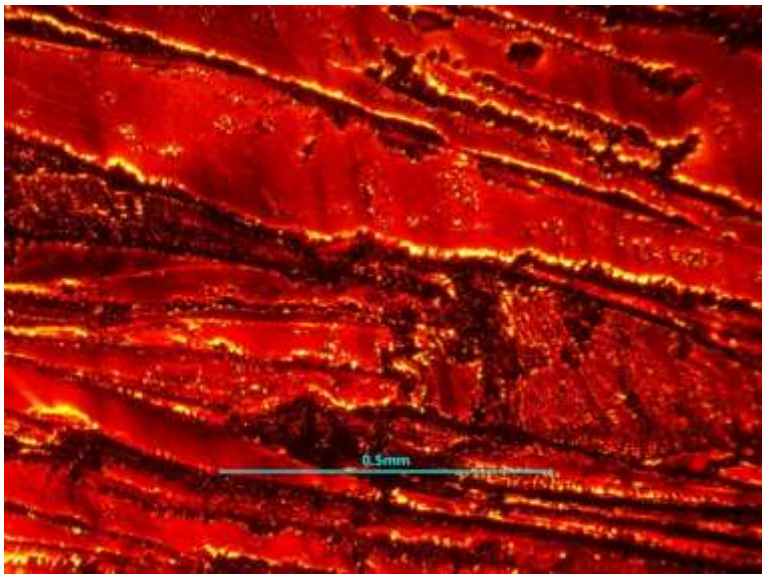

Figure 3-9 OM image of the solution sheared film at 180 °C (0.15mm/sec)

In general, we found a the relationship between the metal plate or solvent evaporation rate and constant blade coating speed was investigated and is illustrated in Figure 3-8. The crystal grain size increases linearly with the temperature in the range of 140 °C to 190 °C. On the other hand, the grain size decreases linearly with inceasing the blade coating speed at a constant substrate temperature. When a shearing speed of 0.15 mm/sec and temperature 160 °C was applied, an optimal film with large size grains is formed as presented in Figure 3-8 and Figure 3-9.

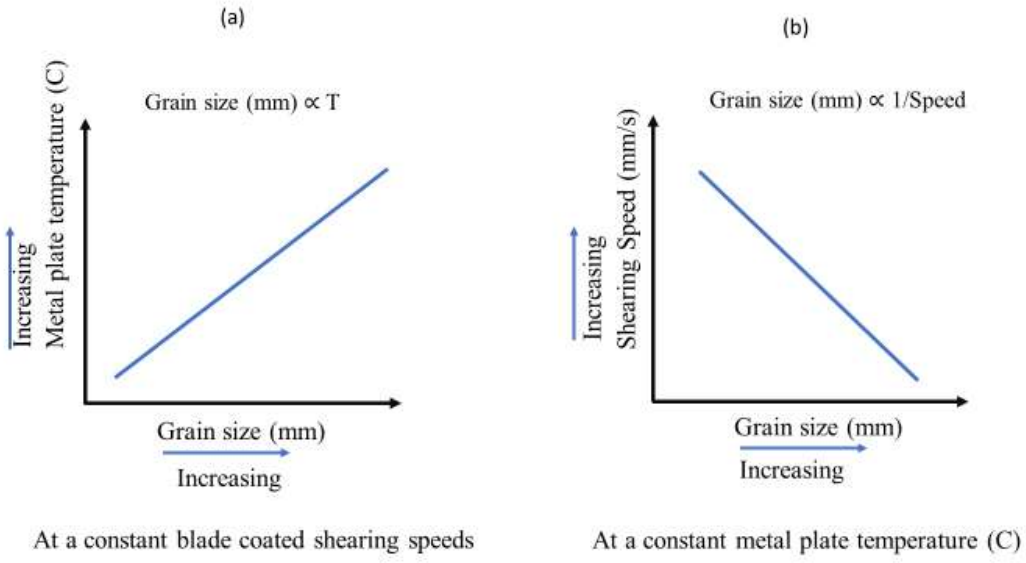

Figure 3-10 Relationship between the temperature, blade coating speed, and crystal grain size

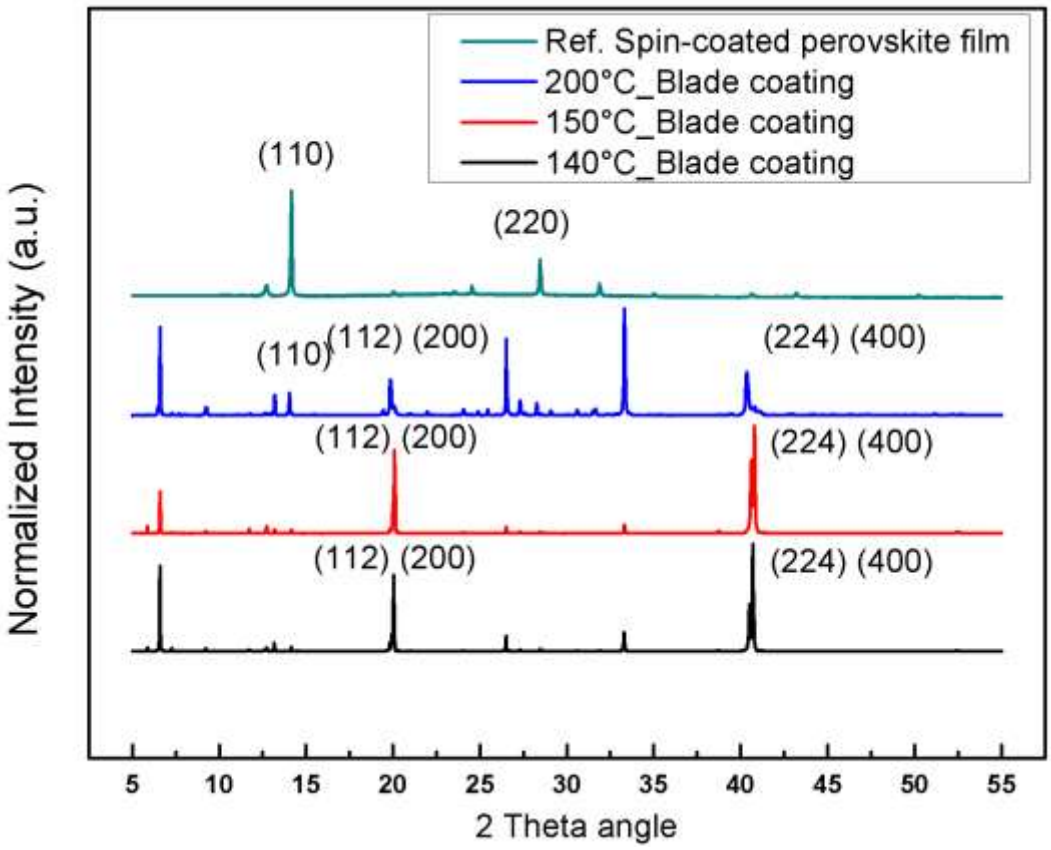

Figure 3-11 XRD diffraction pattern of DMSO based spin-coated and blade-coated perovskite film.

We charaterized our films with XRD to confirm their crystal structure and orientation. The perovskite films were fabricated at different temperatures (140 ºC to 200 ºC) and compared with the reference spin-coated film. In Figure 3-11, we show the different X-ray diffraction profiles of blade-coated and spin-coated perovskite film.The X-ray diffraction pattern of solution sheared perovskite film confirmed the presence of tetragonal phase at a different orientation plane than the spincoated film. At a low temperature of 140 °C and 150 °C, sharp peaks were observed at 2θ=20° degree, and 2θ=40.42º degree corresponding to (220)

and (224) planes respectively. The doublet peak was also present at the 2θ angle of 40.42° and 40.64° which may have been caused by crystal stretching during blade coating and heating of the perovskite film. The doublet diffraction strong peaks appeared at 2θ=19.90° and 20° corresponding to (112) and (200) planes, respectively, and at 2θ=40.42° and 40.64° corresponding to (224) and (400) planes, respectively. From XRD, we conclude that the sheared coated crystal domain mainly orientated along the (112) or (200) directions which are parallel to the substrate. On the other hand, the spin-coated perovskite film was showing the regular diffraction peak intensities at (110) and (220) planes which matched well with earlier reports [66]. In perovskite films made at high temperature, PbI_2 peaks appeared in the X-ray diffraction pattern indicating burned reagents. At the same time, additional diffraction peaks appeared at a lower temperature which correspond to unreacted PbI_2 impurities peak intensities. For morphology investigations, we attempted to perform the XRD on different perovskite film to look at the evolution of the peaks, as presented in details Appendix 1.

Furthermore, we attempted to use various solvent with different boiling points to see the effect on the crystal structures in the films. The $MAPbI_3$ based perovskite materials were mixed into a different volume ratio of N-Methyl-2-pyrrolidone (NMP) and DMSO solvent. The details of this study are given in Appendix 1. We also employed various mixtures of DMSO with the high boiling point Gamma-Butyrolactone **(**GBL and the results are presented in Appendix 1. Herein, we briefly present in Figure 3-12 the effects of using different solvents on morphology and compare them with a spin coated film.

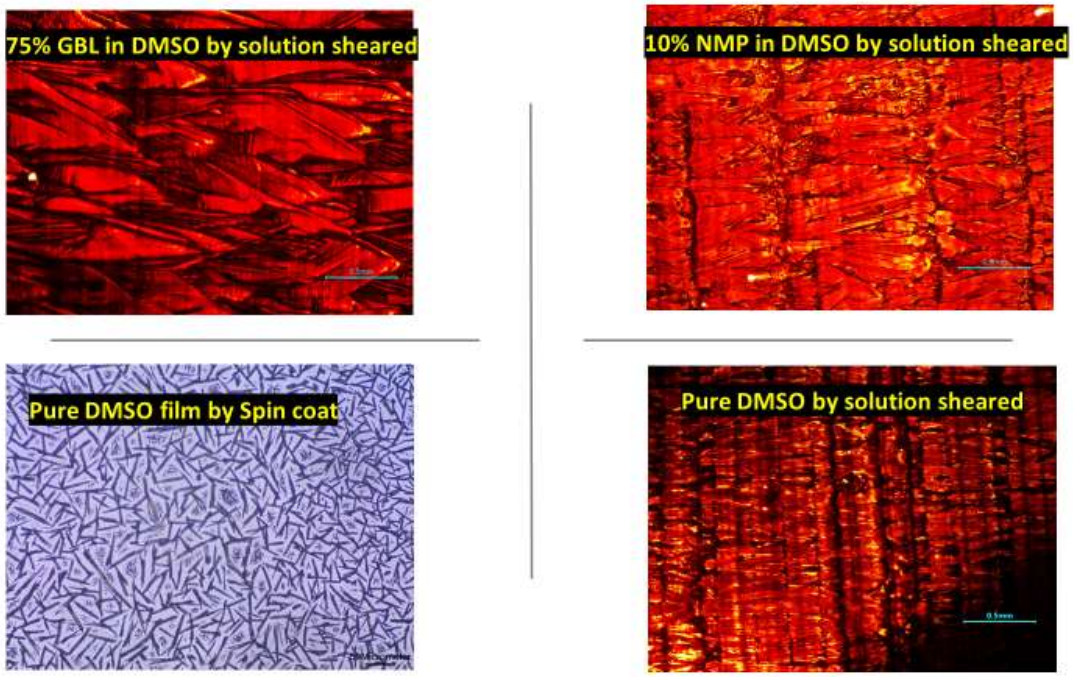

Figure 3-12 Comparison in between spin coated and mixed solvent based sheared perovskite film

3.5 Summary

In this chapter, the blade coating and spin coating processes were described employing the processes of perovskite film, structural analysis with XRD, and film thickness measurement techniques used in this work. These processes allow for insight of properties of the perovskite films and materials. The detailed morphological characterization of blade coated perovskite film is analyzed in Appendices 1 through 4.

Chapter 4 Optical and Electrical Characterization Setup

High-performance organic lead-halide perovskite photodetectors and their electrical properties have been an attractive field of research [8]–[10], [26], [54]–[56], [58], [60], [67]. In this chapter,

the fabrication of efficient methylammonium lead iodide thin film photodetectors and their electrical characterization will be discussed. This chapter also describes the fabrication and measurements of lateral structured photoresistors which showcase the electrical anisotropy of the crystalline structures used.

4.1 Ultraviolet-Visible (UV-Vis) Spectroscopy and Film Absorption

UV-Vis spectroscopy was used to measure the absorption and transmission properties of our perovskite thin films. The difference between the conduction band and the valence band, the bandgap of the material, is determined from the onset of the absorption spectrum and is determined using the following equation,

$$E_g = h*c / \lambda_{onset}$$

Where;

h is Planck's constant valued at 4.136×10−15 eV·s, and

c is the speed of light in a vacuum and is equal to 2.998×10^8 m/s.

For the various perovskite films evaluated in our work, the UV-Vis absorption spectra were obtained using Agilent Cary 7000 with the Cary Scan software program. After measuring the base with a blank sample, the perovskite solid thin films were mounted vertically into the instrument with the glass side facing the detector source. Finally, the absorption and transmission spectra were obtained by scanning the source wavelengths from 300nm to 900nm.

This method shows the absorption capability of photon energy in a perovskite film. A block diagram of absorption spectroscopy is depicted in Figure 4-1. In general, a light source at different wavelengths is passed through the monochromator. This incident light beam hits the sample, which absorbs most of the light in the UV-Vis spectrum. The decector then detects the light signal and converts it to a digital signal to store in the computer.

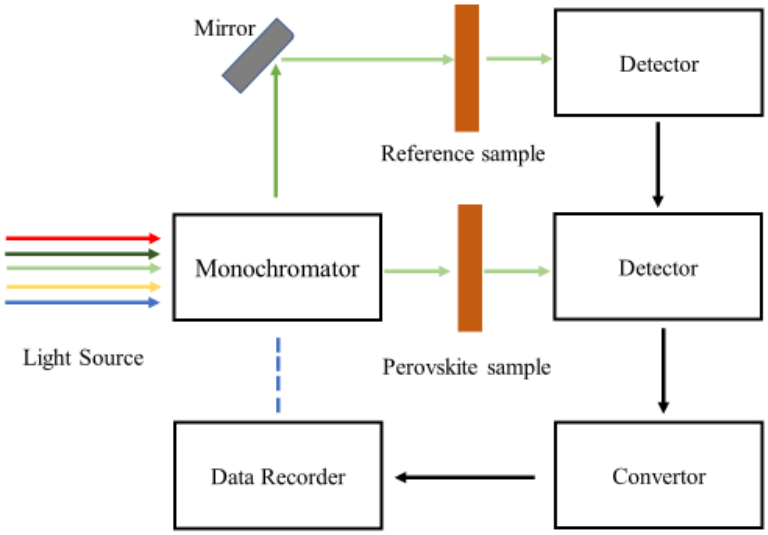

Figure 4-1 Schametic diagram of UV-Vis spectroscopy for absorption measurement in perovskite film

4.2 Photoluminescence (PL) Spectroscopy

The term photoluminescence (PL) is associated with the emission of photons following photoexcitation. Photoexcitation occurs when electrons are excited to higher-energy states upon the absorption of incident light energy. A photoluminescence (PL) instrument detects the photon's radiation when the photons are re-radiated after the electrons relax to the ground state. High energy photons irradiate the samples during the PL measurement, and the emission spectrum is then recorded. The perovskite thin films were mounted vertically into the instrument as explain in schematic Figure 4.2. The film side faced the radiation

source, and the excitation wavelength was selected at 650 nm for the emission experiment with a scan rate of 600 nm/min.

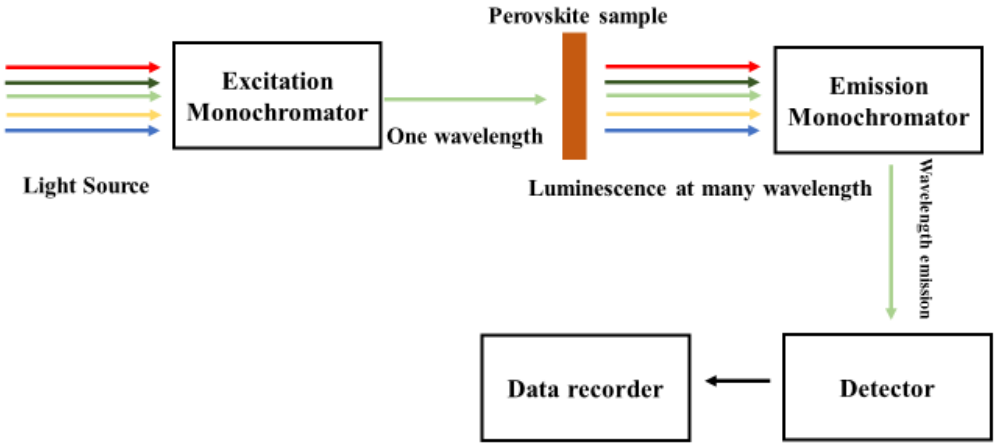

Figure 4-2 Simple schematic block diagram of sample photoluminescence in spectroscopy

4.3 Time-Resolved Photoluminescence Spectroscopy (TRPL)

Time-resolved photoluminescence spectroscopy (TRPL) was used to investigate the charge carrier lifetime within the different perovskite thin-films. TRPL measures the intensity of light, which is proportional to the number of photons emitted by a sample over time, the transient response, when it is excited by a laser pulse. The schematic diagram is presented in Figure 4-3 and the setup of TRPL in lab was demonstrated by Daphne in Dalhousie University's Department of Physics and Atmospheric Science.

A specific laser of 640 nm wavelength was used for the excitation, and the transient PL intensity was recorded. If the laser pulse has an energy higher than the bandgap energy of the material, then the electrons absorb that energy, recombines, and emits a photon. The peak of the PL is observed when the laser hits the sample. Over time, the sample response decays as carriers start to recombine and radiate.

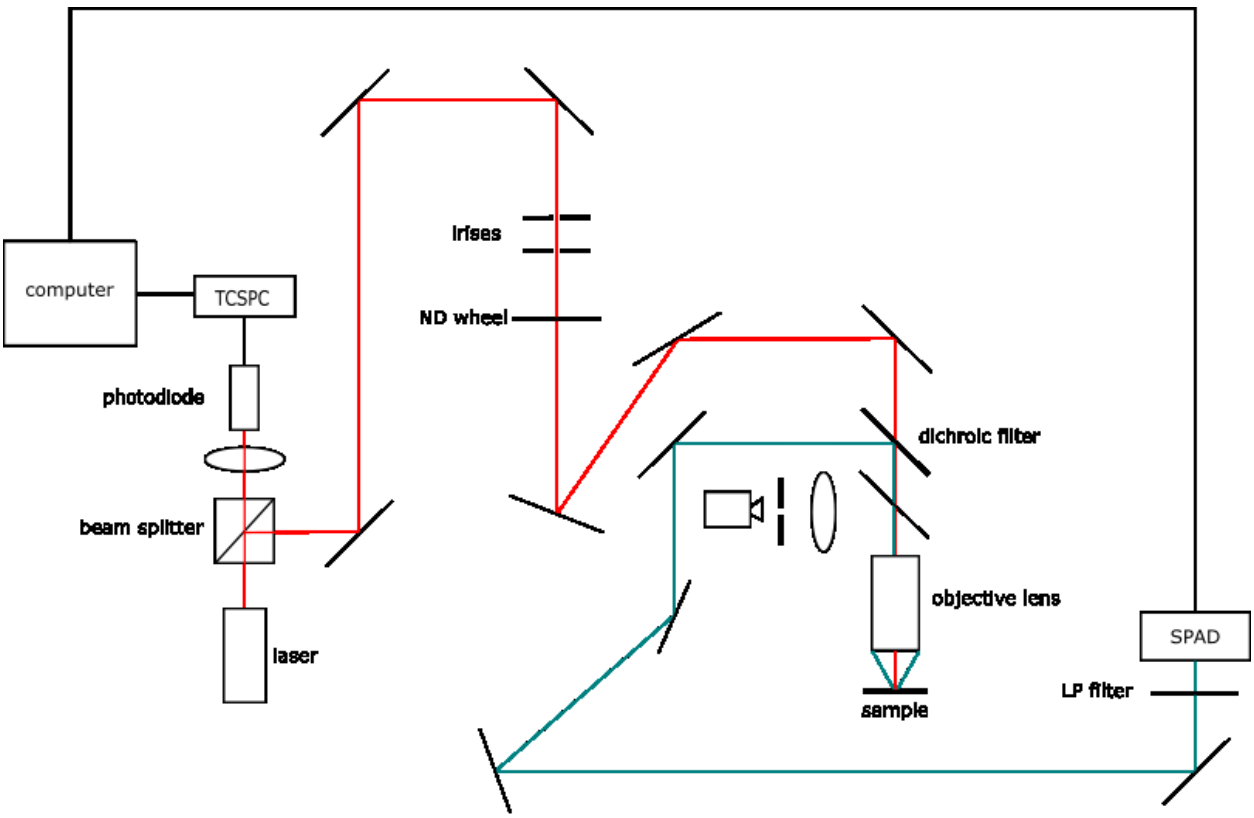

Figure 4-3 Schematic diagram of PL decay measurement setup from Dr. Kimberly's lab

During the measurement, the perovskite films were placed under an objective lens which focused the incident laser pulse on the sample. The laser beam (640 nm) was passed through a beam splitter and into a photodiode. A signal was then sent to the Pico Quant Picoharp 300 time-correlated single photon counting module (TCSPC). That signal when received tells the machine to start counting photons. The laser then follows a path until it reaches the sample, where the PL emitted goes into the objective. The emitted light was passed through a dichroic filter to the single photon avalanche photodiode (SPAD), which emits a signal every time photons go through. Those signals are in turn sent to the TCSPC, which counts them.

The data counts from many photons were collected over time, and the data was then sent to the computer for processing. A software program Picoharp 300 was employed to see the counts. Then, the double exponential fit equation was used to measure the results and generate the graphs of the response.

A maximum charge carrier lifetime of 53 ns is achieved from a thicker (above 1 micrometer) blade-coated perovskite crystal grain fabricated at a temperature of 170 °C. Further details are available in Appendix 3. The lowest carrier lifetime obtained from spin-coated perovskite film will be discussed in Chapter 5.

4.4 Solution-Processed Photodetectors

The Perovskite materials being studied have attracted a great attention in the field of optoelectronics. In this regard, solution processed photodetectors using methylammonium lead iodide based perovskite materials were fabricated.

The solution process method studied was simple and much more economic than silicon based processes [68], but produced more internal defects in the produced synthetic crystals. To form the precursor solution, PbI_2 and CH_3NH_3I were dissolved into the solvents at a certain stoichiometric ratio, which was directly shear cast on an ITO substrate (interdigitated electrode) to form a perovskite film. The crystal quality and properties of the perovskite layer are closely related to the solvent used, annealing temperature, and annealing time [65].

4.4.1 Device Layout

Fluorine doped Tin Oxide (FTO) and Indium doped Tin Oxide (ITO) coated glass substrates are commonly used for the fabrication of optoelectronic devices [54]. The pre-patterned interdigitated ITO-based glass substrates (20 mm x 15 mm) were purchased directly from the company "Ossila". Figure 4-4 shows the ITO substrate consisting of 30 interdigitated fingers working as an electrode. The electrode thickness is 100 nm. The channel dimensions are 30mm × 50 μm (width × length).

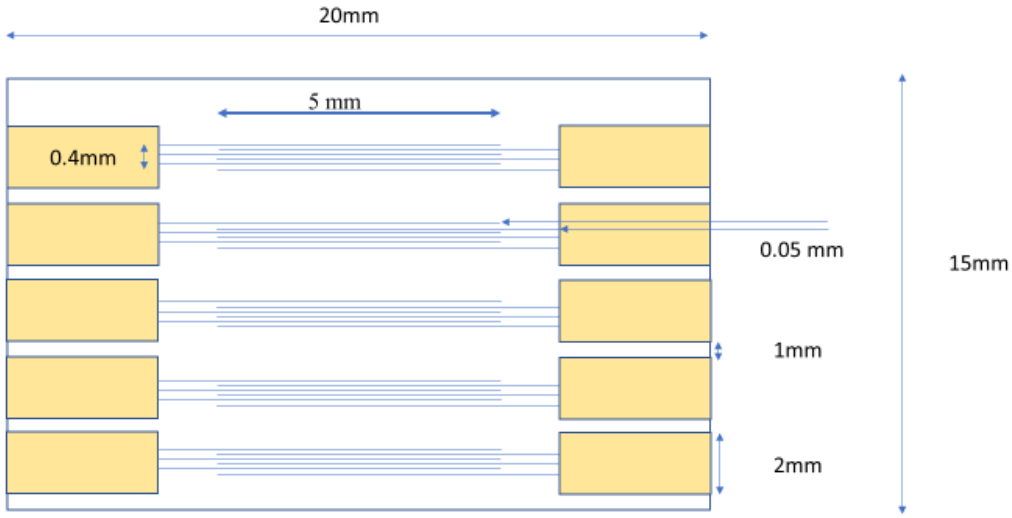

Figure 4-4 Schematic diagram of interdigitate patterned ITO substrate

4.4.2 Device Fabrication

The patterned ITO substrate was cleaned using a fifteen- minute ultrasonic bath in a solution consisting of deionized water (DI-H_2O) and few drops of the detergent "Triton". Following this ultrasonic bath, the substrate underwent an additional fifteen-minutes of sonication in DI-H_2O and 2-isopropanol (IPA). The substrate was then dried using compressed nitrogen gas. The procedure of perovskite film formation on the glass substrate has previously been discussed in Chapter 3.

Once the integrated ITO glass substrate has been cleaned and dried, the perovskite layer was deposited using either the blade-coating or spin-coating techniques. Finally, the $CH_3NH_3PbI_3$-based perovskite photodetector was ready after post annealing.

In the same way, the perovskite film was prepared on 25mm × 25mm glass substrate by blade-coating and spin-coating techniques. After post annealing of the film, the spiro-OMeTAD solution was sheared on this film. A 80 mg spiro-OMeTAD was mixed with 1 mL of chlorobenzene with N, N′-bis(3-methyl phenyl)-N, N′-diphenyl benzidine (TDP), and $Li[(CF_3SO_2)_2N]$ (LiTFSI) dopant. The spiro solution was sheared on the film at a speed of 0.075 mm/sec with no additional heat supplied to the air. The spiro layer was then coated to make better ohmic contact between the gold (Au) electrode and crystallized perovskite layer. The gold electrodes were deposited (~50 nm) in the channel position at a base pressure of 10^{-6} torr using a deposition rate between 0.5 – 1 A/s. Finally, the perovskite photoresistor device was ready.

4.4.3 Photodetector Device Architecture

As displayed in Figure 4-5, the crystallized perovskite structure is deposited in the center of the pre-patterned ITO substrate. The crystallized film generates an electric charge when light is illuminated on the film surface when the device is biased externally. An electrode was connected to the external circuit to transfer the electric signal.

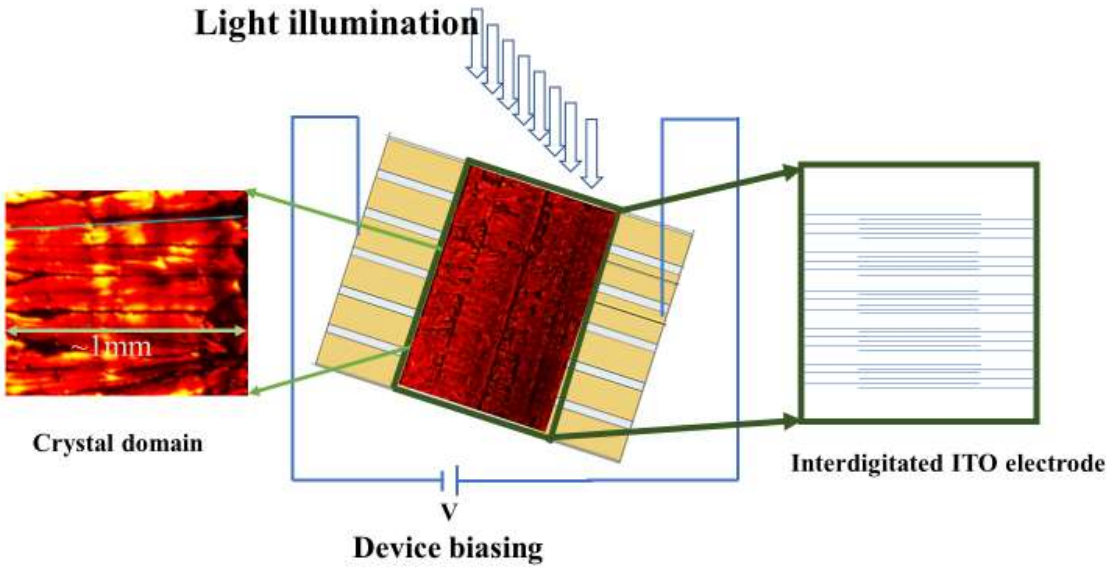

Figure 4-5 Schematic diagram of lateral-structured perovskite photodetector.

4.5 Electrical Device Testing and Performance Metrics

The photocurrent response (I-V) and the speed of time response were measured with a lab setup to characterize the perovskite photodetector. The setup consists of a power supply, a KEITHLEY 2450 SourceMeter, and LEDs of wavelengths 448 nm, 522 nm, 610 nm and 700 nm. These LED wavelengths correspond to the colors blue, green, orange, and red, respectively. In addition, a power supply, frequency generator, and oscilloscope were used to measure the time-responses of the photodetector devices. Before testing the devices, the light intensity was measured using a power meter at a series of different voltage biasing values to the LED. The applied biasing voltages ranged from -5 V to +5 V.

In the perovskite photodetector device, the incident light generates an exciton, and the charge carriers move to the separated electrodes through conduction and valence bands of respective materials as described in Chapter 2. Consequently, these devices generate photocurrent in response to incident light intensity. The figure of merit that is used traditionally to quantify the amplitude of a photo-induced signal is the responsivity (R), [8].

$$R = \frac{I_{ph}}{P_{out}} \qquad [A/W]$$

where I_{ph} is the output photocurrent and P_{opt} is the incident light intensity.

The quantum efficiency (QE) represents the number of incident photons converted to electrical charge which is represented as [69]:

$$EQE\ (\%) = \frac{R\,h\,C}{e\ \lambda}$$

Where,

h is Planck's constant,

C is the velocity of light,

e is the charge of an electron and

λ is the wavelength of incident light.

Responsivity is correlated with EQE by a constant factor depending exclusively on the frequency (wavelength) of the incident signal. The EQE is correlated with the photoresponsivity which can be expressed as:

$$R = \frac{Iph}{Pout} = q.\frac{EQE}{hv}$$

So, it follows that:

$$EQE = \frac{hvR}{q}$$

Where;

q is the elemental charge,

h is the Planck's constant, and

v is the frequency of the incident light.

Detectivity is one of the important parameters of the device that indicates the ability of a photodetector to measure weak optical signals. The detectivity can be expressed as D, where the equation is [54]:

$$D = \frac{R}{\sqrt{2q\ .I_{dark}}}$$

Where,

R is responsivity,

q is the elementary charge, and

I_{dark} is the dark current.

4.6 Electrical Measurement Setup

The block diagram in Figure 4-6 represents the setup of the measurement system of the photodetector devices. The top of the figure shows that the device is connected electrically with the op-amp circuit and trans-impedance amplifier. The setup is then connected with an oscilloscope to gain an output time response of devices. Light is illuminated on the device area to generate an exciton and an external biasing voltage is applied to the circuit, as visible in the bottom part of the figure.

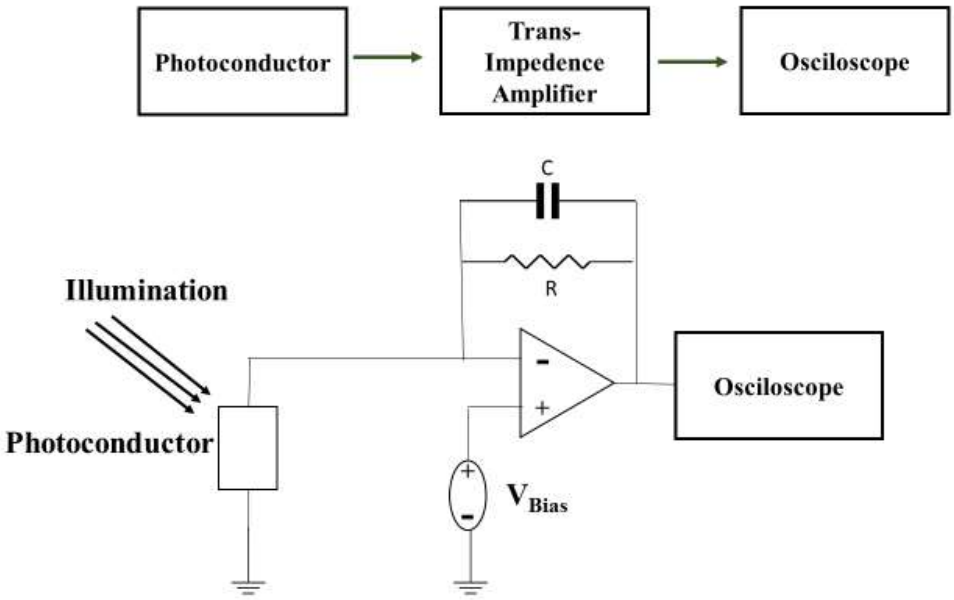

Figure 4-6 Schematic block diagram (top) and the setup of the circuit diagram for Photodetector device measurement (down)

Photocurrent response measurement of the photodetector

A lateral-structured perovskite photodetector device was measured using a semiconductor analyzer (KEITHLEY 2450 Source Meter) in the air under both dark and light illumination. The device area was 0.015 cm^2 to calculate the speed of photoresponse. The photo-response was measured in both scan directions of forwarding voltage bias (-5V to +5V) and reverse voltage bias (+5V to -5V) under low light intensity. During measurement of the photocurrent, the delay time was 100 milliseconds. The different wavelengths of light were illuminated on the device such as blue, green, and red LEDs of 448nm, 522nm, and 700nm

wavelength, respectively. A range of power intensity of 20 nW/cm^2 to 1 mW/cm^2 were applied to strike on the perovskite photodetector device to generate electron-hole pairs. In the meantime, the external low biasing voltage was connected to the circuit during performance measurement. A channel was hooked up using the KEITHLEY Source Meter. Finally, the electrons passed through the Schottky barrier were collected by the electrode, and the generated I-V graph was displayed on the KEITHLEY Source Meter.

4.7 Photoresistance Measurement

Photosensitivity of perovskite thin film is correlated with the illumination of light. The photo resistance decreases with increasing intensity of incident light on the devices. Different colored LED lights were used with different wavelengths and power densities. The photo resistivity was characterized by our blade-coated lateral-structured perovskite photodetector where the perovskite film obtained directional larger crystal grains. A spin-coated perovskite device was used as a reference to make a comparison. As presented in Figure 4-7, the different channel lengths of the gold electrode such as 0.75 mm, 1.5 mm, and 2 mm were used to investigate the grain photoresistivity in the blade-coated sheared and spin-coated perovskite devices. The gold electrode channel was deposited on the perovskite film in parallel, but it was deposited in perpendicular to the crystal grain. The intention of this directional difference was to gain a trend of anisotropy in the blade-coated device. A spiro layer was coated on the perovskite films to make better ohmic contact and to decrease the interface resistance between the perovskite surface and the top electrode. The channel length of 0.75 mm was used in the final spin-coated and blade-coated sheared

devices as depicted in Figure 4-8. Light was illuminated only on those device areas. Three different wavelengths of light were used to measure the performance of the device: 448 nm, 522 nm, and 700 nm for the LED colors blue, green, and red, respectively. A probe station was used to measure the device in a glovebox under dark and light illumination. Light absorption and photoluminescence were also measured for the same devices to improve the findings.

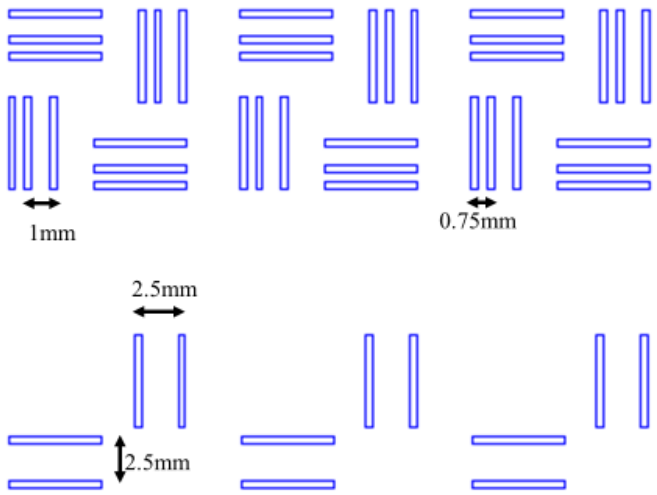

Figure 4-7 Schematic diagram of gold (Au) channel structure on the photoresistor devices

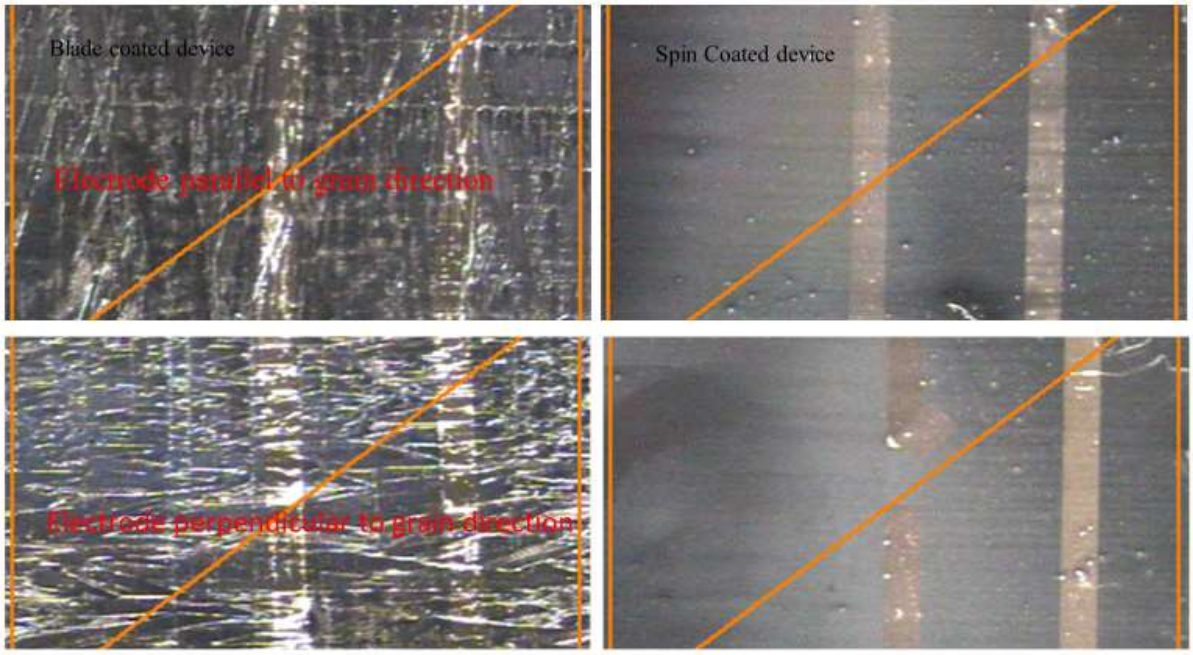

Figure 4-8 Photograph of perovskite photoresistor device, Blade coated (left side) and spin coated device (right side)

4.8 Summary

In this chapter, details of the electrical characterization technique employed to the perovskite film absorption were described. The phenomena of photoluminescence, PL decay were also discussed, as well as photodetector devices. The technique discussed can provide insight of the perovskite materials such as the ones used in this work.

Chapter 5 Optical and Electrical Measurement

The initial analysis of this thesis work will cover individual studies conducted to analyze the film absorption, photoluminescence of perovskite film, time -resolved photoluminescence decay (TRPL), and photo resistance in perovskite films. The chronological presentation of these studies will show the optimized photodetector devices performance (I-V) which leads to a comparison with other processed results. In addition, a comparative analysis of the blade-coated devices responsivity, external quantum efficiency and stability with a reference spin-coated photodetector device is included.

5.1 Absorption and Photoluminescence of Optimized Film

As a reference device, a conventional spin-coated perovskite film has been prepared to compare with a blade-coated perovskite film. As presented in Figure 5-1 (left), the UV-visible absorption spectra of perovskite film are being compared across the techniques of blade-coating and spin-coating. A thicker perovskite layer (~790 nm) absorbs more photons than a thinner perovskite layer (~533 nm). Comparing the spin-coated perovskite film absorption with blade coated film, it is presenting lower absorption then blade coated thinner perovskite film. Photon absorption is dependent on the perovskite film thickness. As presented in Appendix 3's Figure A 5-4A, the higher photon absorption is achieved from blade-coated perovskite film, prepared using a temperature of 150 ^{o}C for a glass substrate.

The photoluminescence (PL) spectra were also measured for the same perovskite film using the excitation wavelength of 522nm. A lower radiative recombination rate (visualized by a lower intensity peak) is seen in spin-coated perovskite film than the blade-coated perovskite film of similar thickness as shown in Figure 5-1 (right side). This result indicates that in the sheared film carriers are not lost to surface traps and imperfections as much as in a spin-coated film.

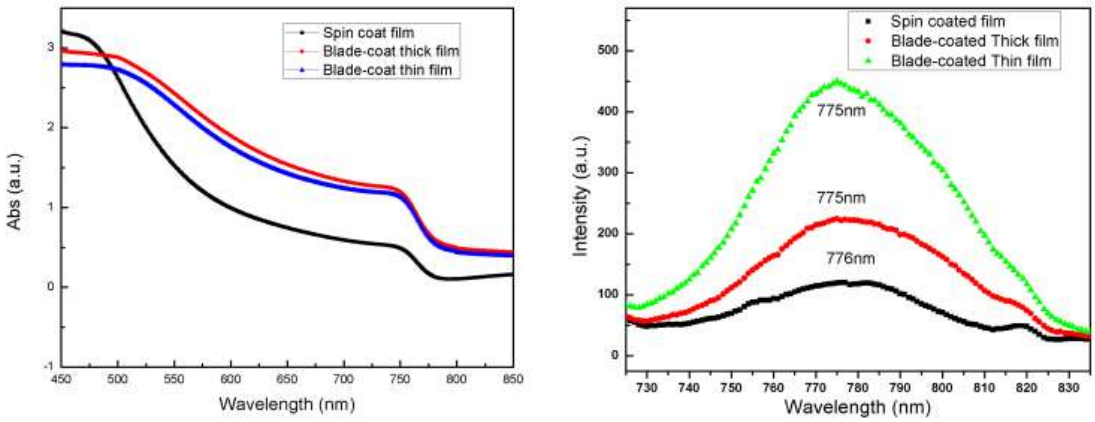

Figure 5-1 UV-Vis absorption of perovskite film by spin-coat and blade coating process (left side) and photoluminescence (PL) of perovskite film (right side)

5.2 Time-Resolved Photoluminescence Decay (TRPL)

TRPL is also used to measure carrier lifetime within the films. The TRPL characterization reveals a superior carrier lifetime in solution-sheared perovskite films compared with the reference spin-coated perovskite films. As presented in Figure 5-2, by using the double fit equation, the carrier lifetime in a blade-coated perovskite crystal grain is about ~46 ns, while for a spin-coated perovskite crystal grain lifetime is ~23.8 ns. As presented in Appendix 3's Figure A 5-1, the measurements employed on various blade-coated perovskite films show carrier lifetimes of ~ 47 ns and ~53 ns in the perovskite grain at temperatures of 160 ^{o}C and 170 ^{o}C, respectively. With larger crystal grain sizes in thicker films, carrier lifetimes increase and take a longer time to be lost to recombination.

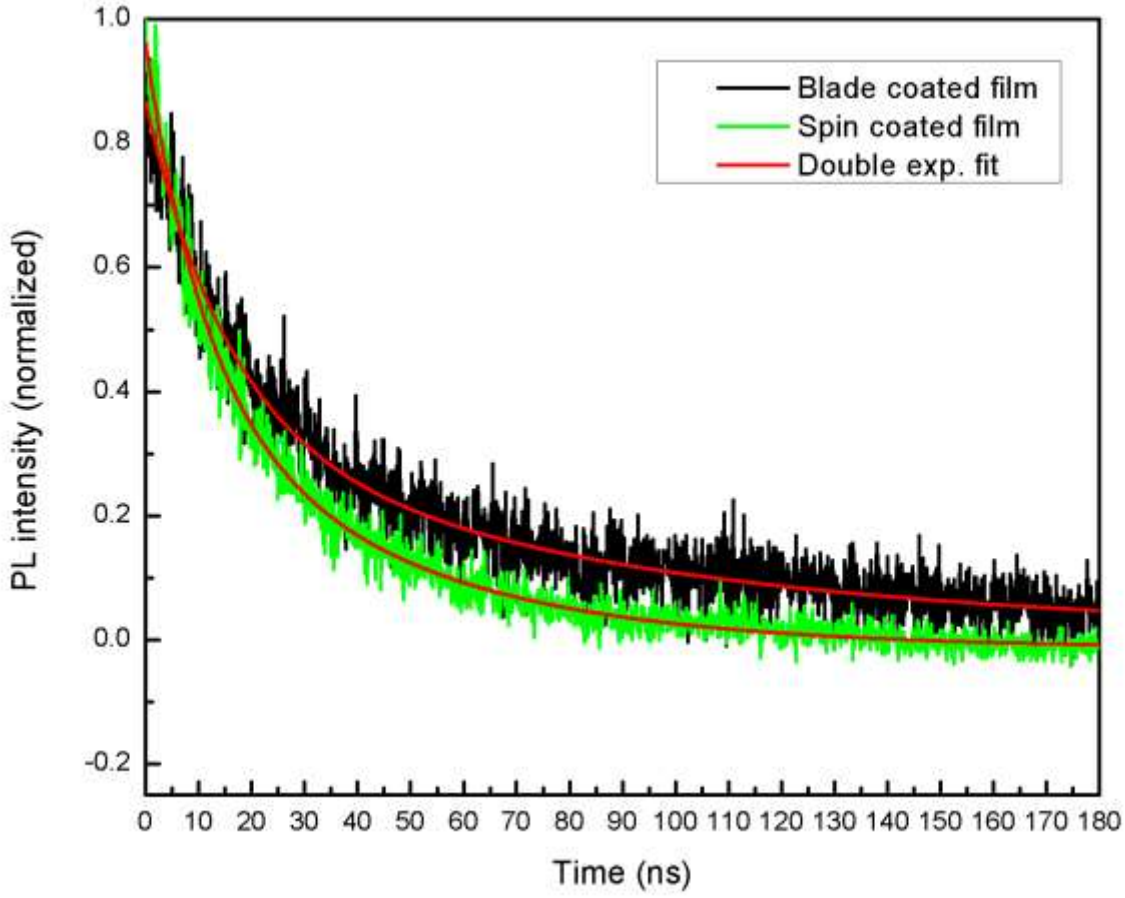

Figure 5-2 Charge carrier lifetime comparison in blade coated perovskite grain and the reference spin coated perovskite gain

5.3 Photo Resistance Measurement

The photoresistance in the various perovskite films has been investigated. To that end, lateral-structured blade-coated and spin-coated photoresistor devices on glass substrates were fabricated, with a coated spiro-OMeTAD layer as an intermediate interface between the gold electrodes and perovskite surface to reduce contact resistance. The differences

between employing a Spiro-OMeTAD layer and omitting that interfacial layer are discussed in Appendix Figure A 5-3 and also the devices resistance under different wavelength (448nm, 522nm and 700nm) of light are discussed Appendix Figure A 5-4.

As seen in the schematic illustration Figure (A & B), the channel length was 0.75 mm on the final implementation of the devices. The resistance parallel and perpendicular to the crystal grain orientation in a blade coated film was measured. To compare between the crystal grains in blade-coated and spin-coated film, measurements of resistance in the films were taken under 522 nm wavelength of light illuminations and in the dark, as presented in Figure 5-3. The different wavelengths of light, such as 448 nm, 522 nm, and 700 nm were used to illuminate the devices as depicted in Figure (C&D). The resistance in parallel (relative to shearing direction) of the blade-coated devices demonstrate lower resistance than spin-coated devices, which is three order of magnitude lower under the wavelength of 522 nm, as presented in Figure 5-4. Despite this observation, the devices obtained higher resistances under dark conditions. At wavelengths of 448 nm, the measured resistance in parallel of the sheared devices represented seven orders of magnitude lower than a spin-coated device. The resistance among the devices is showing higher photoresistance under 700 nm wavelengths of light due to less photon absorption and lower band energy of light, as presented in Appendix 3.

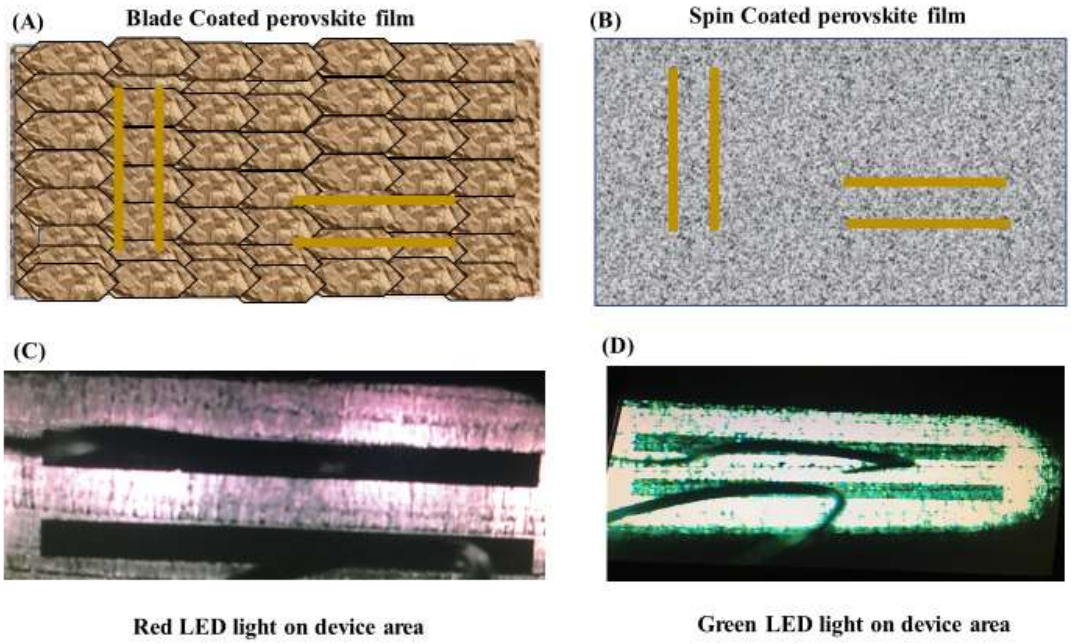

Figure 5-3 Schematic of (A) and (B) is blade coated and spin coated perovskite grain respectively and deposited gold electrode on it, (C) & (D) are red, and green LED light illuminated on the active device area

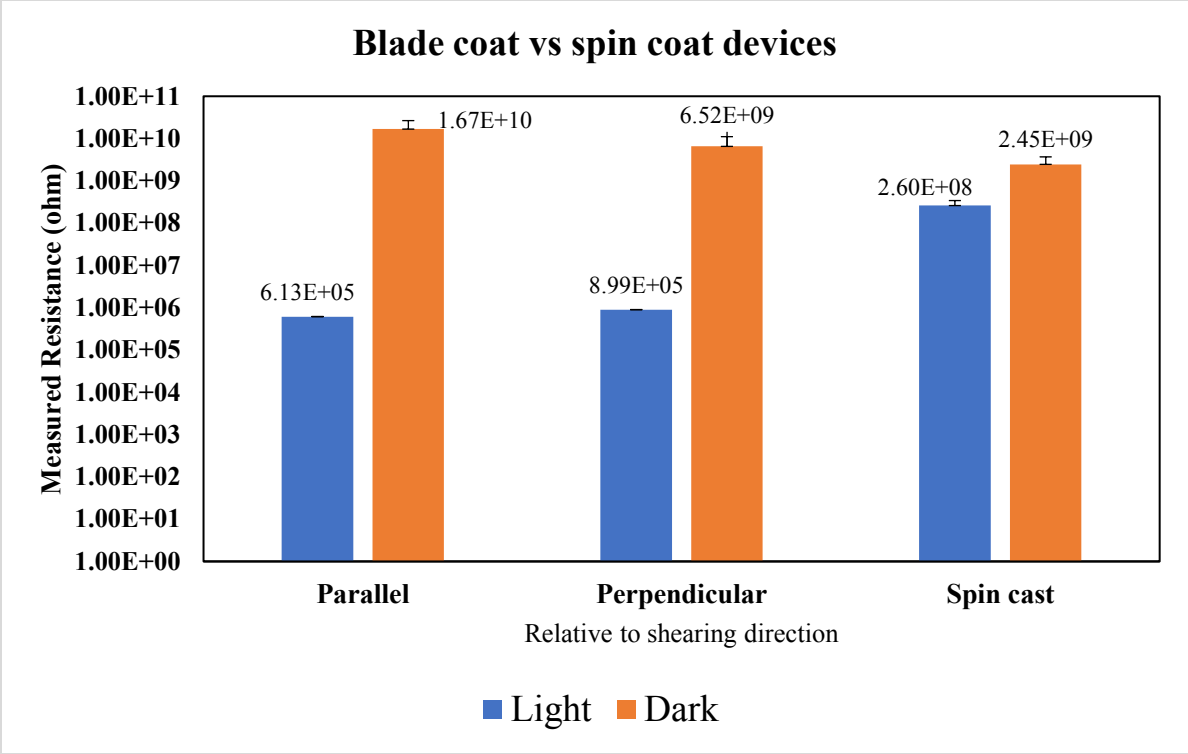

Figure 5-4 Photo-resistance comparison under illumination of 522nm light wavelength and dark of the devices

Finally, we conclude that, the photo resistance in a blade coated perovskite film is less than a spin coated perovskite film in both direction of crystal grain (parallel and perpendicular) under illumination of light.

5.4 Electrical Measurement of Perovskite Photodetector Devices

For the performance study of DMSO-based blade-coated perovskite photodetectors compared with the spin-coated devices, the spectrum of 522nm wavelength was selected as representative. A device was measured with different power densities ranging from 20 nW/cm^2 to 1 mW/cm^2. The study covered the photoresponse of the photodetector, responsivity, and device performance stability. There are two keys to acknowledging the perovskite photodetector's device performance: photoresponsivity (R) and external quantum efficiency (EQE). The device was proven to have excellent stability and external quantum efficiency was calculated using a equation.

For these devices, photo-current response (I-V), responsivity (R), and external quantum efficiency (EQE) are the figures-of-merit to compare the performances of thin and thick blade-coated devices with the reference spin-coated devices. As presented in Figure 5-5, the I-V plot is giving a clear demonstration of comparison between sheared and spin-coated devices. The device shows a higher photo-current response at higher power density of $1mW/cm^2$. At this power density, the sheared device has achieved a photocurrent six times higher of that than the spin-coated device under a 5 V bias. A thicker (~790nm) device obtained higher photo current than a thinner (~533nm) device under 5 V biasing, with details available in Appendix Figure A 5-5. It is noted that the photocurrent response is significantly better for the blade-coated photodetector devices when compared to spin-coated perovskite devices.

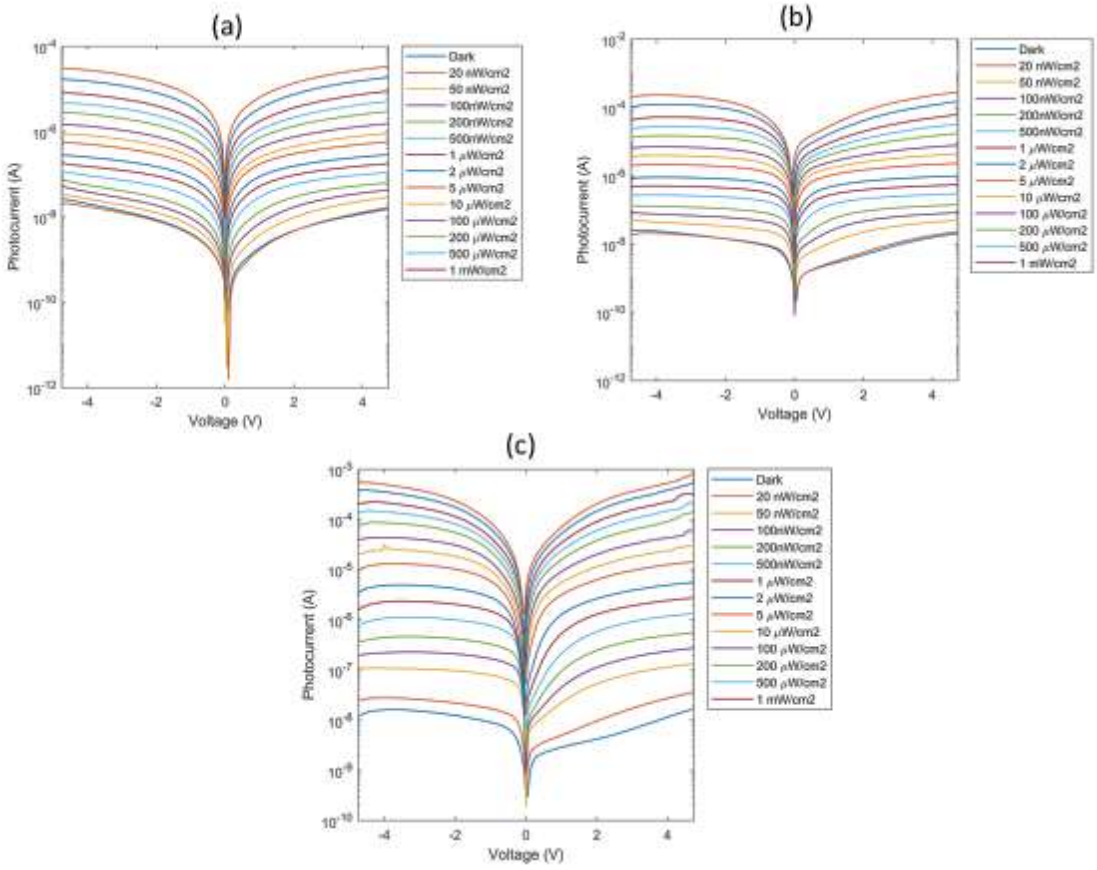

Figure 5-5 Photocurrent of photodetector devices at a different power density using 522nm wavelength of light and biased from 1V to 5V, (a) spin-coated (~550nm) device (b) blade-coated (~533nm) thin device and (c) blade-coated (~790nm) thick device

The photo-current increased linearly over an increased incident power density with the highest current (A) being obtained from 4 V biasing, as presented in Figure .

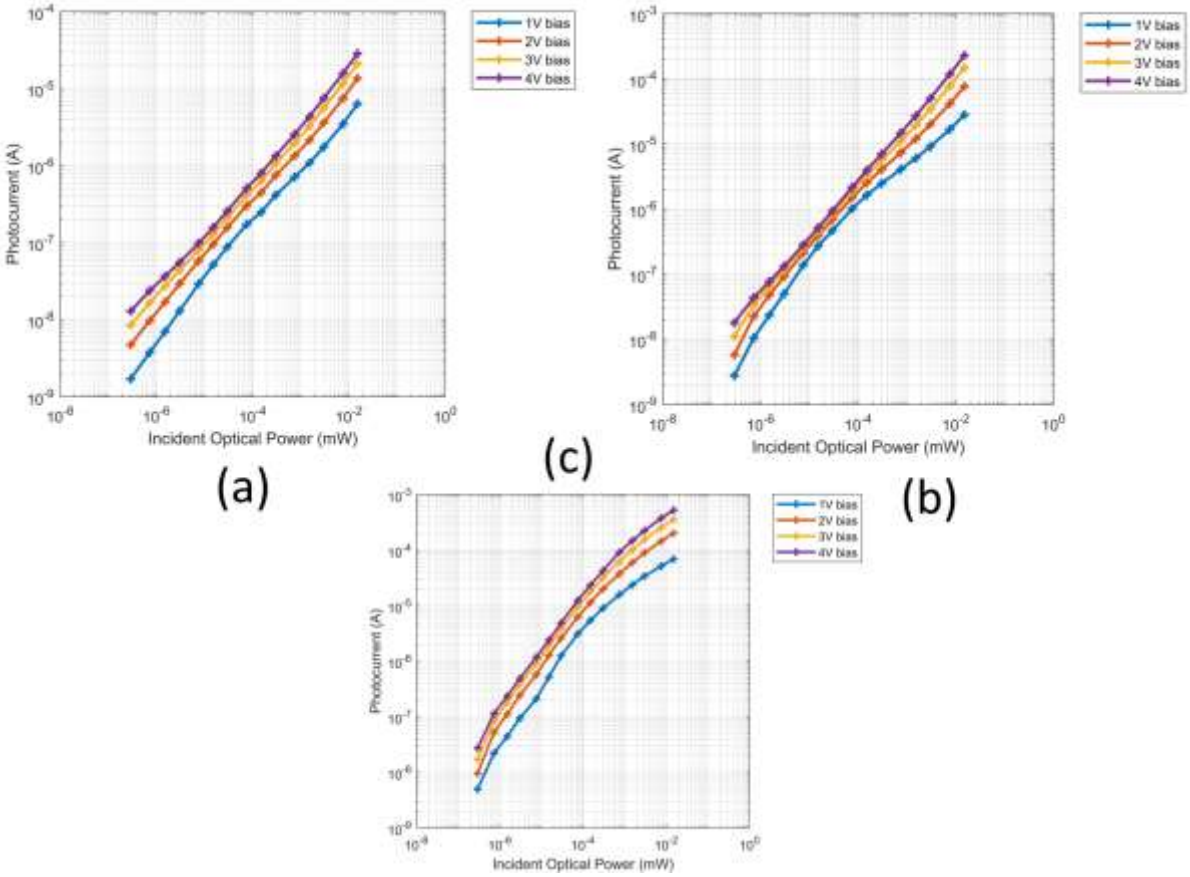

Figure 5-6 Photocurrent versus incident optical power at different voltage biasing to the devices of (a) spin-coated, (b) blade coated thin (~533nm) and (c) blade-coated thick devices (~790nm)

In this regard, spectral responsivity of both devices was calculated to compare performances in applications. The spectral responsivity can be defined by the ratio of output photocurrent and input light power density. Using an equation of responsivity (R), the responsivity of blade-coated thin devices, thick devices and spin-coated photodetectors reached to 40.26 A/W, 148.7 A/W and 16.3 A/W respectively with a low power density of

100 nW/cm^2 under 4V biasing. The responsivity decreased with increasing power density, as presented in Figure 5-7. Figure 5-8 displays the difference of responsivity for different voltage biasing for blade-coated and spin-coated devices.

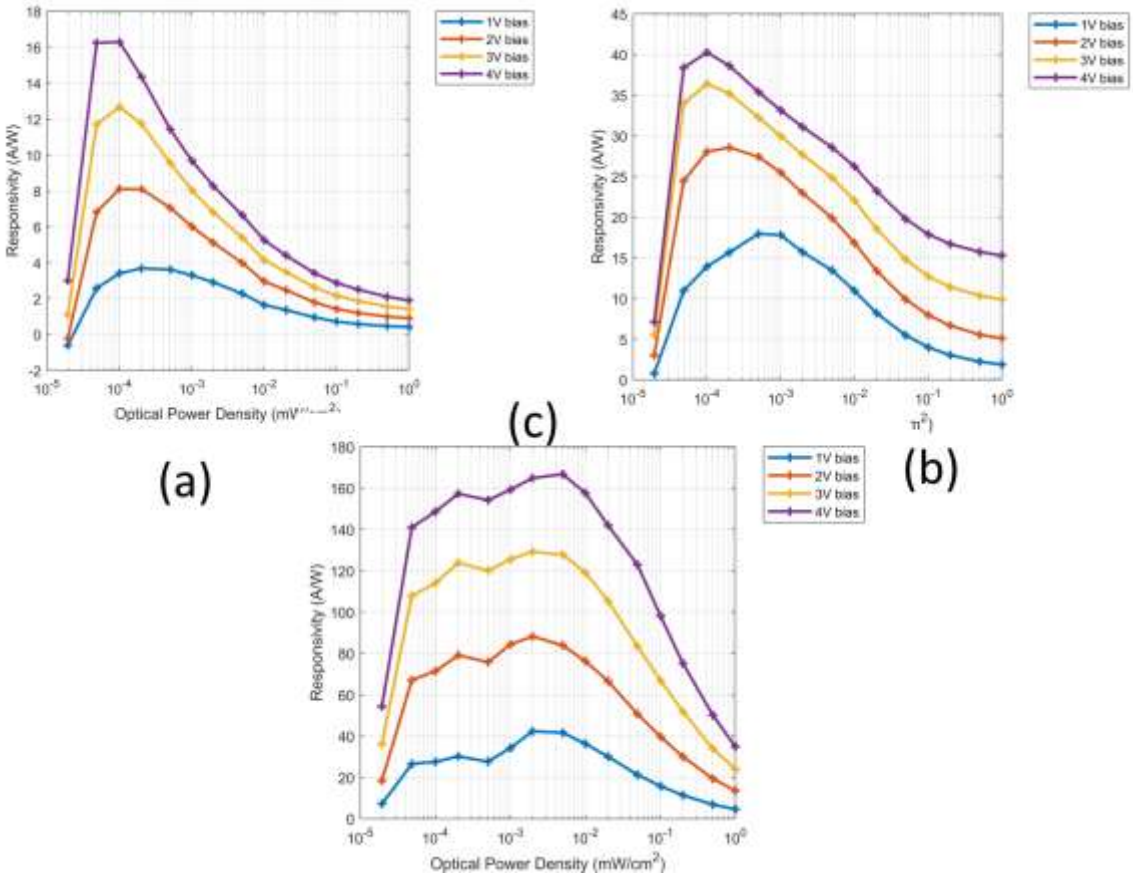

Figure 5-7 Responsivity of photodetector devices under 1 V to 4 V biasing and illuminating with power density of 20 nW/cm2 to 1 mW/cm^2 using 522 nm of light wavelength (a) spin-coated device (~550 nm), (b) blade-coated thin (~533 nm) device and (c) blade-coated thick (~790 nm) device

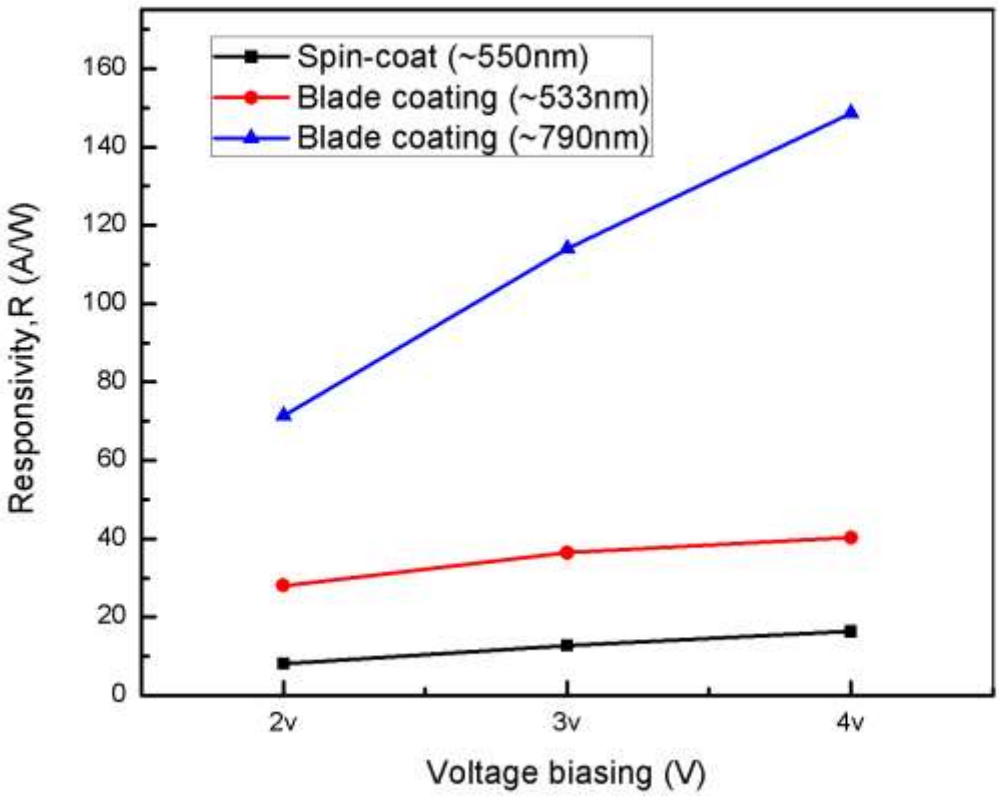

Figure 5-8 Responsivity versus biasing voltage for spin coated and blade coated devices

The maximum responsivity is reached at 148.7 A/W under 4V biasing using a 522 nm wavelength of light illumination with a low power density of 100 nW/cm^2 for a blade-coated device. The spin-coated devices reach a responsivity of 16.4 A/W under 4 V biasing where a thin blade-coated device represent the responsivity of 40.27A/W. A lateral-structured blade-coated perovskite photodetector demonstrates higher responsivity than the spin-coated device under 4V bias, as presented in Appendix Table A 5-1, which

summarizes the figure-of-merit parameters. The electrons must overcome the Schottky barrier during transport in the device. In theory, a short wavelength of 522 nm can excite more electrons and transfer to the conduction band resulting in more contribution to the photocurrent. As a result, in blade-coated devices, this phenomenon is significantly contributing to the device responsivity performance. Also, the responsivity decreased as a function of light wavelength as we can see in Figure 5-9.

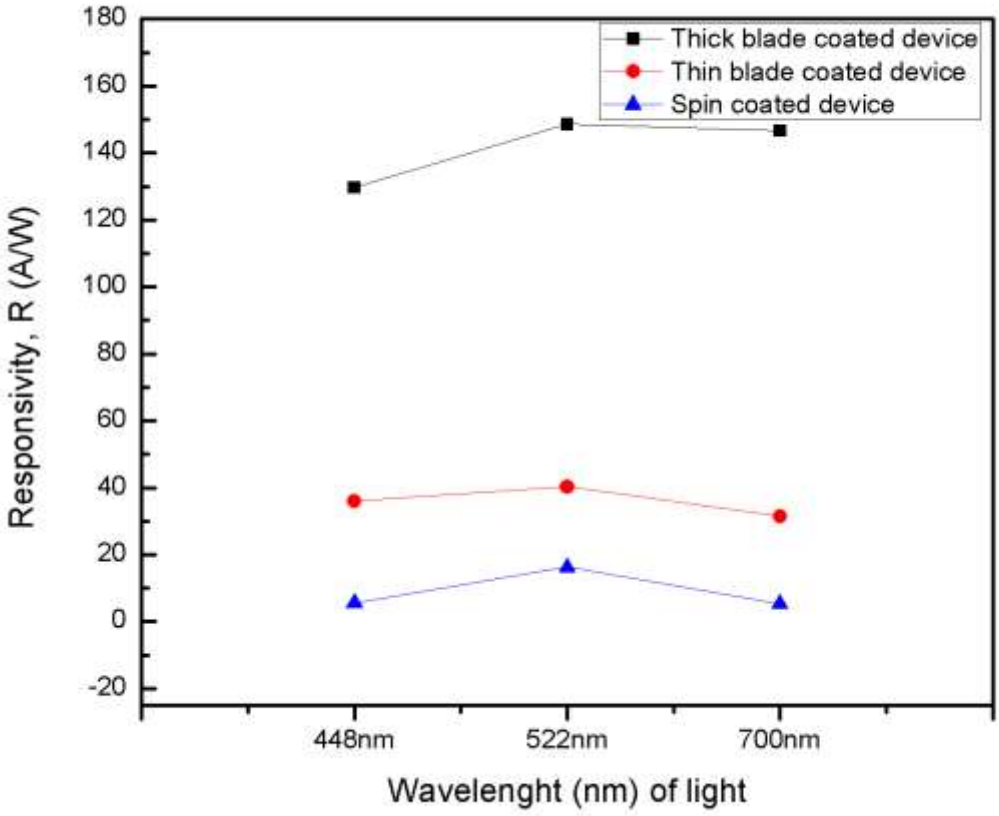

Figure 5-9 Responsivity as a function of wavelength of light

When this is applied, the external quantum efficiency was calculated using the relationship of EQE=(Rhc)/(eλ), being defined as the number of electrons detected per incident photon. The EQE of the blade-coated (~533 nm) photodetector is three times higher than that of spin-coated devices. At biasing of 4 V, a higher EQE 3.52×10^4 % is achieved from the blade-coated thicker (~790nm) devices at a lower power density of 100 nW/cm^2 where 3.89×10^3 % EQE is measured from spin-coated devices. Thicker blade coated devices have been employed with a 0.3 M concentration of precursor perovskite solution and sheared at speed of 0.125 mm/sec at a substrate temperature of 150 °C. The device was illuminated of a wavelength of 522 nm which is significantly greater than the reference spin-coated device (16.3 A/W). We measured our thicker (0.4M and 0.125mm/sec) blade coated device under 700nm wavelength of light illumination at power density of 100nW/cm2 and represents larger responsivity, R as presented in Appendix 3's Figure A 5-6. The EQE of this thinner device reaches a value of 9.6×10^3 %. Due to having more grain boundaries and a shorter carrier life time in spin-coated perovskite film, limitations were in the external quantum efficiency (EQE%) and stability performance of these films.

In the end, the work completed for this thesis was compared with other published research work, with details presented in Table 5-1.

Device architecture	Growth method	Perovskite materials and crystal structure	Responsivity R (A W−1) and light wavelength	EQE (%)	Bias and power density	Ref.
Lateral Structure	Blade-coating	$CH_3NH_3PbI_3$	40.27 and 522nm	9.6×10^3	4V and 100nW/cm^2	This work
Lateral Structure	Blade-coating	$CH_3NH_3PbI_3$	148.7 and 522nm	3.52×10^4	4V and 100nW/cm^2	This work

Lateral Structure	Blade-coating	$CH_3NH_3PbI_3$	208.7 and 700nm	4.96×10^4	4V and 100nW/cm^2	This work
Lateral Structure	Spin-coating	$CH_3NH_3PbI_3$	16.3 and 522nm	3.89×10^3	4V and 100nW/cm^2	This work (reference)
Lateral Structure	solution dropping	$CH_3NH_3PbI_3$ NW	1.32 and UV-NIF	-	1V and 80uW/cm^2	[56]
Lateral Structure	Blade-coating	Single-crystal $CH_3NH_3PbI_3$ NW	1 3.5 and 420nm	-	-5V and 1 uW/ cm^2	[60]
Lateral Structure	Two-step spin coating	$CH_3NH_3PbI_3$ CM size	3.49 and 365nm	1.19×10^3	3V and 1mW/ cm^2	[9]
Lateral Structure	Two-step of spin coating and dipping	$CH_3NH_3PbI_3$ NW	0.1 and 650nm	-	10V and 100uW/cm^2	[8]
Lateral Structure	Spin-coating	$CH_3NH_3PbI_3$	20.7 and 520nm	-	5v and 2uW/cm^2	[70]
Lateral Structure	Spin-coating	$CH_3NH_3PbI_3$ polycrystalline	0.0107 and 365nm	-	1V and 500uW/cm^2	[71]
Lateral Structure	Spin-coating	$CH_3NH_3PbI_3$ thin film	0.055 and 475nm	-	10V and 2mW/cm^2	[72]
Lateral Structure	Slip coating	$CH_3NH_3PbI_3$ NW	0.005 and 633nm	0.357	1V and 2.5W/cm^2	[73]

Table 5-1 Optoelectronic performance of thin film and single crystalline perovskite-based photodetectors

5.5 Photodetector Devices Stability

A common problem of lead halide based perovskite optoelectronics devices is instability in devices such as solar cells, photodetectors, thin film transistors, and photodetectors when exposed to the air, reducing performance. The blade-coating technique without any additive in perovskite materials significantly enhanced the stability of the tested

photodetector devices. The devices were made and stored in a glovebox in a dark environment and examined. The devices were taken out from the glovebox to characterize their properties at different time frames in air. The blade-coated photodetector devices were compared with a reference spin-coated device, as presented in Figure 5-10. The thicker blade-coated devices showed higher stability than the spin-coated device. After a week, the measurements of the spin-coated devices degraded by about 80%, while a blade-coated device degraded only 10% from its initial measurement. Two weeks later, the blade-coated devices were measured again in the air. The photocurrent through the devices was nearly unchanged in the blade-coated thicker device, which confirmed its improved stability. The measurement taken two weeks after the initial storage stood at about 82% percent of the initial value for a thicker blade-coated device, while the thinner device stood at about 52%. The spin-coated device recorded a degradation to about 14.48% after two weeks.

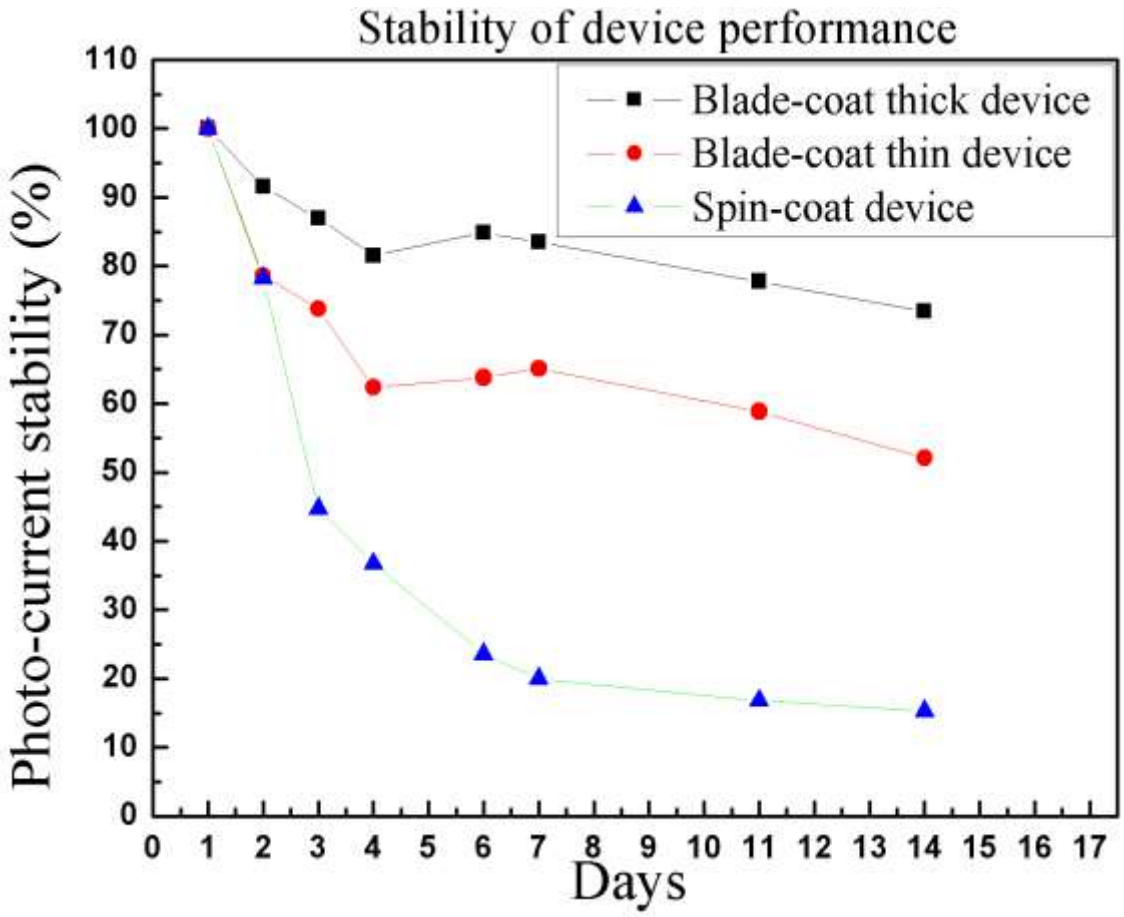

Figure 5-10 Photo-current degradation percentage of photodetector devices at different storage time

5.6 Summary

This chapter explained that the blade-coated perovskite photodetector device responsivity is significantly higher than the spin coated photodetector device. The charge carrier life times in a blade-coated device were recorded to be almost double of spin-coated device. Thicker blade coated films have better photo responses than thinner films. The improved

stability of the blade-coated devices, compared to spin-coated devices, was also shown, where the degradation of the thicker blade-coated devices was only 20% after two weeks of storage.

Chapter 6 Conclusion and Future Work

Methylammonium lead iodide perovskite materials are being widely implemented for solution based optoelectronic device fabrication. Perovskite materials based on metal halide are employed for their maximum performance and demonstrated long-term electrical stability in open air. It is currently possible to reach the maximum electrical efficiency using these devices, but long-term stability has not been attained. It was found in literature that $CH_3NH_3PbI_3$ perovskite-based photodetector devices and other applications are achieving high electrical performance at the lab scale. In this thesis, a $CH_3NH_3PbI_3$ perovskite photodetector was introduced. The morphological, optical and electrical properties were characterized for both blade-coated and spin-coated perovskite films. Perovskite photodetectors were fabricated with an active area of 0.015 cm^2. The electrical performance such as PL, PL decay, TRPL, photo resistivity in perovskite film, photo-current responses (I-V), and photo-responsivity (R) of the blade-coated photodetector in comparison to the spin-coated perovskite photodetector have been investigated. The highest achievable photo-current (mA) reported in this thesis is in the order of 15.31 mA/cm^2 for blade-coated (~533nm) photodetector devices and 1.928 mA/cm^2 for the spin-coated devices under a 4 V bias. On the other hand, a photo-current of 34.98 mA/cm^2 was achieved under illuminated at 1mW intensity from a thicker (~790nm) blade-coated photodetector which is still larger than its spin-coated counterpart.

After the optimization of the fabrication conditions, the optimal substrate temperature of 150 °C was found for the crystallized layer to be considered very stable. The optimal shearing speed was found to be 0.125 mm/sec and 0.15mm/sec for thick and thin devices respectively. In the end, a responsivity of 148.7 A/W was achieved under a 4V bias from the blade-coated thick photodetector and a responsivity of 16.3 A/W was obtained from the spin-coated perovskite photodetector device under the same bias. The blade-coated photodetector device's performance was observed to be higher than those of the spin-coated devices. The thicker blade-coated photodetector devices also exhibited a better responsivity of 208.7 A/W under a wavelength of 700nm which is higher than that of a spin-coated device under 4 V bias. The blade-coated method enhanced performance of the photo-current response with responsivity values observed to be better than the conventional spin-coating of photodetector devices. The results indicated that the technique of blade coating can be promising for optoelectronic devices. The external quantum efficiency stayed at 3.52×10^4 % at 522nm under 4V biasing which is higher than spin-coated devices. The spin-coated devices demonstrated a value of 3.89×10^3 %, which is three times lower than thicker sheared devices. The maximum responsivity achieved from lower power density has been observed to be 100 nW/cm^2.

Experimental results from the devices at 3V and 4V biasing were presented and thoroughly analyzed in Chapter 5. The electrical stability was presented for the blade-coating perovskite photodetectors for thicknesses of both ~533nm and ~790nm of the perovskite layer in order to provide the readers with a better understanding of the effect of thickness on the material's behavior. The reference spin-coated device also was measured for

electrical stability to compare with blade-coated devices. Electrically, a blade-coated thicker device had about 80% higher stability than a spin-coated device in air.

The next challenge is device stability enhancement in air, performance enhancement, environmental-friendly perovskite materials, and nano-systems with multifunction as shown in the flow chart below. There will also be a competition for organic-inorganic based optoelectronic devices against more mature competing technology.

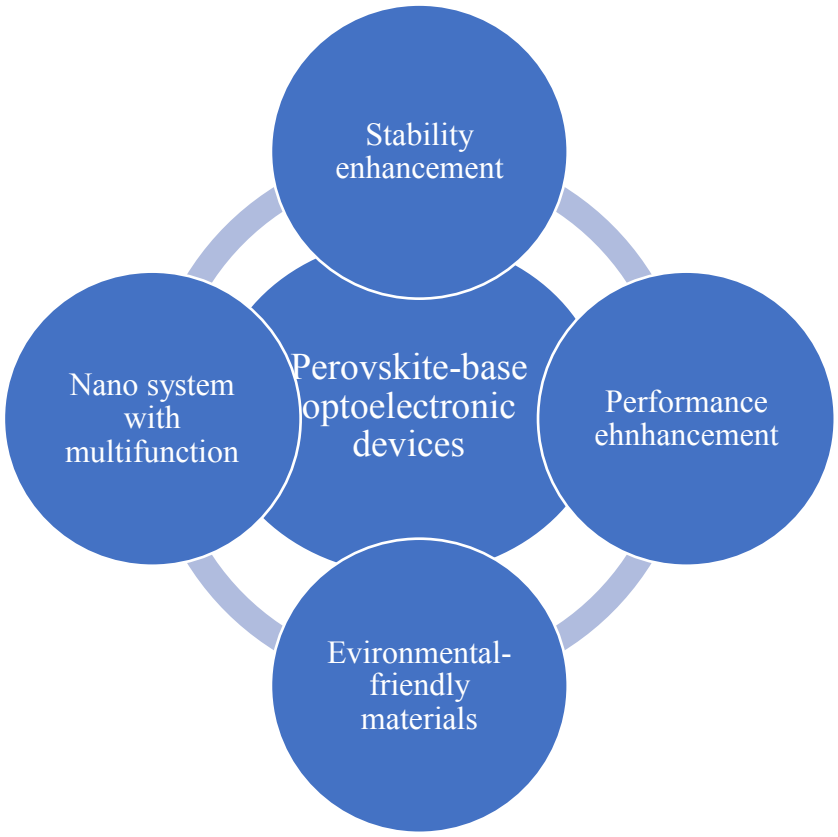

Figure 6-1 Flow chart of future challenging work for perovskite based optoelectronic devices

Future research will involve making efficient and stable perovskite photodetectors with different solvent-based perovskite solutions in an attempt to enhance the surface morphology and the interface between the layers. A new precursor solvent will be used in the perovskite solution process to control the surface morphology and create a larger single crystal domain. The encapsulation method, humidity control, use of fewer toxic halide materials, prevention of solvent corrosion, and compositional tunability may also make the optoelectronic devices stable in air. The blade-coating technique or another fabrication technique would be used to create a single crystal grain in the perovskite absorber layer to absorb more photons to make electrical energy.

This work has provided essential guidance for material optimization of crystalline morphology and the future development of novel optoelectronic devices.

References

[1] C. Wu *et al.*, "Near-unity below-band-gap absorption by microstructured silicon," *Appl. Phys. Lett.*, vol. 78, no. 13, pp. 1850–1852, Mar. 2001.

[2] R. A. Myers, R. Farrell, A. M. Karger, J. E. Carey, and E. Mazur, "Enhancing near-infrared avalanche photodiode performance by femtosecond laser microstructuring," *Appl. Opt.*, vol. 45, no. 35, p. 8825, Dec. 2006.

[3] M. Mikulics *et al.*, "Ultrafast metal-semiconductor-metal photodetectors on low-temperature-grown GaN," 2005.

[4] K. J. Chen, F. Y. Hung, S. J. Chang, and S. J. Young, "Optoelectronic characteristics of UV photodetector based on ZnO nanowire thin films," *J. Alloys Compd.*, vol. 479, no. 1–2, pp. 674–677, Jun. 2009.

[5] Z. Wang, M. Safdar, C. Jiang, and J. He, "High-Performance UV–Visible–NIR Broad Spectral Photodetectors Based on One-Dimensional In_2Te_3 Nanostructures," *Nano Lett.*, vol. 12, no. 9, pp. 4715–4721, Sep. 2012.

[6] R. X. Wang *et al.*, "The effect of Ga-doped nanocrystalline ZnO electrode on deep-ultraviolet enhanced GaN photodetector," *Appl. Phys. Lett.*, vol. 102, no. 21, p. 212104, May 2013.

[7] X. Gao, Y. Cui, R. M. Levenson, L. W. K. Chung, and S. Nie, "In vivo cancer targeting and imaging with semiconductor quantum dots," *Nat. Biotechnol.*, vol. 22, no. 8, pp. 969–976, Aug. 2004.

[8] H. Deng *et al.*, "Flexible and semitransparent organolead triiodide perovskite network photodetector arrays with high stability," *Nano Lett.*, 2015.

[9] Z. Lian *et al.*, "High-Performance Planar-Type Photodetector on (100) Facet of MAPbI3Single Crystal," *Sci. Rep.*, 2015.

[10] M. I. Saidaminov *et al.*, "Perovskite Photodetectors Operating in Both Narrowband and Broadband Regimes," *Adv. Mater.*, 2016.

[11] N. Cho *et al.*, "Pure crystal orientation and anisotropic charge transport in large-area hybrid perovskite films," *Nat. Commun.*, 2016.

[12] Y. Dong *et al.*, "Improving All-Inorganic Perovskite Photodetectors by Preferred Orientation and Plasmonic Effect," *Small*, vol. 12, no. 40, pp. 5622–5632, Oct. 2016.

[13] P. Ramasamy, D. H. Lim, B. Kim, S. H. Lee, M. S. Lee, and J. S. Lee, "All-inorganic cesium lead halide perovskite nanocrystals for photodetector applications," *Chem. Commun.*, 2016.

[14] W. Deng *et al.*, "Aligned Single-Crystalline Perovskite Microwire Arrays for High-Performance Flexible Image Sensors with Long-Term Stability," *Adv. Mater.*, 2016.

[15] Y. Kim *et al.*, "Efficient Luminescence from Perovskite Quantum Dot Solids," *ACS Appl. Mater. Interfaces*, vol. 7, no. 45, pp. 25007–25013, Nov. 2015.

[16] Q. Chen *et al.*, "Planar Heterojunction Perovskite Solar Cells via Vapor-Assisted Solution Process," *J. Am. Chem. Soc.*, vol. 136, no. 2, pp. 622–625, Jan. 2014.

[17] M. Liu, M. B. Johnston, and H. J. Snaith, "Efficient planar heterojunction perovskite solar cells by vapour deposition," *Nature*, vol. 501, no. 7467, pp. 395–398, Sep. 2013.

[18] J. Xue *et al.*, "Constructing Mie-Scattering Porous Interface-Fused Perovskite Films to Synergistically Boost Light Harvesting and Carrier Transport," *Angew. Chemie Int. Ed.*, vol. 56, no. 19, pp. 5232–5236, May 2017.

[19] K. K. Wong *et al.*, "Interface-Dependent Radiative and Nonradiative Recombination in Perovskite Solar Cells," *J. Phys. Chem. C*, 2018.

[20] F. Sahli *et al.*, "Fully textured monolithic perovskite/silicon tandem solar cells with 25.2% power conversion efficiency," *Nat. Mater.*, vol. 17, no. 9, pp. 820–826, Sep. 2018.

[21] S. A. Veldhuis *et al.*, "Perovskite Materials for Light-Emitting Diodes and Lasers," *Adv. Mater.*, pp. 6804–6834, 2016.

[22] G. Xing *et al.*, "Low-temperature solution-processed wavelength-tunable perovskites for lasing," *Nat. Mater.*, vol. 13, no. 5, pp. 476–480, 2014.

[23] H. Zhu *et al.*, "Lead halide perovskite nanowire lasers with low lasing thresholds and high quality factors," *Nat. Mater.*, vol. 14, no. 6, pp. 636–642, 2015.

[24] W. Deng *et al.*, "Ultrahigh-Responsivity Photodetectors from Perovskite Nanowire Arrays for Sequentially Tunable Spectral Measurement," *Nano Lett.*, vol. 17, no. 4, pp. 2482–2489, 2017.

[25] M. I. Saidaminov *et al.*, "Perovskite Photodetectors Operating in Both Narrowband and Broadband Regimes," *Adv. Mater.*, vol. 28, no. 37, pp. 8144–8149, Oct. 2016.

[26] X. Qin, Y. Yao, H. Dong, Y. Zhen, L. Jiang, and W. Hu, "Perovskite Photodetectors based on CH3NH3PbI3Single Crystals," *Chem. - An Asian J.*, vol. 11, no. 19, pp. 2675–2679, 2016.

[27] G. Wang *et al.*, "Wafer-scale growth of large arrays of perovskite microplate crystals for functional electronics and optoelectronics," *Sci. Adv.*, vol. 1, no. 9, pp. 1–9, 2015.

[28] J. Cui *et al.*, "Recent progress in efficient hybrid lead halide perovskite solar cells," *Sci. Technol. Adv. Mater.*, vol. 16, no. 3, p. 036004, Jun. 2015.

[29] B. Saparov and D. B. Mitzi, “Organic–Inorganic Perovskites: Structural Versatility for Functional Materials Design,” *Chem. Rev.*, vol. 116, no. 7, pp. 4558–4596, Apr. 2016.

[30] D. B. Mitzi, “Templating and structural engineering in organic-inorganic perovskites,” *J. Chem. Soc., Dalt. Trans*, pp. 1–12, 2001.

[31] Y. Liu, Z. Yang, and S. F. Liu, “Recent Progress in Single-Crystalline Perovskite Research Including Crystal Preparation, Property Evaluation, and Applications.,” *Adv. Sci. (Weinheim, Baden-Wurttemberg, Ger.*, vol. 5, no. 1, p. 1700471, 2018.

[32] Y. Kawamura, H. Mashiyama, and K. Hasebe, “Structural Study on Cubic–Tetragonal Transition of $CH_3NH_3PbI_3$,” *J. Phys. Soc. Japan*, vol. 71, no. 7, pp. 1694–1697, Jul. 2002.

[33] G. Xing *et al.*, “Long-Range Balanced Electron- and Hole-Transport Lengths in Organic-Inorganic CH3NH3PbI3,” *Science (80-.).*, vol. 342, no. 6156, pp. 344–347, Oct. 2013.

[34] J. H. Heo *et al.*, “Efficient inorganic–organic hybrid heterojunction solar cells containing perovskite compound and polymeric hole conductors,” *Nat. Photonics*, vol. 7, no. 6, pp. 486–491, Jun. 2013.

[35] C. Wehrenfennig, G. E. Eperon, M. B. Johnston, H. J. Snaith, and L. M. Herz, “High Charge Carrier Mobilities and Lifetimes in Organolead Trihalide Perovskites,” *Adv. Mater.*, vol. 26, no. 10, pp. 1584–1589, Mar. 2014.

[36] E. J. Juarez-Perez *et al.*, “Photoinduced Giant Dielectric Constant in Lead Halide Perovskite Solar Cells,” *J. Phys. Chem. Lett.*, vol. 5, no. 13, pp. 2390–2394, Jul. 2014.

[37] V. D'Innocenzo *et al.*, "Excitons versus free charges in organo-lead tri-halide perovskites," *Nat. Commun.*, vol. 5, no. 1, p. 3586, Dec. 2014.

[38] J. M. Frost, K. T. Butler, F. Brivio, C. H. Hendon, M. van Schilfgaarde, and A. Walsh, "Atomistic Origins of High-Performance in Hybrid Halide Perovskite Solar Cells," *Nano Lett.*, vol. 14, no. 5, pp. 2584–2590, May 2014.

[39] K. Domanski, W. Tress, T. Moehl, M. Saliba, M. K. Nazeeruddin, and M. Grätzel, "Working Principles of Perovskite Photodetectors: Analyzing the Interplay Between Photoconductivity and Voltage-Driven Energy-Level Alignment," *Adv. Funct. Mater.*, vol. 25, no. 44, pp. 6936–6947, Nov. 2015.

[40] R. Dong *et al.*, "High-Gain and Low-Driving-Voltage Photodetectors Based on Organolead Triiodide Perovskites," *Adv. Mater.*, vol. 27, no. 11, pp. 1912–1918, Mar. 2015.

[41] X. Hu *et al.*, "High-Performance Flexible Broadband Photodetector Based on Organolead Halide Perovskite," *Adv. Funct. Mater.*, vol. 24, no. 46, pp. 7373–7380, Dec. 2014.

[42] H. Deng *et al.*, "Flexible and Semitransparent Organolead Triiodide Perovskite Network Photodetector Arrays with High Stability," *Nano Lett.*, vol. 15, no. 12, pp. 7963–7969, Dec. 2015.

[43] Z. Lian *et al.*, "High-Performance Planar-Type Photodetector on (100) Facet of MAPbI 3 Single Crystal," *Sci. Rep.*, vol. 5, no. 1, p. 16563, Dec. 2015.

[44] J. Ding *et al.*, "From chip-in-a-lab to lab-on-a-chip: towards a single handheld electronic system for multiple application-specific lab-on-a-chip (ASLOC)," vol. 18, p. 4405, 2014.

[45] P. Ramasamy, D.-H. Lim, B. Kim, S.-H. Lee, M.-S. Lee, and J.-S. Lee, "All-inorganic cesium lead halide perovskite nanocrystals for photodetector applications," *Chem. Commun.*, vol. 52, no. 10, pp. 2067–2070, Jan. 2016.

[46] V. Adinolfi *et al.*, "Fast and Sensitive Solution-Processed Visible-Blind Perovskite UV Photodetectors," *Adv. Mater.*, vol. 28, no. 33, pp. 7264–7268, Sep. 2016.

[47] W. Wang *et al.*, "Visible blind ultraviolet photodetector based on CH_3NH_3PbCl_3 thin film," *Opt. Express*, vol. 24, no. 8, p. 8411, Apr. 2016.

[48] L. Etgar *et al.*, "Mesoscopic CH 3 NH 3 PbI 3 /TiO 2 Heterojunction Solar Cells," *J. Am. Chem. Soc*, vol. 134, pp. 17396–17399, 2012.

[49] D. Bi *et al.*, "18762 RSC Advances COMMUNICATION 18762 | RSC Adv," *This J. is ß R. Soc. Chem.*, vol. 3, no. 3, pp. 18762–18766, 2013.

[50] G. Wang *et al.*, "Efficient perovskite solar cell fabricated in ambient air using one-step spin-coating," *RSC Adv.*, vol. 6, no. 49, pp. 43299–43303, Apr. 2016.

[51] J. Burschka *et al.*, "Sequential deposition as a route to high-performance perovskite-sensitized solar cells," *Nature*, vol. 499, no. 7458, pp. 316–319, Jul. 2013.

[52] T. C. Sum and N. Mathews, "Advancements in perovskite solar cells: photophysics behind the photovoltaics," *Energy Environ. Sci.*, vol. 7, no. 8, pp. 2518–2534, Jul. 2014.

[53] Y. Wang *et al.*, "Vapour-assisted multi-functional perovskite thin films for solar cells and photodetectors," *J. Mater. Chem. C*, vol. 4, no. 31, pp. 7415–7419, Aug. 2016.

[54] S. F. Leung *et al.*, "A Self-Powered and Flexible Organometallic Halide Perovskite Photodetector with Very High Detectivity," *Adv. Mater.*, 2018.

[55] X. Hu *et al.*, "High-performance flexible broadband photodetector based on organolead halide perovskite," *Adv. Funct. Mater.*, 2014.

[56] H. Deng *et al.*, "Growth, patterning and alignment of organolead iodide perovskite nanowires for optoelectronic devices," *Nanoscale*, 2015.

[57] Q. Hu, H. Wu, J. Sun, D. Yan, Y. Gao, and J. Yang, "Large-area perovskite nanowire arrays fabricated by large-scale roll-to-roll micro-gravure printing and doctor blading," *Nanoscale*, 2016.

[58] P. Zhu *et al.*, "Direct Conversion of Perovskite Thin Films into Nanowires with Kinetic Control for Flexible Optoelectronic Devices," *Nano Lett.*, 2016.

[59] D. Shi *et al.*, "Solar cells. Low trap-state density and long carrier diffusion in organolead trihalide perovskite single crystals.," *Science*, vol. 347, no. 6221, pp. 519–22, Jan. 2015.

[60] W. Deng *et al.*, "Aligned Single-Crystalline Perovskite Microwire Arrays for High-Performance Flexible Image Sensors with Long-Term Stability," *Adv. Mater.*, vol. 28, no. 11, pp. 2201–2208, Mar. 2016.

[61] J. Y. Jeng *et al.*, "CH3NH3PbI3 perovskite/fullerene planar-heterojunction hybrid solar cells," *Adv. Mater.*, vol. 25, no. 27, pp. 3727–3732, 2013.

[62] P. Fan *et al.*, "High-performance perovskite CH3NH3PbI3 thin films for solar cells prepared by single-source physical vapour deposition," *Sci. Rep.*, vol. 6, no. 1, p. 29910, Sep. 2016.

[63] S. D. Stranks *et al.*, "Electron-hole diffusion lengths exceeding 1 micrometer in an organometal trihalide perovskite absorber.," *Science*, vol. 342, no. 6156, pp. 341–4, Oct. 2013.

[64] C. C. Stoumpos, C. D. Malliakas, and M. G. Kanatzidis, “Semiconducting Tin and Lead Iodide Perovskites with Organic Cations: Phase Transitions, High Mobilities, and Near-Infrared Photoluminescent Properties,” 2013.

[65] J. L. Barnett, V. L. Cherrette, C. J. Hutcherson, and M. C. So, “Effects of Solution-Based Fabrication Conditions on Morphology of Lead Halide Perovskite Thin Film Solar Cells,” *Advances in Materials Science and Engineering*. 2016.

[66] M. He *et al.*, “Meniscus-assisted solution printing of large-grained perovskite films for high-efficiency solar cells,” *Nat. Commun.*, 2017.

[67] L. Gao *et al.*, “Passivated Single-Crystalline CH 3 NH 3 PbI 3 Nanowire Photodetector with High Detectivity and Polarization Sensitivity,” *Nano Lett*, vol. 16, p. 25, 2016.

[68] R. G. Stearns and R. L. Weisfield, “Two-dimensional amorphous-silicon photodetector array for optical imaging.”

[69] L. Li *et al.*, “Electrical transport and high-Performance photoconductivity in individual ZrS2nanobelts,” *Adv. Mater.*, 2010.

[70] L. Ji, H. Y. Hsu, J. C. Lee, A. J. Bard, and E. T. Yu, “High-Performance Photodetectors Based on Solution-Processed Epitaxial Grown Hybrid Halide Perovskites,” *Nano Lett.*, 2018.

[71] S. Chen, C. Teng, M. Zhang, Y. Li, D. Xie, and G. Shi, “A Flexible UV–Vis–NIR Photodetector based on a Perovskite/Conjugated-Polymer Composite,” *Adv. Mater.*, 2016.

[72] F. Wang, J. Mei, Y. Wang, L. Zhang, H. Zhao, and D. Zhao, “Fast Photoconductive Responses in Organometal Halide Perovskite Photodetectors,” *ACS Appl. Mater. Interfaces*, 2016.

[73] E. Horváth *et al.*, “Nanowires of Methylammonium Lead Iodide (CH3NH3PbI3) prepared by low temperature solution-mediated crystallization,” *Nano Lett.*, 2014.

Appendices

Appendix 1

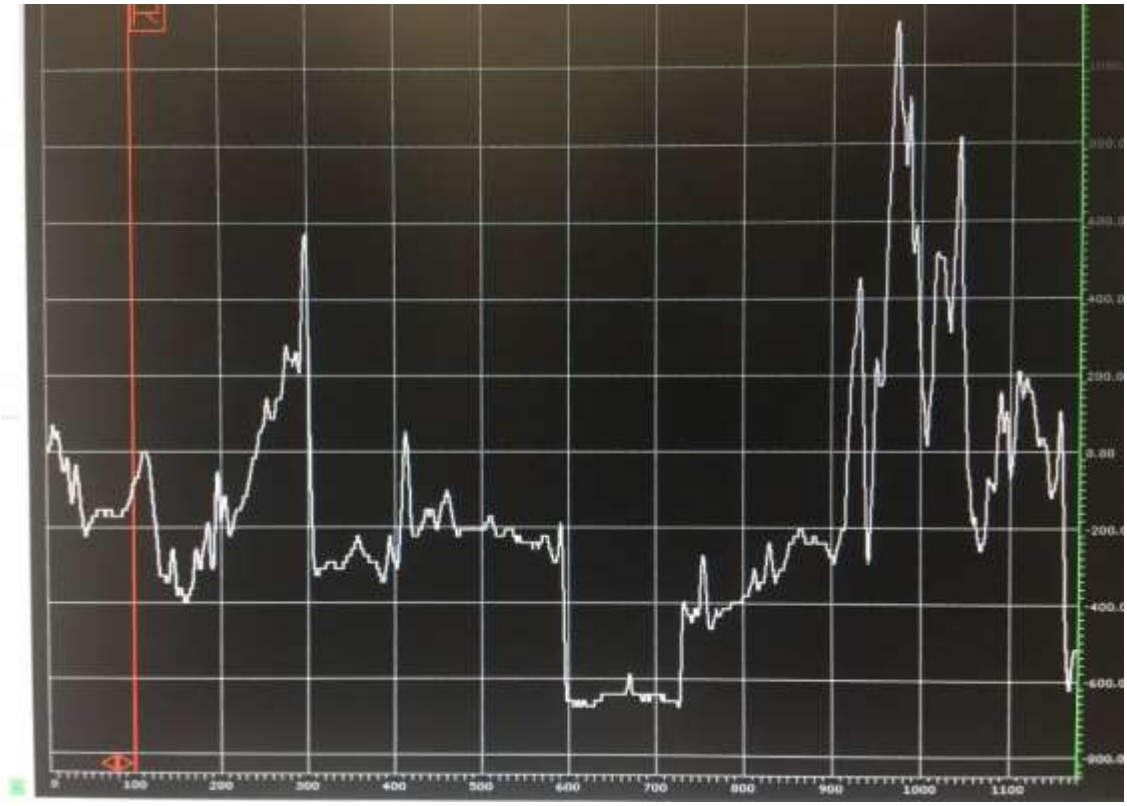

Appendix Figure A 3-1 Photograph of perovskite film thickness measurement using profilometry spectra

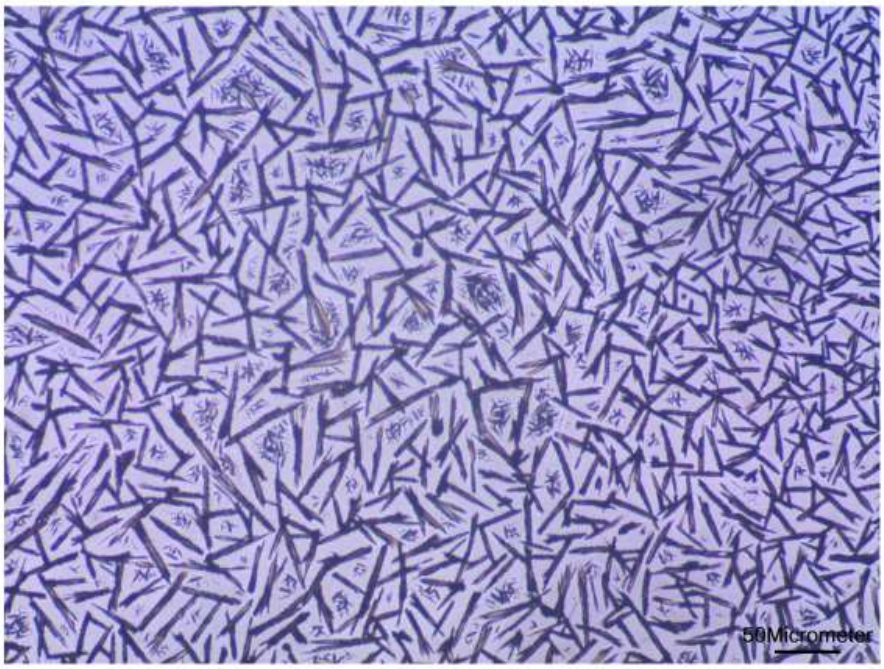

Appendix Figure A 3-2 OM image of DMSO based spin coated perovskite film

A spin-coated and blade-coated perovskite films were viewed with a scanning electron microscope (SEM) in micrometer scale, as presented in Appendix Figure A 3-2 and 3-3. A crystal grain is formed in parallel with the substrate in blade-coated sheared film. On the other hand, the crystal grain is formed in perpendicular with the substrate in spin-coated perovskite.

Spin coated perovskite crystal structure

Solution sheared perovskite crystal structure

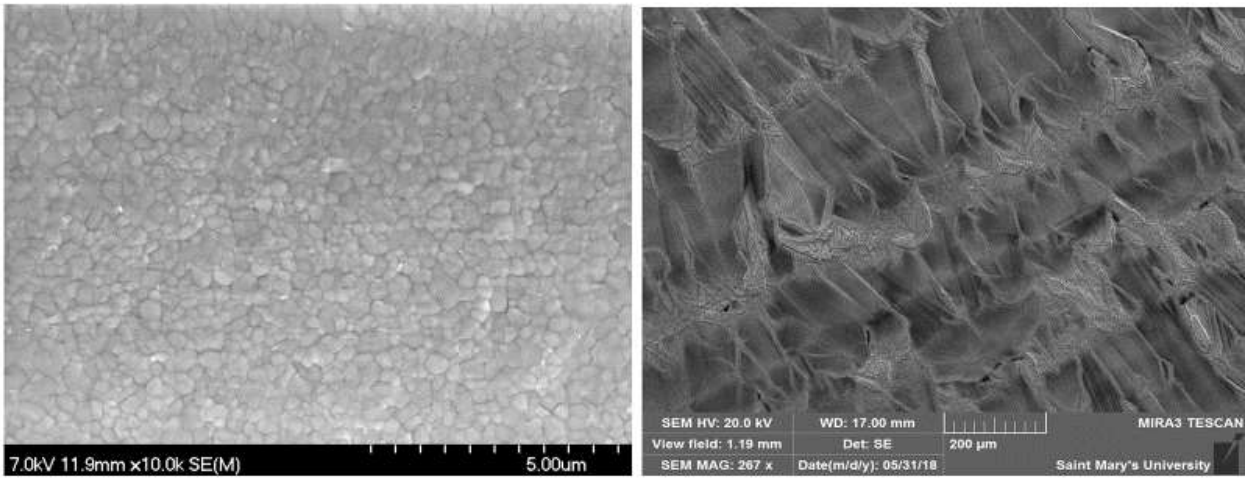

Appendix Figure A 3-2 Comparison between blade-coated (right) and spin-coated (left) perovskite single crystal structure

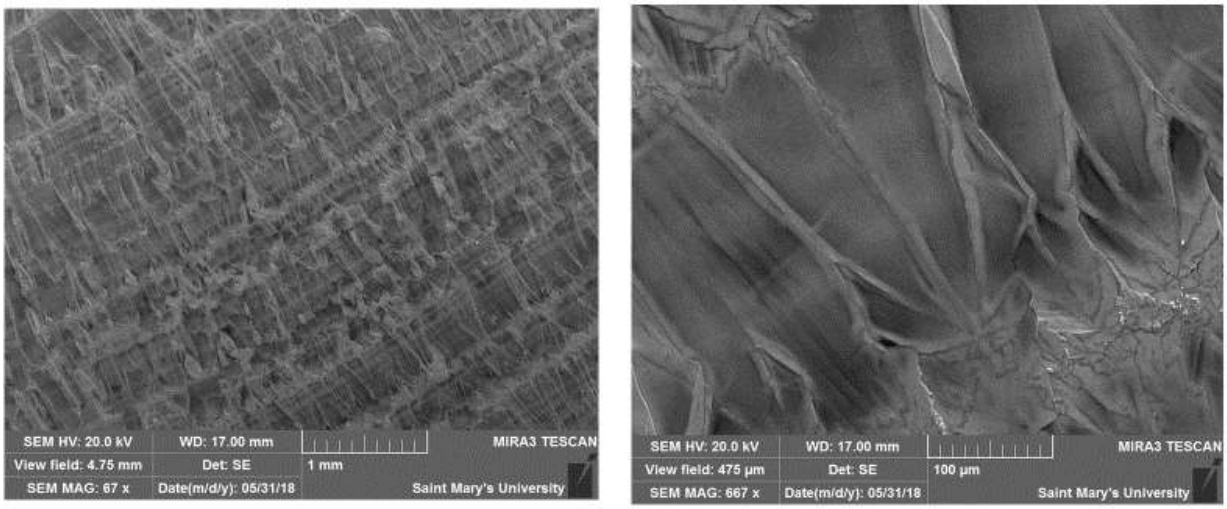

Appendix Figure A 3-3 SEM images of blade-coated perovskite film at different magnification

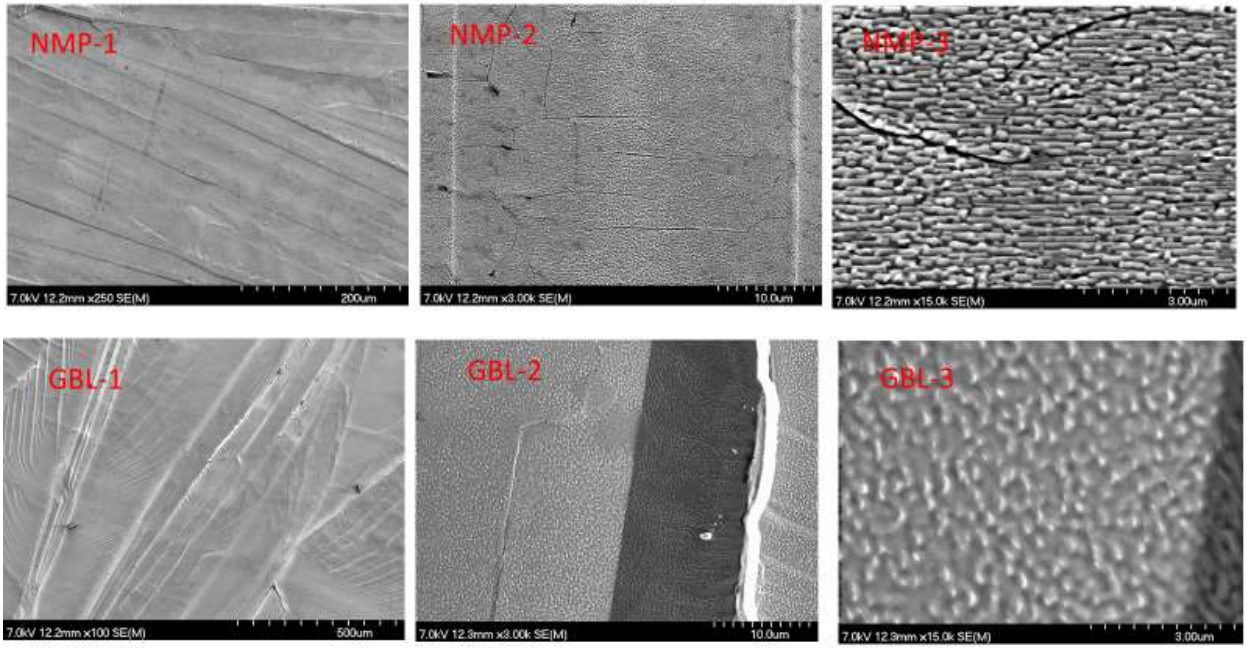

Appendix Figure A 3-4 SEM images of GBL and NMP based crystallized perovskite film at a different scale.

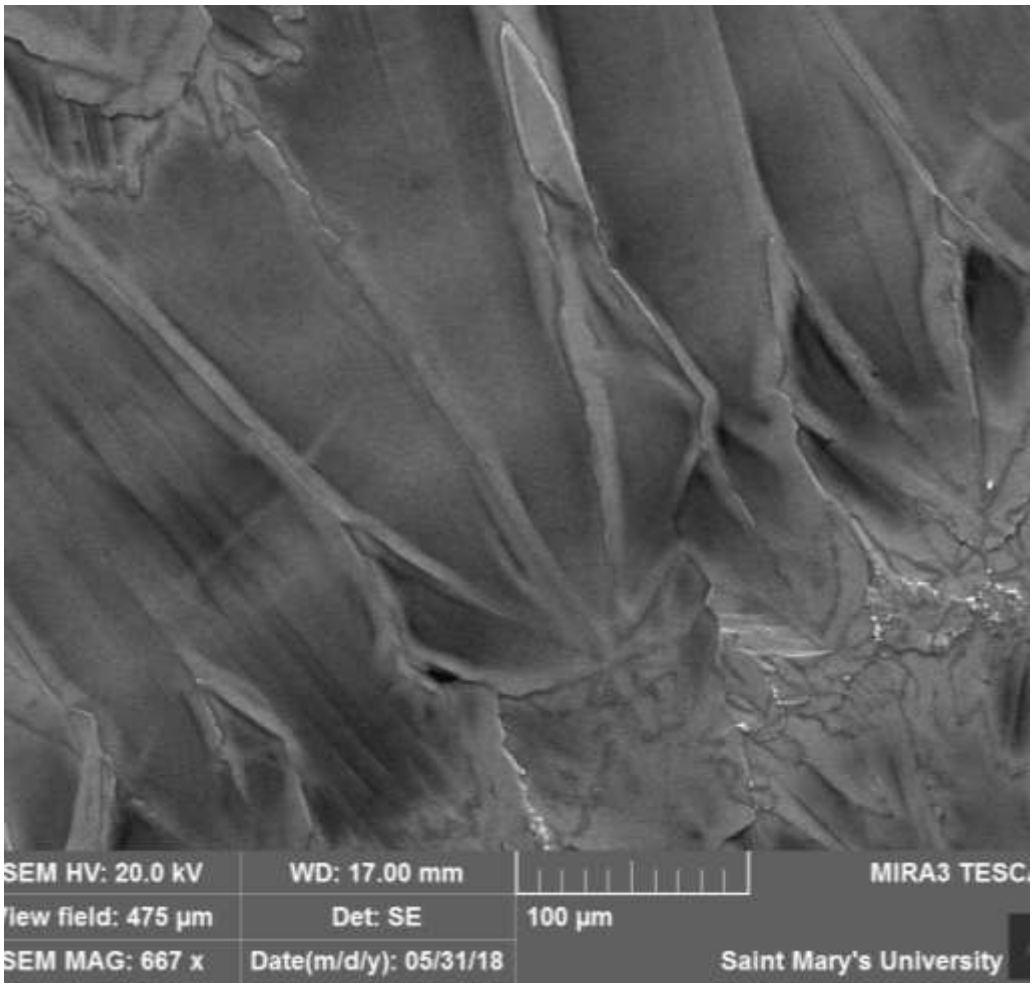

Appendix Figure A 3-5 Scanning electron microscopic (SEM) image of blade-coated perovskite film is showing larger crystal grain and their boundaries

The XRD of DMSO based perovskite film is compared with NMP based perovskite film and its shows the crystal peak at same position of 2 theta angle.

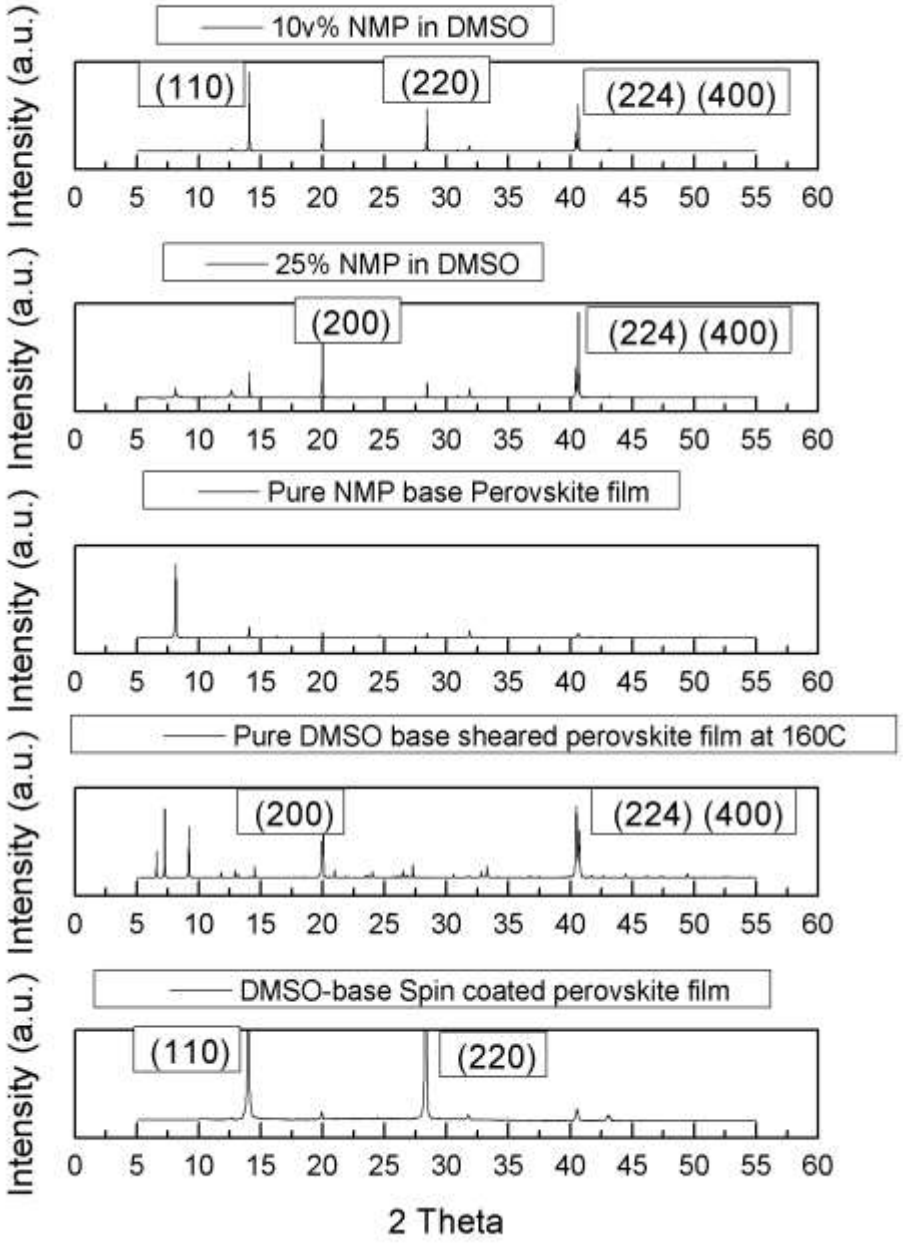

Appendix Figure A 3-6 Comparison of XRD diffraction in between NMP and DMSO base perovskite film

In a time-frame, a blade-coated perovskite film is characterized by XRD technique.

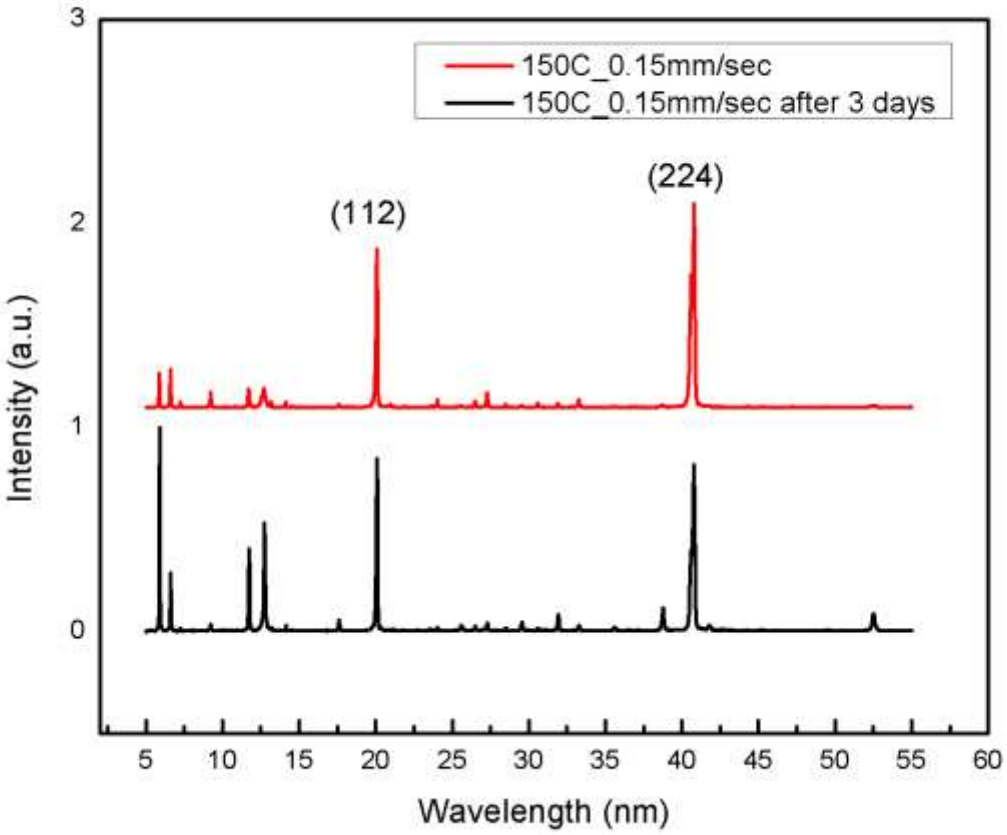

Appendix Figure A 3-7 X-ray diffraction profile of blade-coated $CH_3NH_3PbI_3$ (150 ^{o} C and 0.15mm/sec) perovskite film at different days

A breaking line is made in perpendicular of solution shearing direction during blade coating. The perovskite film was viewed with higher magnification of optical microscopy. It seems the crystal structure are continuous, and no pinholes in those areas.

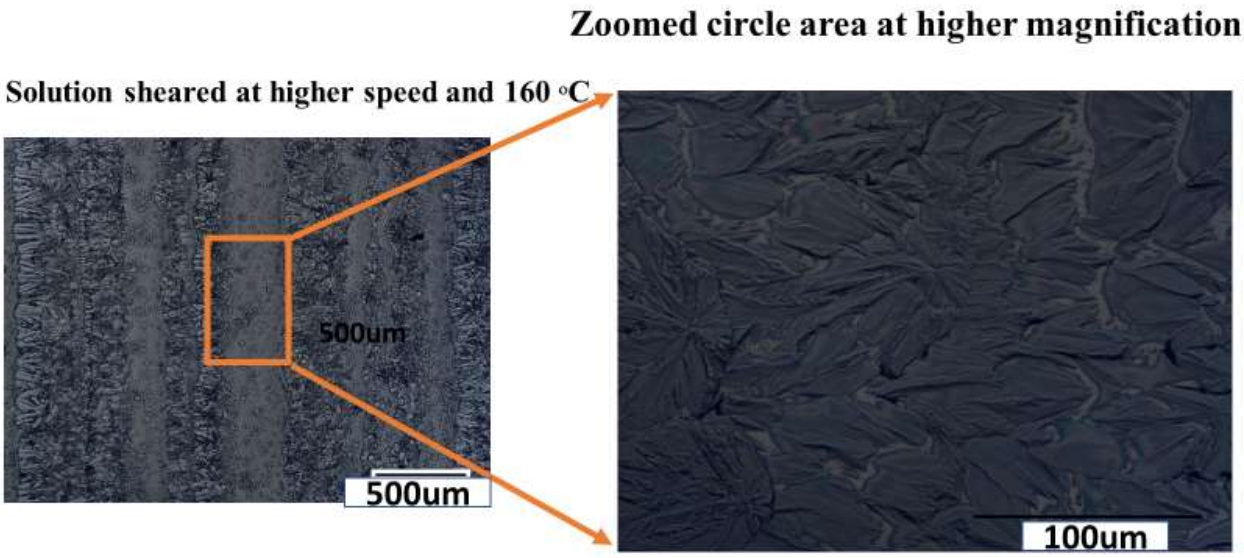

Appendix Figure A 3-8 High magnification optical microscopic image of blade-coated perovskite film at sheared at high speed of 0.275 mm/sec and the circle area is showing follower-like crystal structure in between the larger crystal grain

The perovskite crystallized film is fabricated with two different speeds of 0.125mm/sec and 0.15mm/sec under substrate heating at 150 °C degree. The crystal grains formed with larger than 500 micrometer size which is strongly depends on blade coating speeds and solvent evaporation rate.

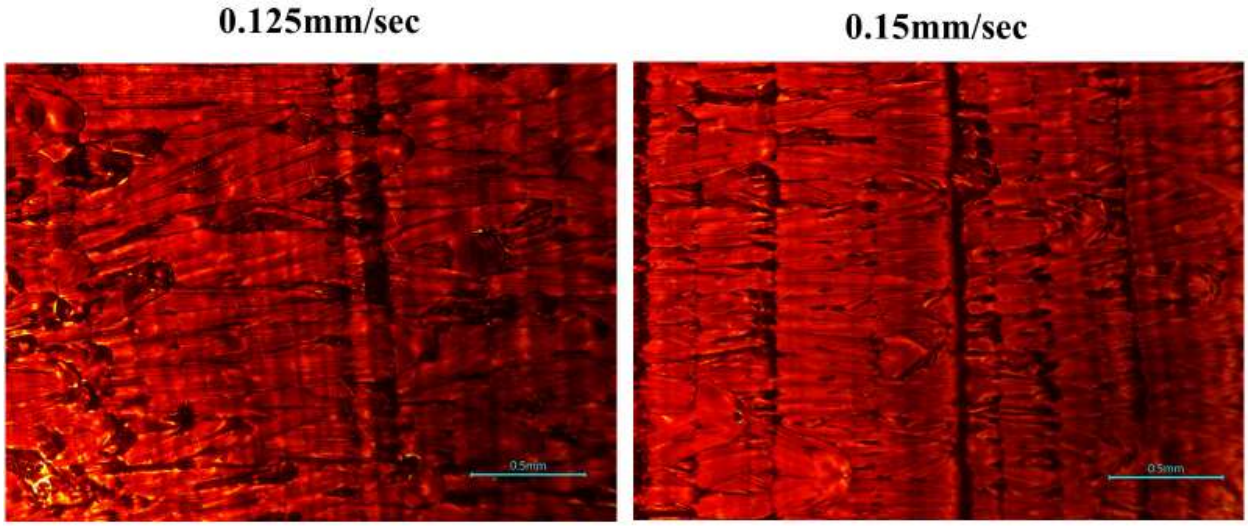

Appendix Figure A 3-9 Optical images of blade coated $CH_3NH_3PbI_3$ perovskite film at 150 ^oC using 0.125mm/sec (thick film) and 0.15mm/sec (thin film) shearing speeds.

Different solvent based perovskite solution was applied in shearing technique to controlling the crystal growth and orientation.

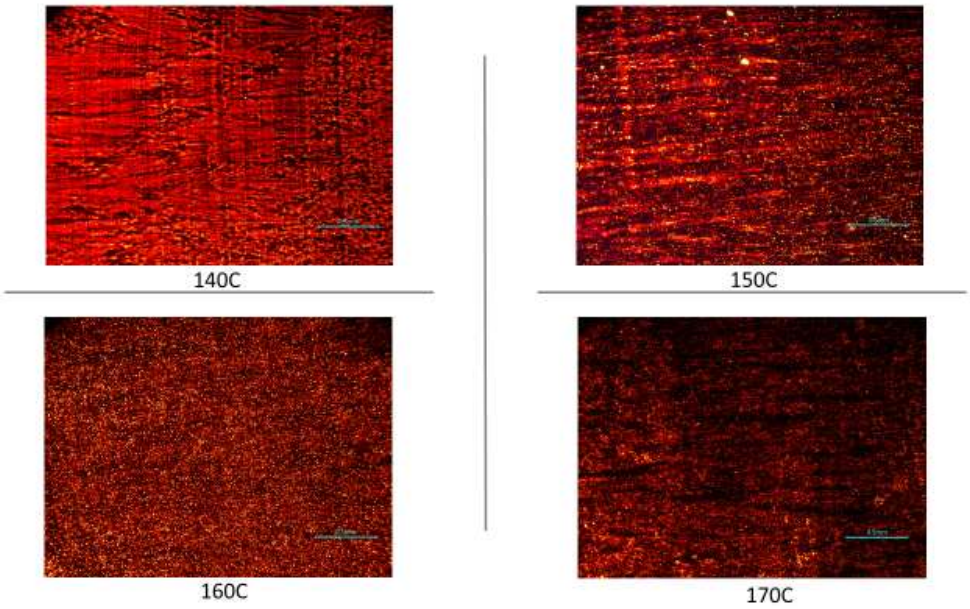

Appendix Figure A 3-10 Pure NMP based perovskite (0.3M concentration) solution sheared at different temperature and shearing speeds of 0.125mm/sec

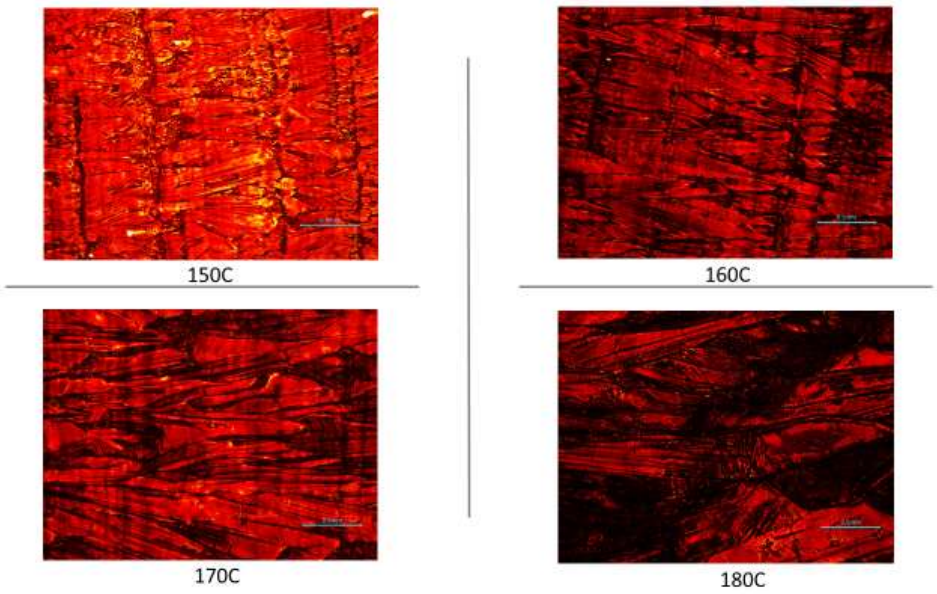

Appendix Figure A 3-11 10v% NMP in DMSO and sheared at 0.15mm/sec

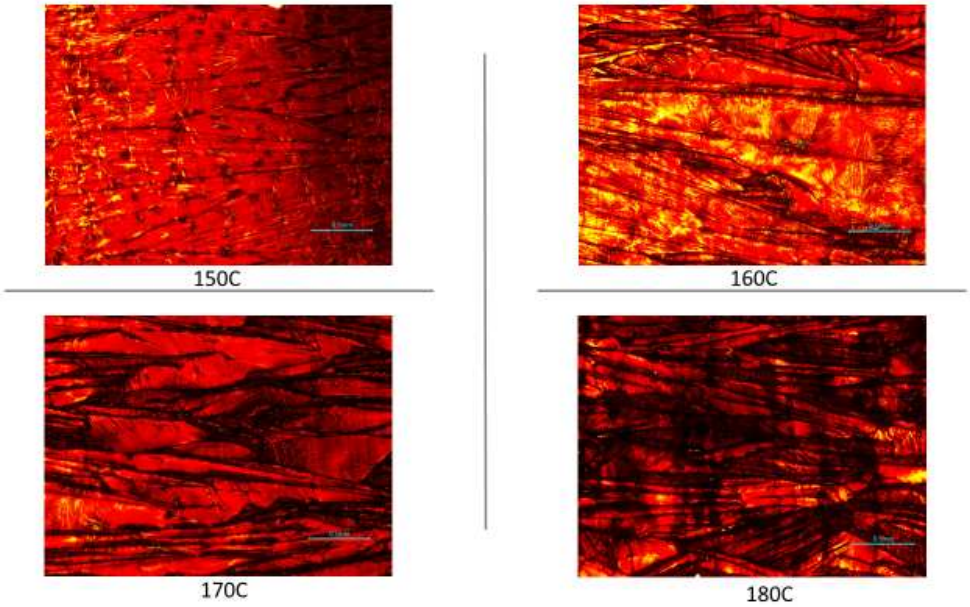

Appendix Figure A 3-12 25v% NMP in DMSO and sheared at speed 0.125mm/sec

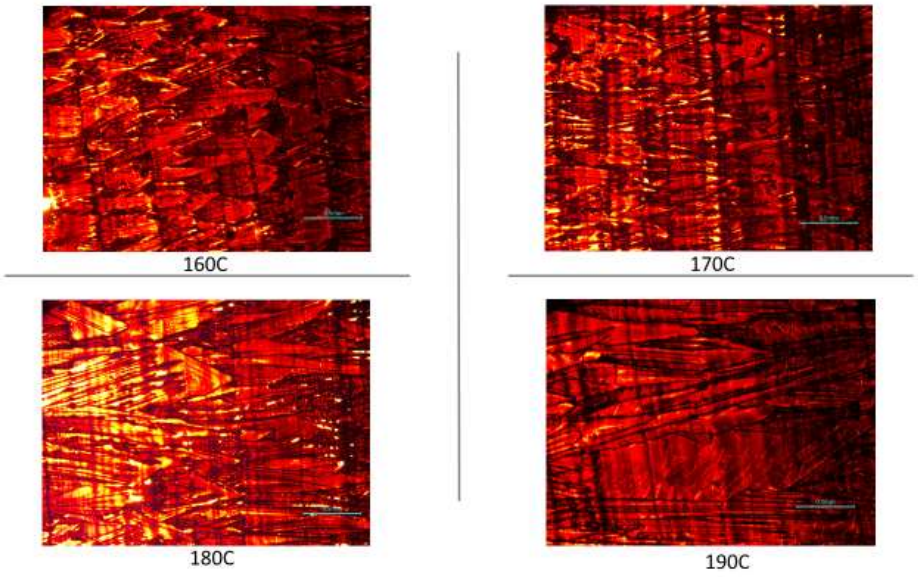

Appendix Figure A 3-13 50v% NMP in DMSO and sheared at speed 0.125mm/sec

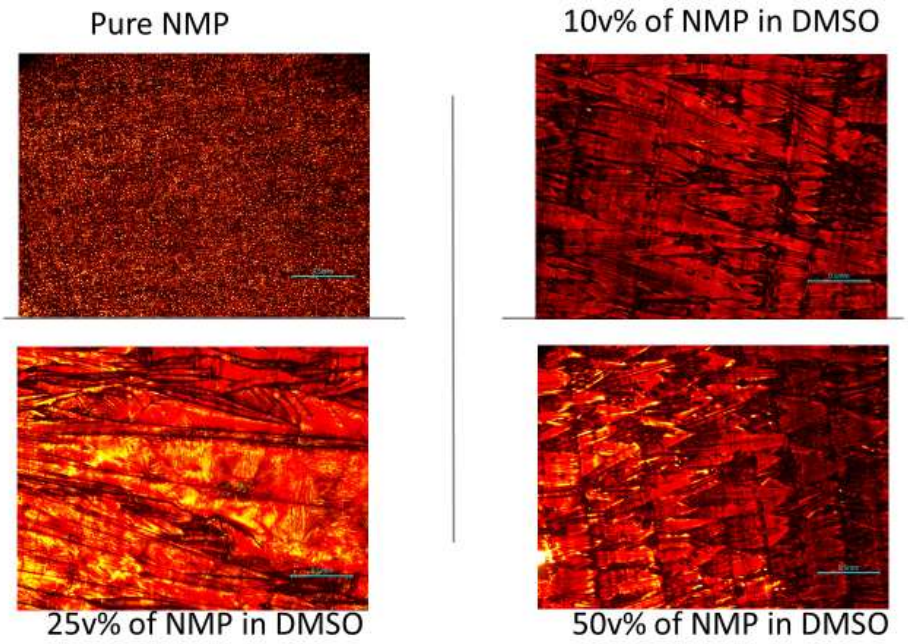

Appendix Figure A 3-14 Morphology comparison at different ratio of NMP solvent in DMSO solvent

High boiling point (204 °C) of gamma butyrolactone (GBL) solvent was mixed with precursor DMSO solvent in perovskite solution. A GBL solvent was partially mixed with DMSO solvent to prepare precursor $CH_3NH_3PbI_3$ perovskite solutions. A GBL mixing ratio was started from 10v% to 100v% in precursor DMSO solvent.

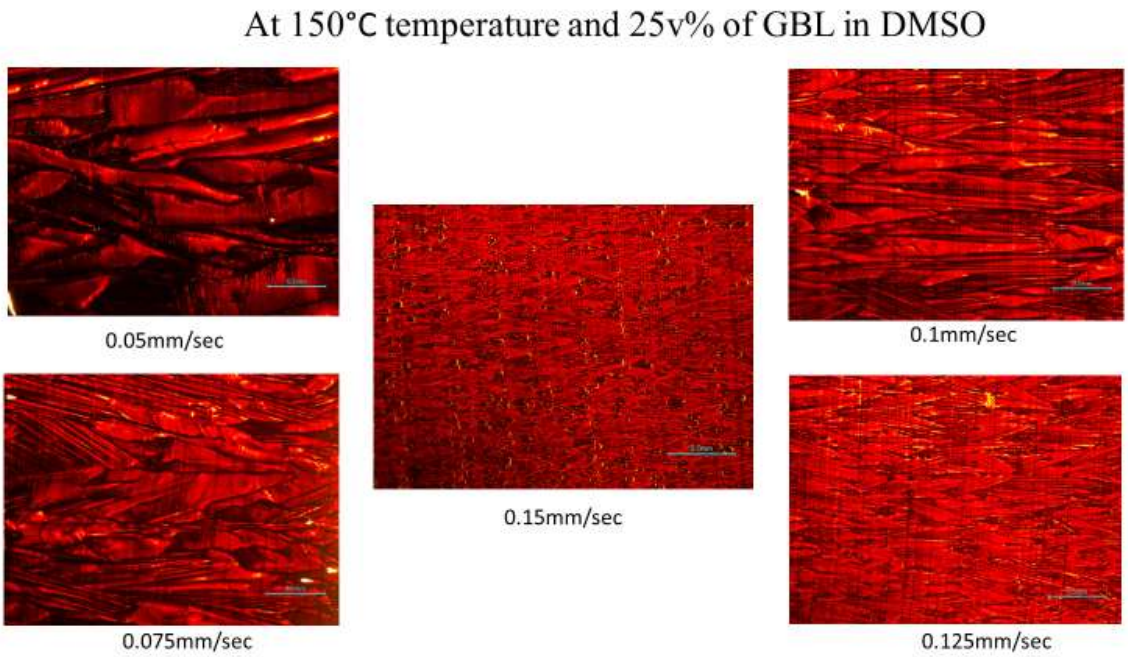

Appendix Figure A 3-15 Perovskite film morphology at 150 °C for different sheared speed

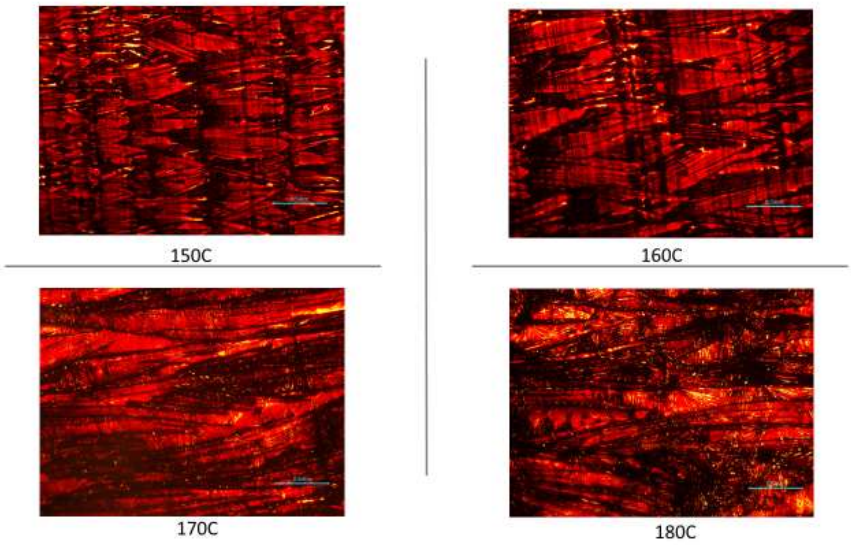

Appendix Figure A 3-16 50v% of GBL in DMSO based perovskite film morphology

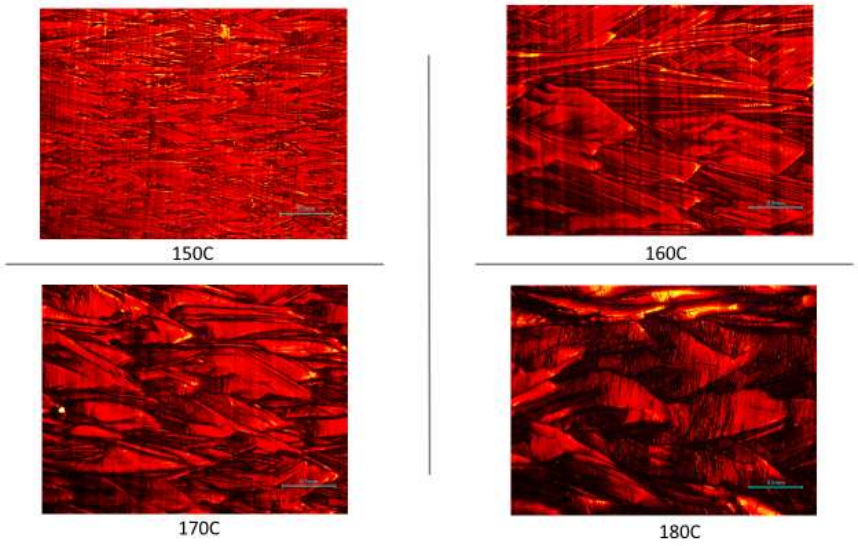

Appendix Figure A 3-17 75v% of GBL in DMSO based perovskite thin film morphology

The Dispersive X-ray Spectroscopy (EDS) analysis was applied to the plane area, and micro-size crystal grain in the perovskite film to examine the number of elements and the atomic percentage of lead and Iodine. The analyzed NMP and GBL based perovskite films were included beside of DMSO based film analysis and its confirmed the absolute ratio of lead (Pb) and Iodine (I) in the crystal domain.

It was proven that the ratio of lead and iodine in DMSO based crystallized film by EDS analysis and it gives good ratio as expected. The atomic ratio of Pb and I_2 was 36.5: 64.49 in DMSO-based perovskite grain, which was a good agreement with an earlier report [73] by neglecting the small amount of C and N.

Spectrum	In stats.	C	N	I	Pb	Total
1	Yes	16.30	9.28	54.50	19.92	100.00
2	Yes	17.03	10.43	54.25	18.30	100.00
3	Yes	20.15	12.43	49.33	18.08	100.00
4	Yes	17.10	11.86	52.33	18.71	100.00
5	Yes	19.97	11.82	48.10	20.12	100.00
6	Yes	18.59	11.67	52.75	17.00	100.00
Mean		18.19	11.25	51.88	18.69	100.00
Std. deviation		1.63	1.17	2.62	1.18	
Max.		20.15	12.43	54.50	20.12	
Min.		16.30	9.28	48.10	17.00	
All results in atomic (%)						

Appendix Table A 3-1 Atomic percentage of Lead and Iodine from EDS analysis of perovskite film

Appendix 2

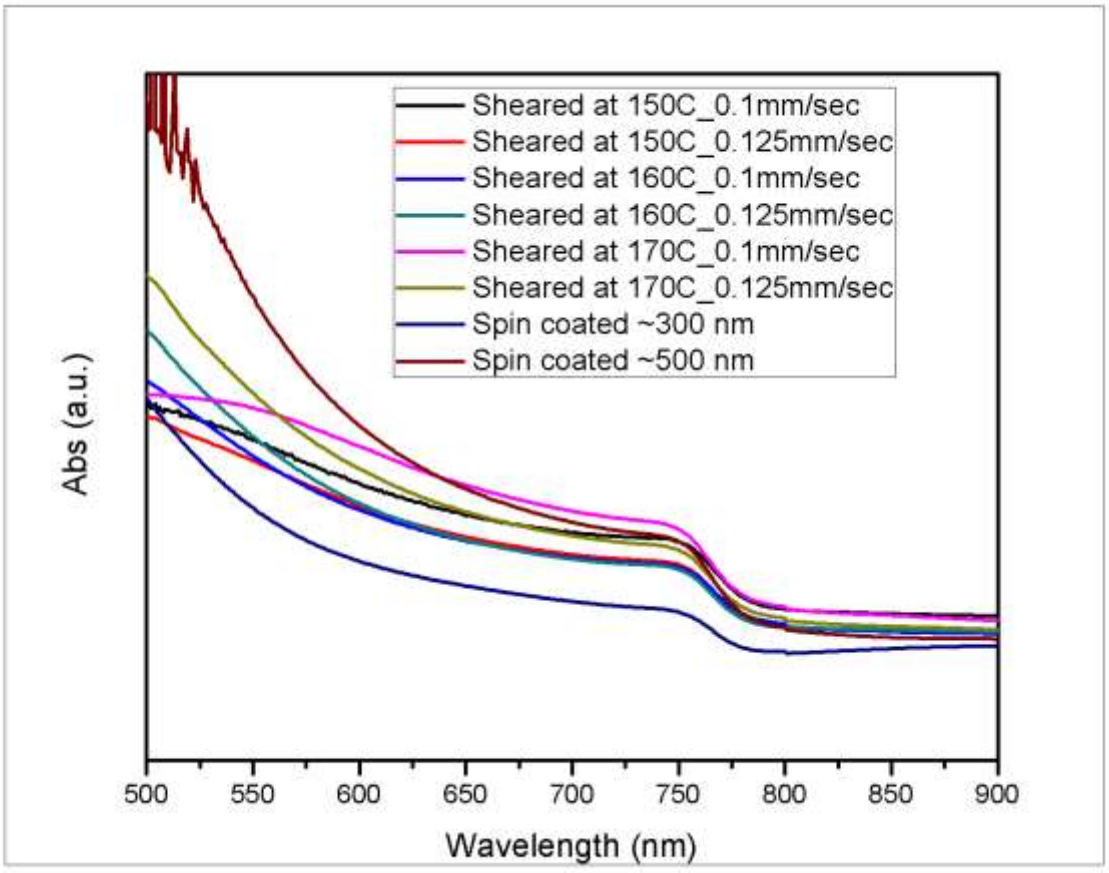

Appendix Figure A 4-1 Light absorption of spin-coated and solution sheared perovskite film

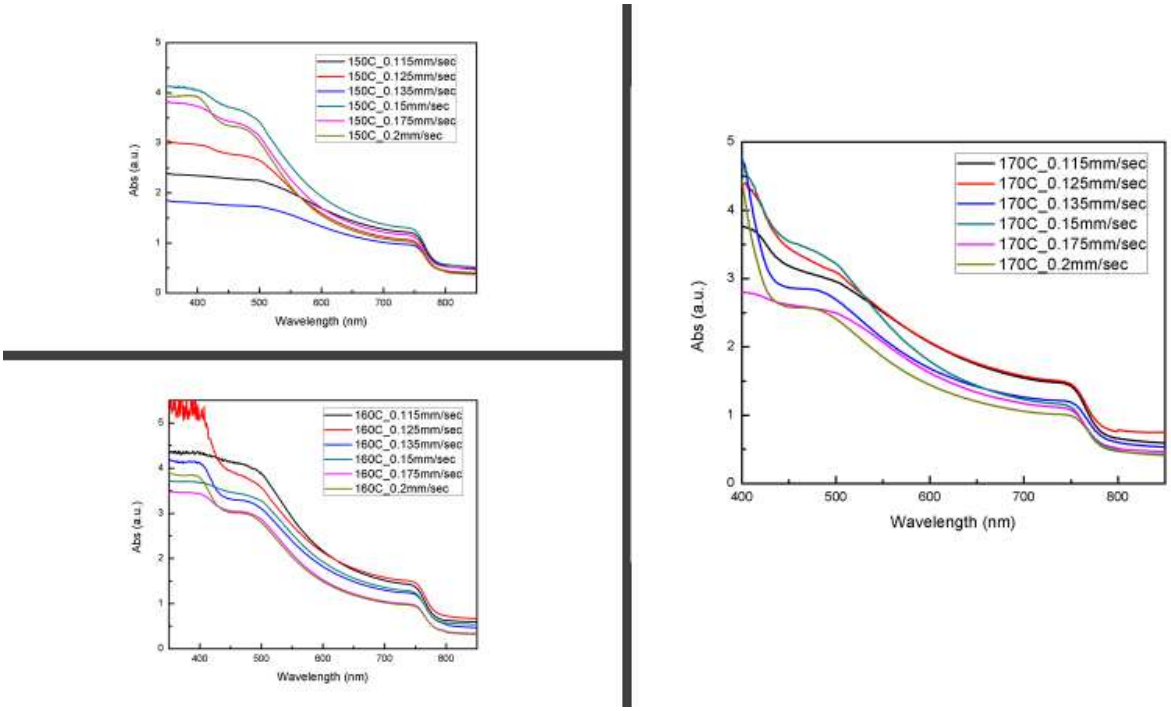

Appendix Figure A 4-2 Absorbance of perovskite film at different temperature and shearing speeds

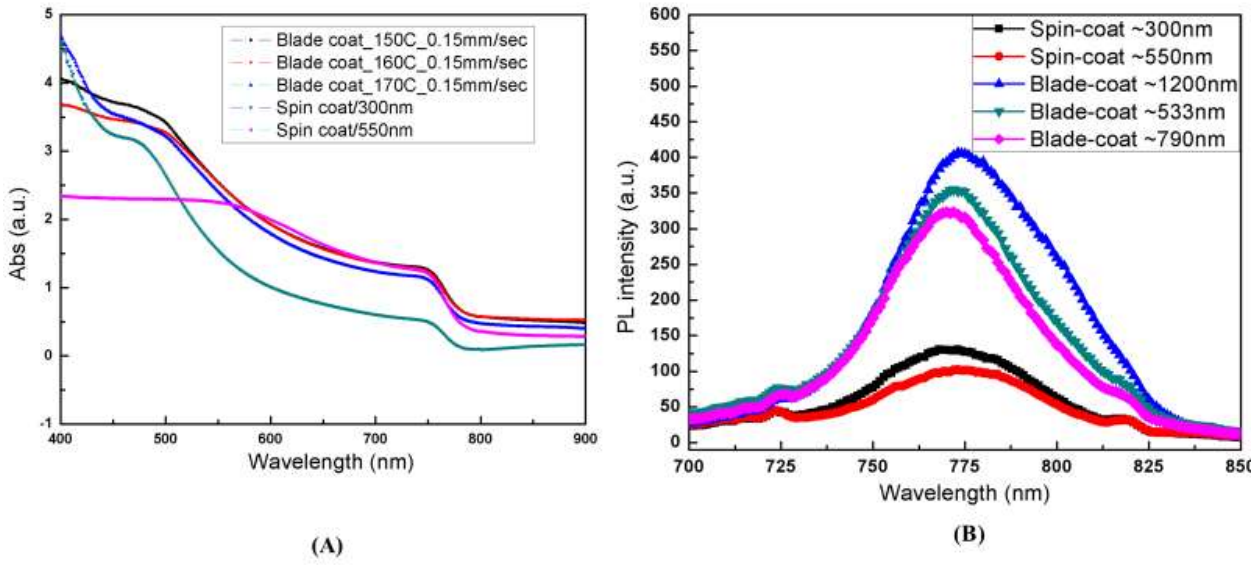

Appendix Figure A 4-3 The absorbance of the blade-coated perovskite film using at different substrate temperature and spin-coated perovskite film (A), and photoluminescence intensities based on perovskite film thickness

Appendix 3

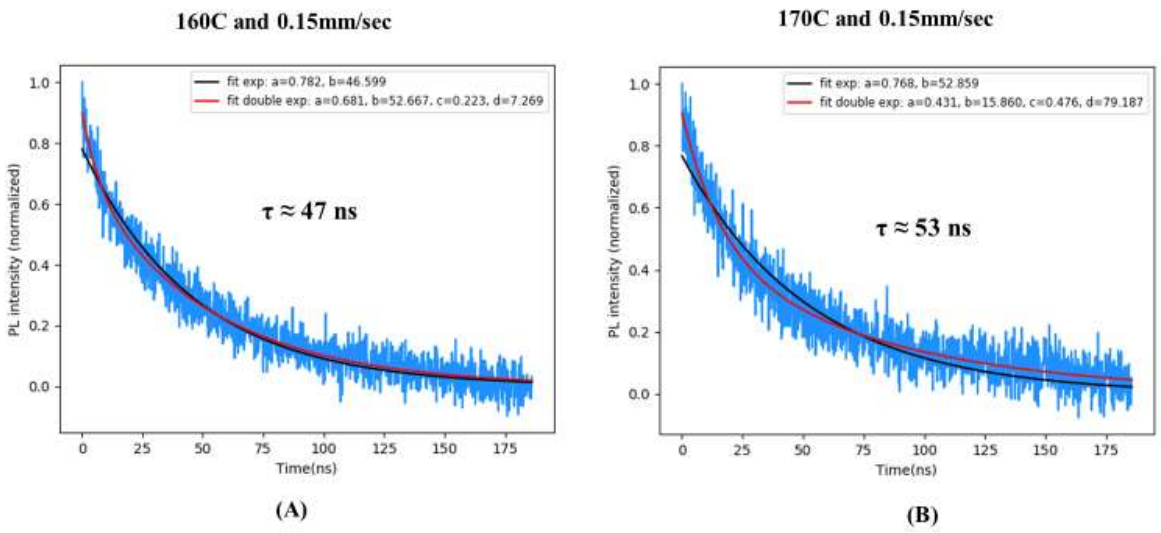

Appendix Figure A 5-1 Time-resolved PL decay of blade-coated perovskite film at 160 °C and 170 °C temperature and the highest carrier lifetime 53ns is achieved from perovskite film by 170 °C

The gold electrode channel was deposited in parallel and perpendicular of crystal direction. A interlayer of Spiro-MeOTAD was sheared in between gold electrode and perovskite layer to make better ohmic contact and decrease the contact resistance.

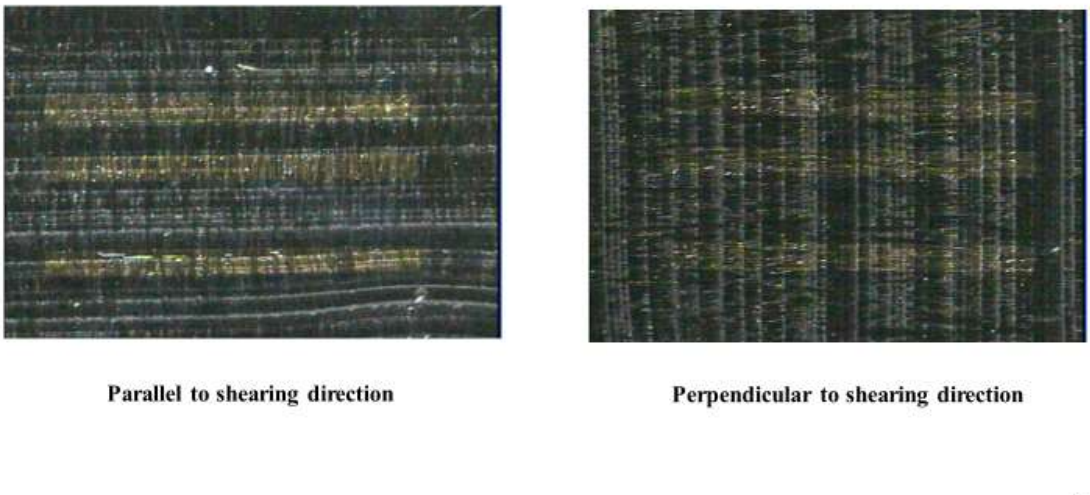

Appendix Figure A 5-2 A Photograph of channel (0.75mm) direction on perovskite film

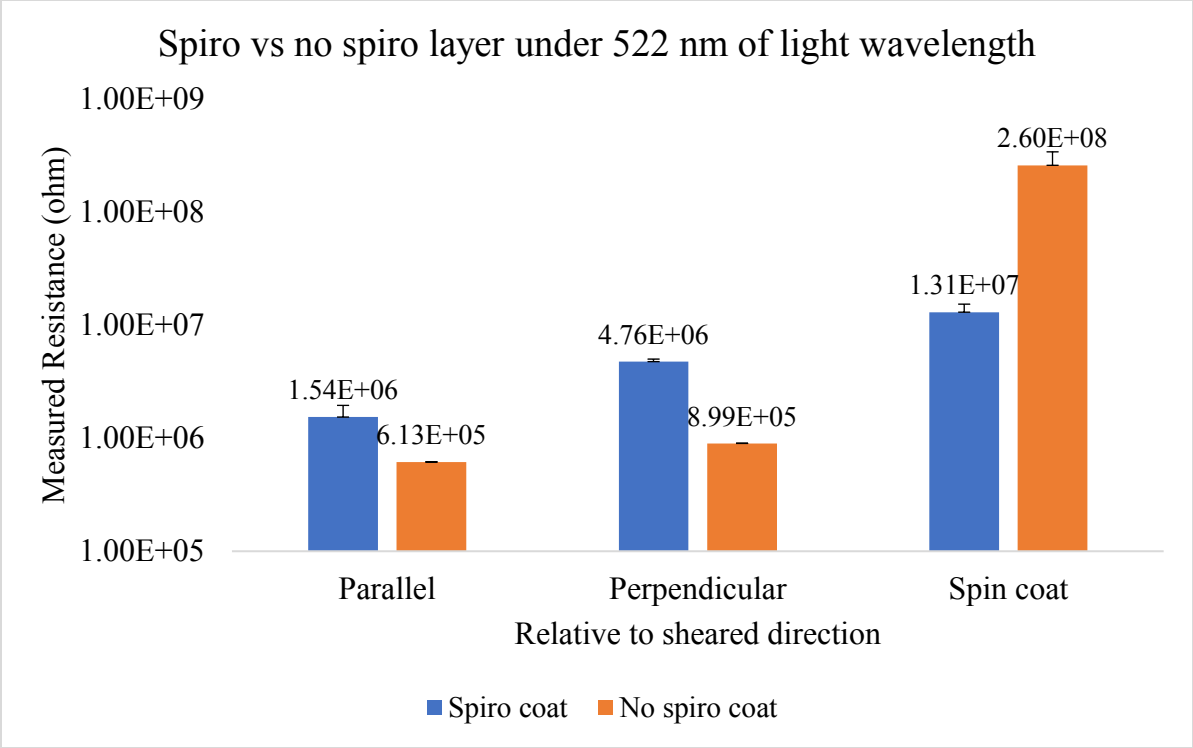

Appendix Figure A 5-3 The photo-resistance performance of blade-coated and spin coated perovskite film under light wavelength of 522nm

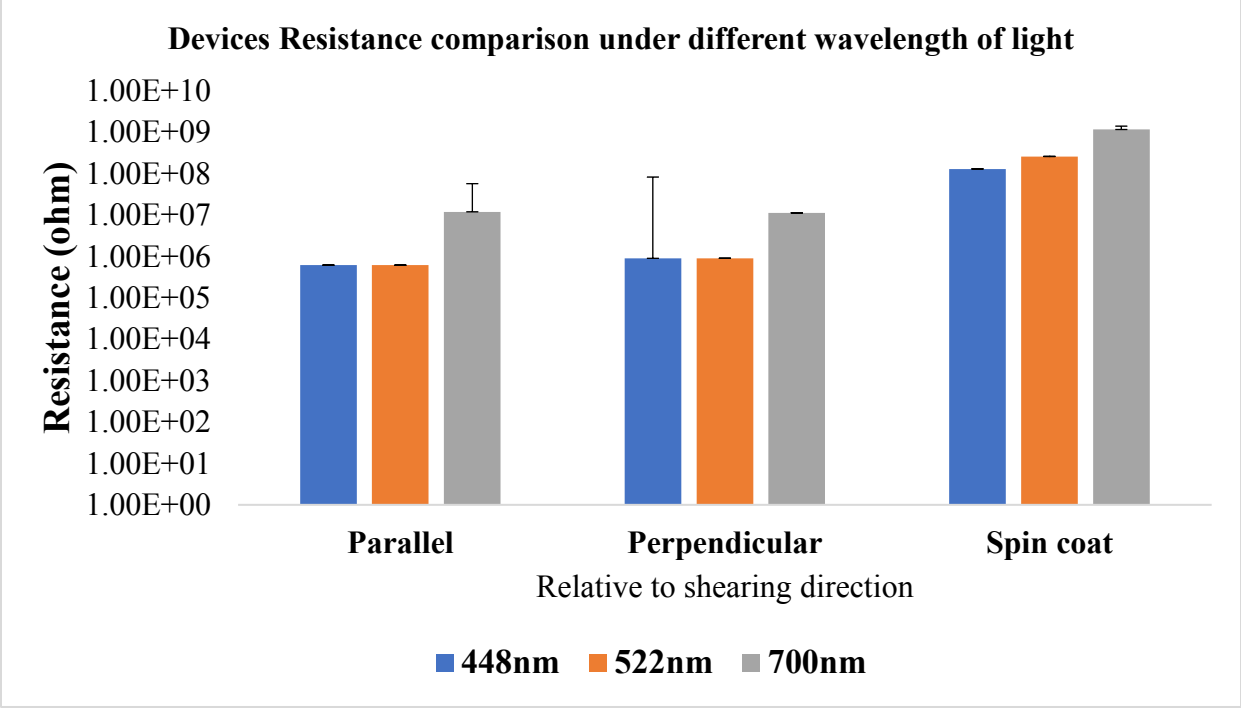

Appendix Figure A 5-4 Devices resistance (ohm) measured under different wavelength of light

Optical power density (uW/cm^2)	Responsivity (A/W) of Spin-coated (~550nm) device	Responsivity (A/W) of Blade-coated thin device (~533nm) device
0.020	7.125475	54.30146
0.050	38.39127	140.9918
0.100	40.26649	148.6925
0.200	38.6352	157.3202
0.500	35.39268	154.26
1	33.14791	159.2887
2	31.11796	164.901
5	28.58818	166.7727
10	26.26261	157.7061
20	23.1957	141.9675
50	19.78987	122.921
100	17.89779	98.14214
200	16.69802	75.23406
500	15.72964	50.16834
1000	15.2908	34.91726

Appendix Table A 5-1 Responsivity difference between thin and thick blade-coated photodetectors at different power density using a green light wavelength of 522nm and under 4v biasing

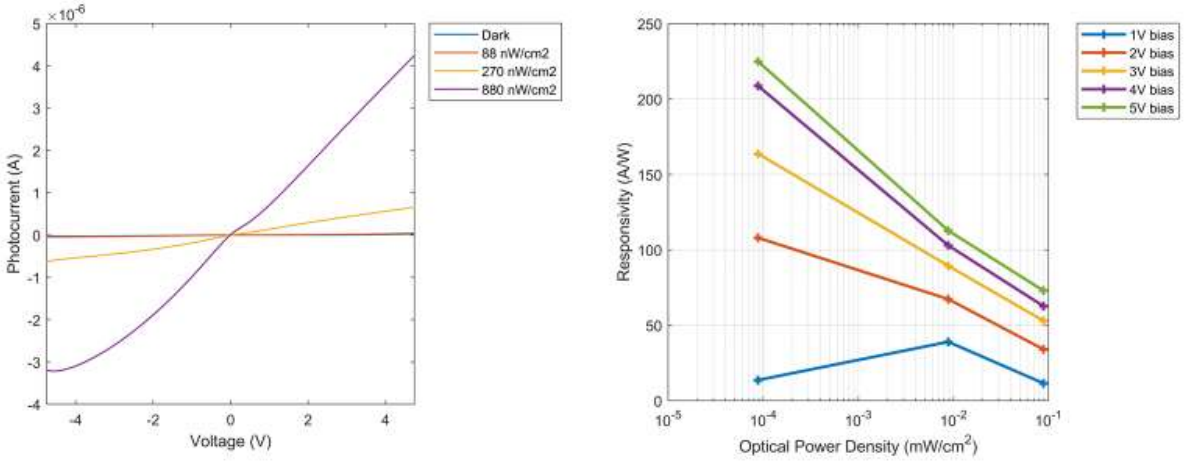

Appendix Figure A 5-5 Responsivity of a blade coated thicker (~790nm) device and illuminated with a 700nm wavelength

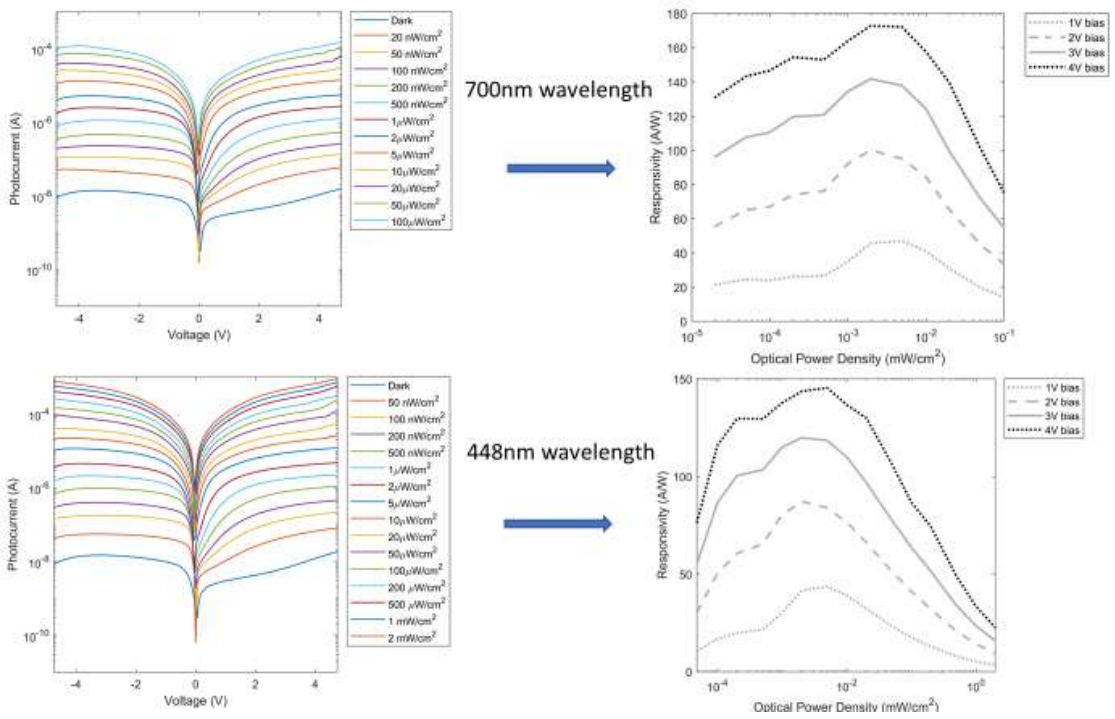

Appendix Figure A 5-6 Responsivity of a blade coated thicker device and illuminated with a 700nm and 448nm of wavelength